Energetics and Electronic Properties of Edges of Two-dimensional Materials

Ayaka Yamanaka

February 2017

Energetics and Electronic Properties of Edges of Two-dimensional Materials

Ayaka Yamanaka

Doctoral Program in
Nano-Science and Nano-Technology

Submitted to the Graduate School of
Pure and Applied Sciences
in Partial Fulfillment of the Requirements
for the Degree of Doctor of Philosophy in
Science

at the
University of Tsukuba

Abstract

Two-dimensional materials have great deal of attention not only in nanoscience but also in nanothechnology because of its unique geometric and electronic properties. The electronic properties of these materials are strongly affected by their edges. However, it is still unclear the correlation between edge geometry and electronic structure. In this thesis, we study the energetics and electronic properties of edges of two-dimensional materials using density functional theory.

First, we study the energetics and electronic properties of graphene edges. Our calculations showed that the stability of graphene edges strongly depends on the length of the zigzag edge portion. Near-zigzag edges are less stable than near-armchair edges because of the large number of states at the Fermi level (E_F) arising from edge states. Thus, the edge stability strongly correlates with the electronic structures near the E_F of graphene nanoribbons.

Under a lateral electric field, we showed the anomalous screening effect against the external electric field; the electrostatic potential oscillates rapidly at the atomic site in zigzag shape, leading to over-screening in the vicinity of edge C atomic sites. The penetration depth of anomalous screening depends on the edge structure of nanoribbons. We also showed that the nearly free electron (NFE) state emerges in the vacuum region outside the leftmost edge of the ribbons and shifts downward with increasing the lateral electric field. Electrons are injected into the NFE state of graphene nanoribbons by the critical electric field. NFE states strongly depend on the mutual arrangements of graphene nanoribbons with respect to the electric field, while the π electron states are insensitive. We clarified that the electric field concentration around the edges leads to the orientation dependence of the NFE states on the field.

Next, we study the energetics and electronic properties of hexagonal boron nitride (h-BN) nanoribbons. Our calculations showed that the stability of h-BN edges strongly depends on the edge termination. In the case of hydrogenated edges, the formation energy is constant for all edge shapes ranging from armchair to zigzag, indicating that h-BN may exhibit rich variation in their edge atomic arrangements under static conditions. The hydrogenated h-BN nanoribbons are insulators with an energy gap of 4 eV irrespective of edge shape. In contrast, the formation energy of h-BN nanoribbons with clean edges monotonically increases as the edge shape is changed from armchair to zigzag because of the increase of density of states at the E_F arising from dangling bond states. We also study the polar properties of h-BN nano-flakes by evaluating their electrostatic potential. The polarity of the nanoribbons is sensitive to their edge shape, edge hydrogen coverage, and uniaxial tensile strain. By controlling the hydrogen concentration at edges and the uniaxial tensile strain, we can invert the polarity of h-BN, indicating that h-BN nanoribbons can exhibit non-polar properties at a particular condition, even though the nanoribbons essentially have polarity at the edge. We also found that the edge angle affects the polarity of nanoribbons with hydrogenated edges.

Acknowledgments

I would like to express the deepest appreciation to Professor Susumu Okada for his continuing guidance, discussions, and encouragements. I also would like to appreciate Professor Atsushi Oshiyama, Dr. Takazumi Kawai, Professor Yasuhiro Tokura, and Professor Akinobu Kanda for fruitful discussions. I am grateful to Mina Maruyama for many discussions and advices. I would like to thank all the members of laboratory. Part of this work was supported by the Grant-in-Aid for JSPS Research Fellow. Finally, I would like to sincerely thank my parents for their continuing supports and encouragements.

Contents

Chapter 1 Introduction 1

References 8

Chapter 2 Calculation Methods 13

2.1 Density Functional Theory 13

2.2 Kohn–Sham Equation 14

2.3 Local Density Approximation 15

2.4 Generalized Gradient Approximation 16

2.5 Pseudopotential 16

2.6 Effective Screening Medium Method 18

References 20

Chapter 3 Geometric and Electronic Properties of Graphene Edges 23

3.1 Introduction 23

3.2 Energetics and Electronic structure 25

3.2.1 Hydrogenated Edges 26

3.2.2 Clean Edges 31

3.3 Electrostatic Potential under an Electric Field 35

3.4 Electron Injection into Nearly Free Electron States 39

3.5 Influence of Local Electric Field on Nearly Free Electron States . 46

3.6 Conclusion 52

References 54

Chapter 4 Geometric and Electronic Properties of h-BN 57

4.1 Introduction 57

4.2 Energetics and Electronic Structure 58

4.2.1 Hydrogenated edges 59

4.2.2 Clean edges 65

4.3 Polarity of Edges 68

4.4 Conclusion 73

References 76

Chapter 5 Summary 79

List of Publications 81

Chapter 1

Introduction

Layered materials, such as graphite [1.1–1.3], hexagonal boron nitride (h-BN) [1.4], transition metal dichalcogenides (TMDCs) [1.5, 1.6], and black phosphorus [1.7–1.9] are starting materials of two-dimensional atomic layer materials. Because each layer is weakly bound *via* van der Waals interaction, it is expected to exfoliate the atomic layer from these layered materials. Indeed, several two-dimensional materials have been successfully synthesized, ever since the mechanical exfoliation of graphene from graphite in 2004 [1.1]. These materials have great deal of attention not only in nanoscience but also in nanothechnology because of its unique geometric and electronic properties.

Graphene [Fig. 1.1(a)] has a honeycomb network structure of sp^2 C atoms that form an ultimate thin film with single-atom thickness. This honeycomb network of sp^2 C atoms means that graphene behaves as a metal with a vanishing density of states at the Fermi level (E_F) because of the presence of two linear dispersion bands at the E_F (Fig. 1.2). An angular-resolved photoelectron spectroscopy experiment on graphene indeed demonstrated the emergence of a pair of linear dispersion bands at the E_F [1.10]. These linear dispersion bands lead to massless electrons near the E_F, which endow graphene with a rich variety of interesting physical properties. For example, the mobility limit of a graphene sheet is expected to exceed the highest known mobility of inorganic semiconductors and semiconducting carbon nanotubes (CNTs) [1.11]. Furthermore, this also leads to the unusual quantum Hall effect [1.12–1.15].

On the other hand, the electronic structure of graphene is known to be fragile with respect to foreign materials such as insulating substrates [1.16–1.18], metal electrodes [1.19, 1.20], other graphene/graphite layers [1.21–1.24], and an external electric field [1.25–1.30]. Among the various foreign elements that can form hybrid structures with graphene, electric fields are one of the important factors for determining their electronic properties in device structures. Because an electric field is essential for operating and functionalizing electronic devices, it is necessary to understand the fundamental behavior of graphene under the electric fields.

h-BN [Fig. 1.1(b)] is insulating version of graphene which consists of boron and nitrogen atoms. Chemical difference between B and N atoms make h-BN an insulator with a large energy gap of 5 eV between the top of the valence band and the bottom of conduction band localized on N and B atoms, respectively (Fig. 1.3). Insulating property and atomically flat networks of h-BN make them a supporting substrate for graphene without substantial modification of their fundamental properties, leading to the remarkable carrier mobility [1.31–1.34]. h-BN itself have also attracted much attention because of their structural similarities and electronic differences to those of graphene [1.35–1.38].

TMDCs, such as MoS_2 [Fig. 1.1(c)], WSe_2, *etc.*, also possess the honeycomb network structure as the case of graphene. In contrast, one transition metal atom is combined with six chalcogen atoms situated above and below the transition metal layer. Thus, TMDCs does not have single-atom thickness in contrast to graphene and h-BN. Electronic structure of TMDCs strongly depend on the number of layers. Monolayer and multilayer TMDCs are the direct and indirect gap semiconductor, respectively (Fig. 1.4). Absence of the inversion symmetry and substantial spin-orbit interaction leads to the new valley degree of freedom, which makes possible selective photoexcitation of carriers by using circularly polarized light [1.39].

Phosphorene [Fig. 1.1(d)] is the monolayer of black phosphorus, which is the most stable allotrope of phosphorus at room temperature. Its structure is corrugated honeycomb network of phosphorus atoms, which also posses the internal structure perpendicular to the layer as in the case of TMDCs. Phosphorene is the direct gap semiconductor with energy gap of about 1 eV. Energy gap monotonically decrease with increasing the number of layers, and finally saturate the energy gap of bulk black phosphorus (0.3 eV).

Because of the two dimensionality, electronic properties of these materials are strongly affected by their edges. It is well known that the electronic structure of graphene depends on their edge structures. In the case of graphene nanoribbons with armchair edges [Fig. 1.6(a)], energy gap possesses the triple periodicity with ribbon width (Fig. 1.7) [1.40]. Energy gap asymptotically decreases with increasing their width. In contrast, graphene nanoribbons with zigzag edges [Fig. 1.6(b)] are a metal possessing peculiar electronic structure at the E_F [1.41–1.43]. Graphene nanoribbons with zigzag edges have a pair of flat bands at the E_F and in the zone boundary of one-dimensional Brillouin zone (Fig. 1.8). These flat band states exhibit an unusual feature depending on the wave number k: The states are perfectly localized at the edge atomic site at $k = \pi$ (Fig. 1.9). They are gradually penetrated with decreasing

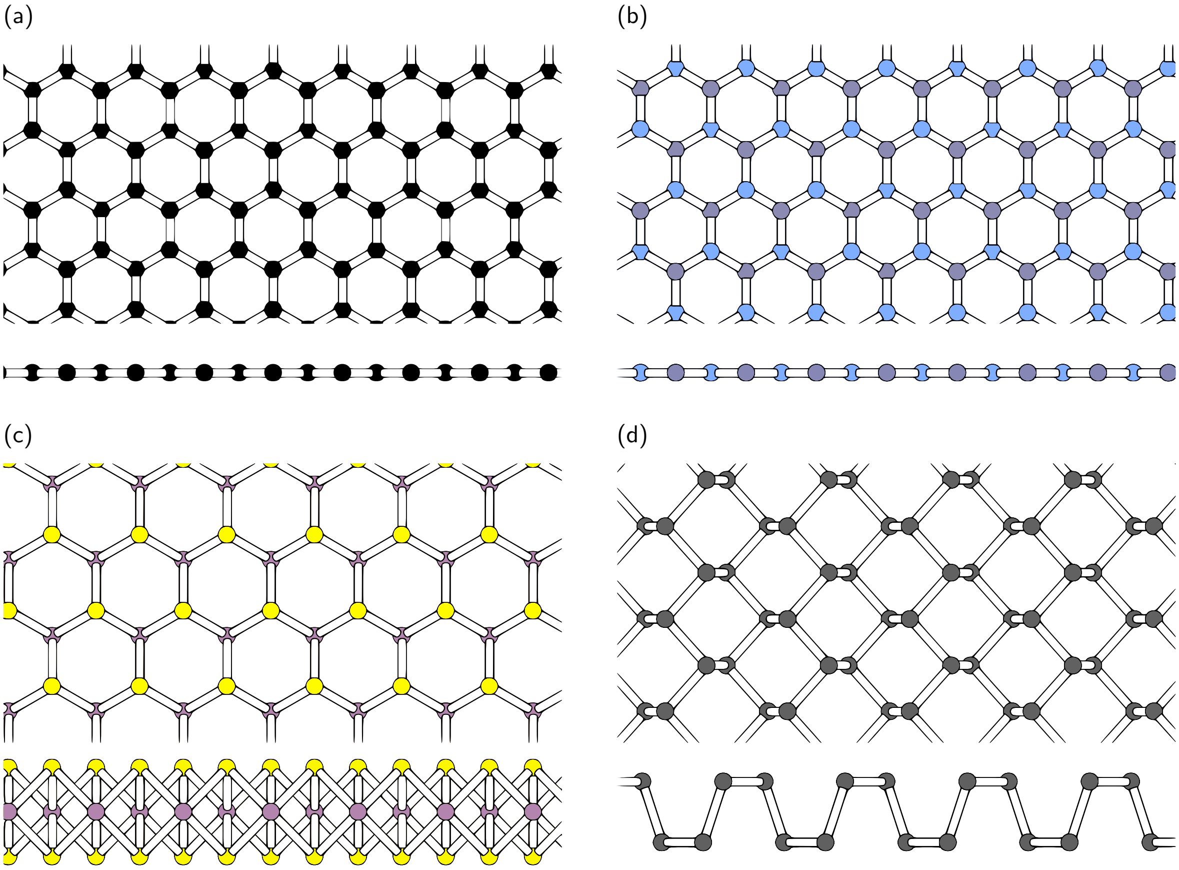

Figure1.1 Geometric structure of (a) graphene, (b) h-BN, (c) TMDC (MoS_2), and (d) phosphorene monolayer. Upper and lower panels are top and side views of layers, respectively. Black, violet, pale blue, magenta, yellow, and gray circles denote carbon, boron, nitrogen, molybdenum, sulfur, and phosphorus atoms, respectively.

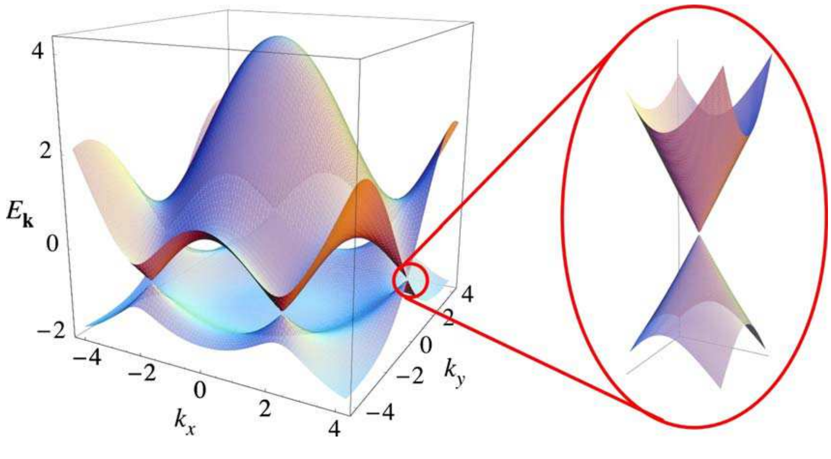

Figure1.2 Electronic structure of graphene [1.3].

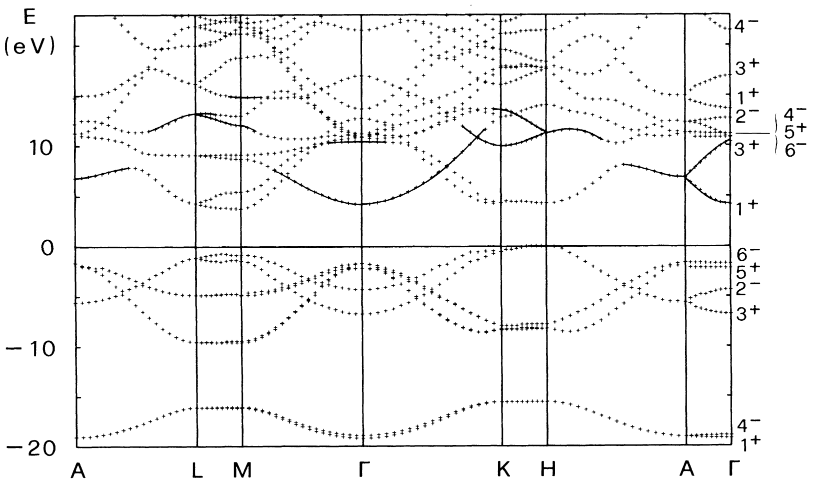

Figure1.3 Electronic structure of h-BN [1.49].

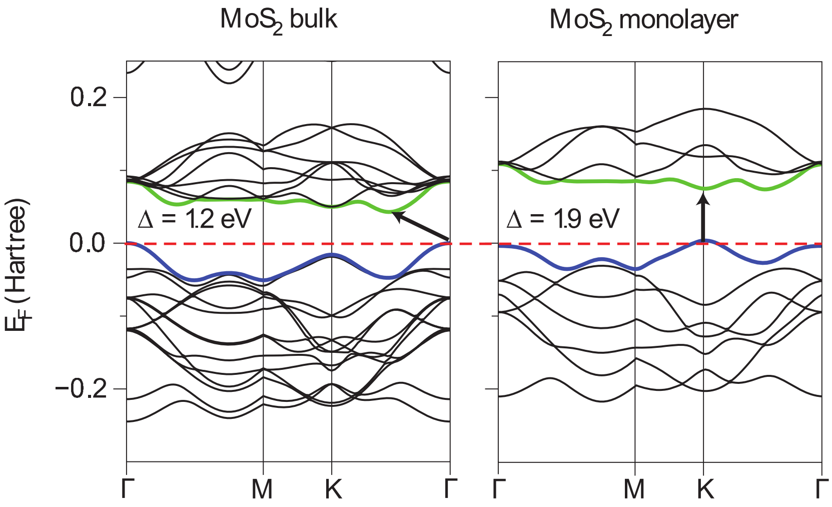

Figure1.4 Electronic structure of bulk and monolayer MoS_2 [1.6].

the wave number k, and finally are extended throughout the sheet as the bulk π state nature of graphene at K point of two-dimensional Brillouin zone. According to the distribution, the states known to be the edge states, which are common in the other two-dimensional materials with hexagonal network. The flat bands at the E_F are known to be split into upper and lower branches under the infinitesimal on-site U, leading to the spin polarization around the edge atomic sites. Thus, the graphene can be applicable for spin related nanodevices by controlling their sizes and shapes. Additionally, the edge roughness induces further variations in their electronic structures [1.44, 1.45]. However, it is still unclear the correlation between edge atomic and electronic structures.

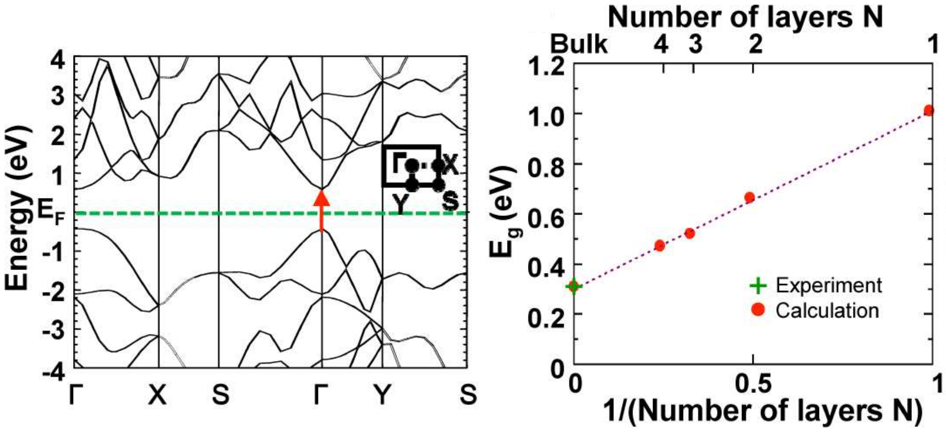

Figure1.5 Electronic structure and the energy gap as a function of the number of layers of phosphorene [1.8].

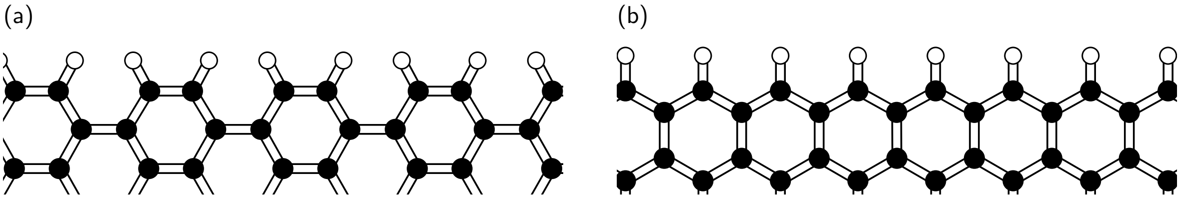

Figure1.6 Representative edge structure of graphene. (a) Armchair and (b) zigzag edges.

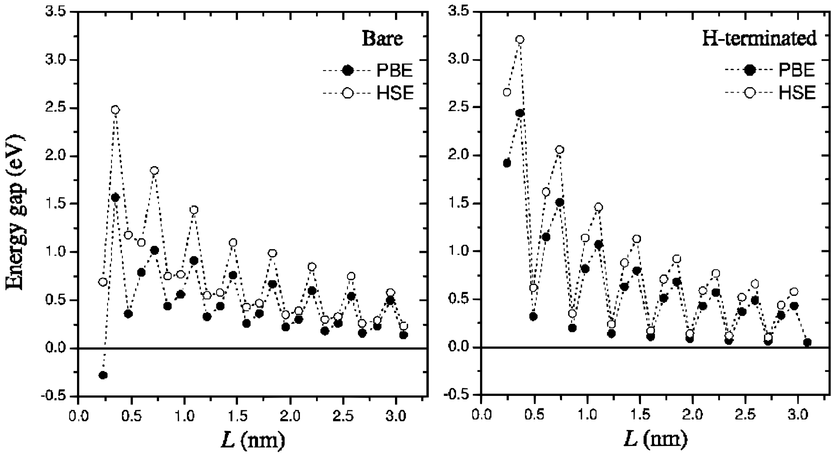

Figure1.7 Energy gap of graphene nanoribbons with armchair edges as a function of the ribbon width [1.40].

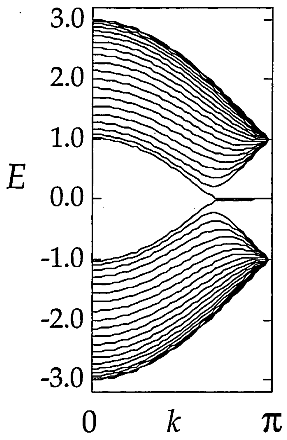

Figure1.8 Electronic structure of graphene nanoribbons with zigzag edges [1.41].

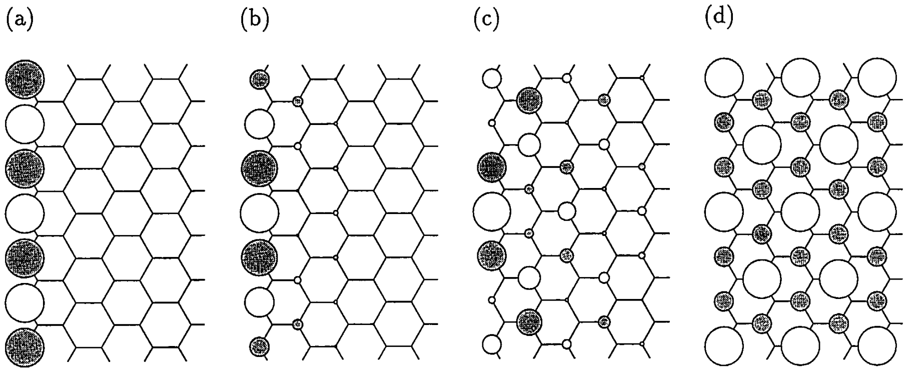

Figure1.9 Wave function distribution of graphene nanoribbons with zigzag edges at (a) $k = \pi$, (b) $8\pi/9$, (c) $7\pi/9$, and (d) $2\pi/3$ [1.41].

Layered materials mentioned above inherently possess large spacings between their dense and flat atomic networks. Because of the large spacing between covalent atomic networks, these layered materials possess unusual electronic states in their unoccupied state below the vacuum level, which plays a decisive role in their excited state spectrum, and even in ground state electronic properties upon the intercalation of foreign atoms or molecules into the spacing [1.46–1.51]. The states have their amplitude in the vacuum region between the atomic layers with a free electron nature along the lateral directions. Thus, the states are known as nearly free electron (NFE) states or interlayer states in these materials. Furthermore, the state shifts downward upon electron injection, leading to unusual transport properties because of the attractive potential resulting from guest intercalant materials [1.46]. In addition to layered materials, similar free electron states are also found in the interunit spacing of nanoscale materials [1.52–1.55] and on the surfaces of conventional metals [1.56–1.58] and semiconductors [1.59] because of the quantum spill of electrons outside the atomic networks of these materials, which acts as the attracting potential for the unoccupied state in the vacuum region.

It has been reported that NFE states are tunable by applying an external electric field normal to the atomic layers of these layered materials [1.51,1.60–1.62]. The NFE states of few-layered graphite shift downward under an external electric field, and cross the E_F at a certain critical electric field that strongly depends on the thickness of the graphite thin films. Similar downward shifts have been also observed in h-BN thin films [1.62] and TMDC thin films [1.51], whose electric field dependence is similar to that of graphite thin films. In these cases, electrons are injected into NFE states under the critical electric field, which depends on both the thickness of the thin films and the constituent atom species of these materials. These downward shifts of the NFE states by the perpendicular electric field are ascribed to the potential gradient outside the films by the electric field that effectively leads to an attractive potential for the NFE states. In addition to two-dimensional conventional surfaces, NFE states also emerge outside the edges of graphene nanoribbons, which can be regarded as the one-dimensional version of surfaces [1.63]. Furthermore, the NFE states shift downward with the injection of electrons and under the lateral electric field.

In this thesis, we aim to theoretically investigate the energetics and electronic properties of edges of two-dimensional materials. In particular, we investigate the edge stability and the electronic structure of graphene and h-BN nanoribbons with various edge structure ranging form armchair to zigzag. Then, we also aim to investigate the electronic properties of graphene nanoribbons with various edge angles under a parallel electric field to give theoretical insight into the fundamental issues for utilizing graphene in electronic devices.

References

[1] K.S. Novoselov, A.K. Geim, S.V. Morozov, D. Jiang, Y. Zhang, S.V. Dubonos, I.V. Grigorieva, and A.A. Firsov, *Science* **306**, 666 (2004).

[2] M.S. Dresselhaus and G. Dresselhaus, *Adv. Phys.* **30** 139 (1981).

[3] A.H. Castro Neto, F. Guinea, N.M.R. Peres, K.S. Novoselov, and A.K. Geim, *Rev. Mod. Phys.* **81**, 109 (2009).

[4] D. Golberg, Y. Bando, Y. Huang, T. Terao, M. Mitome, C. Tang, and C. Zhi, *ACS NANO* **6**, 2979 (2010).

[5] M. Chhowalla, H.S. Shin, G. Eda, L.-J. Li, K.P. Loh, and H. Zhang, *Nat. Chem.* **5**, 263 (2013).

[6] Q.H. Wang, K. Kalantar-Zadeh, A. Kis, J.N. Coleman, and M.S. Strano, *Nat. Nanotechnol.* **7**, 699 (2012).

[7] L. Li, Y. Yu, G. J. Ye, Q. Ge, X. Ou, H. Wu, D. Feng, X.H. Chen, and Y. Zhang, *Nat. Nanotechnol.* **9**, 372 (2014).

[8] H. Liu, A.T. Neal, Z. Zhu, Z. Luo, X. Xu, D. Tománek, and P.D. Ye, *ACS Nano* **8**, 4033 (2014).

[9] F. Xia, H. Wang, and Y. Jia, *Nature Communications* **5**, 4458 (2014).

[10] Th. Seyller, K.V. Emtsev, K. Gao, F. Speck, L. Ley, A. Tadich, L. Broekman, J.D. Riley, R.C.G. Leckey, O. Rader, A. Varykhalov, and A.M. Shikin, *Surf. Sci.* **600**, 3906 (2006).

[11] J.-H. Chen, C. Jang, S. Xiao, M. Ishigamim and M. S. Fuhrer, *Nat. Nanotechnol.* **3**, 206 (2008).

[12] K.S. Novoselov, A.K. Geim, S.V. Morozov, D. Jiang, M.I. Katsnelson, I.V. Grigorieva, S.V. Dubonos, and A.A. Firsov, *Nature* **438**, 197 (2005).

[13] Y. Zhang, Y.-W. Tan, H.L. Stormer, and P. Kim, *Nature* **438**, 201 (2005).

[14] X. Du, I. Skachko, F. Duerr, A. Luican, and E. Y. Andrei, *Nature* **462**, 192 (2009).

[15] K.I. Bolotin, F. Ghahari, M.D. Shulman, H.L. Stormer, and P. Kim, *Nature* **462**, 196 (2009).

[16] S. Okada, *Jpn. J. Appl. Phys.* **49**, 020204 (2010).

[17] N.T. Cuong, M. Otani, and S. Okada, *Phys. Rev. Lett.* **106**, 106801 (2011).

[18] K. Kamiya, N. Umezawa, and S. Okada, *Phys. Rev. B* **83**, 153413 (2011).

[19] Y. Takagi and S. Okada, *Jpn. J. Appl. Phys.* **51**, 085102 (2012).

[20] Y. Takagi and S. Okada, *Jpn. J. Appl. Phys.* **51**, 100203 (2012).

[21] M. Koshino and T. Ando, *Phys. Rev. B* **76**, 085425 (2007).

[22] M. Koshino and T. Ando, *Phys. Rev. B* **77**, 115315 (2008).

[23] M. Otani, M. Koshino, Y. Takagi, and S. Okada, *Phys. Rev. B* **81**, 161403(R) (2010).

[24] M. Otani, M. Koshino, Y. Takagi, and S. Okada, *Appl. Phys. Lett.* **96**, 242504 (2010).

[25] E. McCann, *Phys Rev. B* **74**, 161403 (2006).

[26] E.V. Castro, K.S. Novoselov, S.V. Morozov, N.M.R. Peres, J.M.B. Lopes dos Santos, J. Nilsson, F. Guinea, A.K. Geim, and A.H. Castro Neto, *Phys. Rev. Lett.* **99**, 216802 (2007).

[27] J.B. Oostinga, H.B. Heersche, L. Liu, A.F. Morpurgo, and L.M.K. Vandersypen, *Nature Mater.* **7**, 151 (2008).

[28] H. Miyazaki, K. Tsukagoshi, A. Kanda, M. Otani, and S. Okada, *Nano Lett.* **10**(10), 3888 (2010).

[29] M. Otani and S. Okada, *J. Phys. Soc. Jpn.* **79**, 073701 (2010).

[30] S. Konabe and S. Okada, *J. Phys. Soc. Jpn.* **81**, 113702 (2012).

[31] C.R. Dean, *Nature Nanotechnol.* **5**, 722 (2010).

[32] W. Gannett, *Appl. Phys. Lett.* **98**, 242105 (2011).

[33] P.J. Zomer, *Appl. Phys. Lett.* **99**, 232104 (2011).

[34] K.H. Lee, H.-J. Shin, J. Lee, I.-Y. Lee, G.-H. Kim, and J.-Y. Choi, *Nano Lett.* **12**, 714 (2012).

[35] J. Zhou, Q. Wang, Q. Sun, and P. Jena, *Phys. Rev. B* **81**, 085442 (2010).

[36] J. Kotakoski, C.H. Jin, O. Lehtinen, K. Suenaga, and A.V. Krasheninnikov, *Phys. Rev. B* **82**, 113404 (2010).

[37] P.P. Shinde and V. Kumar, *Phys. Rev. B* **84**, 125401 (2011).

[38] J. Beheshtian, A. Sadeghi, M. Neek-Amal, K.H. Michel, and F.M. Peeters, *Phys. Rev. B* **86**, 195433 (2012).

[39] D. Xiao, G.-B. Liu, W. Feng, X. Xu, and W. Yao, *Phys. Rev. Lett.* **108**, 196802 (2012).

[40] V. Barone, O. Hod, and G.E. Scuseria, *Nano Lett.* **6**, 2748 (2006).

[41] M. Fujita, K. Wakabayashi, K. Nakada, and K. Kusakabe, *J. Phys. Soc. Jpn.* **65**, 1920 (1996).

[42] K. Nakada, M. Fujita, G. Dresselhaus, and M.S. Dresselhaus, *Phys. Rev. B* **54**, 17954 (1996).

[43] Y. Miyamoto, K. Nakada, and M. Fujita, *Phys. Rev. B* **59**, 9858 (1999).

[44] Y. Shimomura, Y. Takane, and K. Watanabe, *J. Phys. Soc. Jpn.* **80**, 054710 (2011).

[45] N.T. Cuong, M. Otani, and S. Okada, *Phys. Rev. B* **87**, 045424 (2013).

[46] T. Enoki, M. Suzuki, and M. Endo, *Graphite Intercalation Compounds and Applications* (Oxford University Press, Oxford, U.K. 2003).

[47] M. Posternak, A. Baldereschi, A.J. Freeman, E. Wimmer, and M. Weinert, *Phys. Rev. Lett.* **50**, 761 (1983).

[48] M. Posternak, A. Baldereschi, A.J. Freeman, and E. Wimmer, *Phys. Rev. Lett.* **52**, 863 (1984).

[49] A. Catellani, M. Posternak, A. Baldereschi, and A.J. Freeman, *Phys. Rev. B* **36**, 6105 (1987).

[50] X. Blase, A. Rubio, S.G. Louie, and M.L. Cohen, *Phys. Rev. B* **51**, 6868 (1995).

[51] N.-T. Cuong, M. Otani, and S. Okada, *J. Phys: Condens. Matter* **26**, 135001 (2014).

[52] Y. Miyamoto, A. Rubio, X. Blase, M.L. Cohen, and S.G. Louie, *Phys. Rev. Lett.* **74**, 2993 (1995).

[53] S. Okada, A. Oshiyama, and S. Saito, *Phys. Rev. B* **62**, 7634 (2000).

[54] X. Blase, A. Rubio, S.G. Louie, and M.L. Cohen, *Europhys. Lett.* **28**, 335 (1994).

[55] M. Boero, K. Terakura, T. Ikeshoji, C.C. Liew and M. Parrinello, *J. Chem. Phys.* **115**, 2219 (2001).

[56] H. Conrad, G. Ertl, J. Kuppers, and E.E. Latta, *Surf. Sci.* **58**, 578 (1976).

[57] P. Heimann, H. Neddermeyer, and H.F. Roloff, *J. Phys. C* **10**, L17 (1977).

[58] S.G. Louie, *Phys. Rev. Lett.* **40**, 1525 (1978).

[59] S. Okada, Y. Enomoto, K. Shiraishi, and A. Oshiyama, *Surf. Sci.* **585**, L177 (2005).

[60] M. Otani and S. Okada, *J. Phys. Soc. Jpn.* **79**, 073701 (2010).

[61] S. Konabe and S. Okada, *J. Phys. Soc. Jpn.* **81**, 113702 (2012).

[62] M. Otani and S. Okada, *Phys. Rev. B* **83**, 073405 (2011).

[63] Q. Liu, Z. Li, and J. Yang, *Chinese J. Chem. Phys.* **24**, 22 (2011).

Chapter 2

Calculation Methods

2.1 Density Functional Theory

In N electrons system, Schrödinger equation is

$$\mathcal{H}\Psi(\mathbf{r}_1, \cdots, \mathbf{r}_N) = E\Psi(\mathbf{r}_1, \cdots, \mathbf{r}_N) \tag{2.1}$$

where

$$\begin{aligned}\mathcal{H} &= \sum_{i=1}^{N}\left(-\frac{\hbar^2}{2m}\nabla_i^2\right) + \frac{1}{2}\sum_{i\neq j}^{N}\frac{e^2}{|\mathbf{r}_i - \mathbf{r}_j|} + \sum_{i=1}^{N} v(\mathbf{r}_i) \\ &= T + U + V. \end{aligned} \tag{2.2}$$

To solve the ground state of this system, we consider the density operator as

$$\hat{n}(\mathbf{r}) = \sum_{i=1}^{N}\delta(\mathbf{r} - \mathbf{r}_i). \tag{2.3}$$

Electron density can be obtained as an expectation of a density operator

$$\begin{aligned} n(\mathbf{r}) &= (\Psi, \hat{n}\Psi) \\ &= \int \Psi^*(\mathbf{r}_1, \cdots, \mathbf{r}_N)\hat{n}(\mathbf{r})\Psi(\mathbf{r}_1, \cdots, \mathbf{r}_N)d\mathbf{r}_1 \cdots d\mathbf{r}_N. \end{aligned} \tag{2.4}$$

By using this operator, an expectation of external potential V is

$$\begin{aligned} (\Psi, V\Psi) &= \int \Psi^* \left[\sum_{i=1}^{N} v(\mathbf{r}_i)\right] \Psi d\mathbf{r}_1 \cdots d\mathbf{r}_N \\ &= \int \Psi^* \left[\int \sum_{i=1}^{N} v(\mathbf{r})\delta(\mathbf{r} - \mathbf{r}_i)d\mathbf{r}\right] \Psi d\mathbf{r}_1 \cdots d\mathbf{r}_N \\ &= \int v(\mathbf{r})n(\mathbf{r})d\mathbf{r}. \end{aligned} \tag{2.5}$$

Here, we consider the following Hohenberg–Kohn theorems [2.1].

Theorem 1

An external potential $v(\mathbf{r})$ is unique functional of the electron density $n(\mathbf{r})$ when the ground state is determined.

This theorem means that $v(\mathbf{r})$ and $\Psi(\mathbf{r}_1, \cdots, \mathbf{r}_N)$ correspond uniquely with $n(\mathbf{r})$.

$$v(\mathbf{r}) \Leftrightarrow n(\mathbf{r}) \tag{2.6}$$

In other words, all physical quantities of the ground state are functionals of the electron density. For example, energy of the ground state E can be written as

$$E_v[n(\mathbf{r})] = F[n(\mathbf{r})] + \int v(\mathbf{r})n(\mathbf{r})d\mathbf{r} \tag{2.7}$$

$$F[n(\mathbf{r})] = (\Psi, (T+U)\Psi) \tag{2.8}$$

where $F[n(\mathbf{r})]$ is a functional of $n(\mathbf{r})$ which is independent of external potential $v(\mathbf{r})$.

Theorem 2

True density $n(\mathbf{r})$ minimizes the energy of the ground state $E_v[n(\mathbf{r})]$.

The expression of the N-electron system based on these theorem is strict discussion about the ground state.

2.2 Kohn–Sham Equation

Equation (2.8) shows that $F[n(\mathbf{r})]$ is an energy functional about kinetic energy of electrons and Coulomb interaction. By using the expression of non-interacting N-electron system,

$$F[n(\mathbf{r})] = T_s[n(\mathbf{r})] + \frac{e^2}{2}\int \frac{n(\mathbf{r})n(\mathbf{r}')}{|\mathbf{r}-\mathbf{r}'|}d\mathbf{r}d\mathbf{r}' + E_{xc}[n(\mathbf{r})] \tag{2.9}$$

where $T_s[n(\mathbf{r})]$ is kinetic energy of non-interacting electron system. E_{xc} is exchange-correlation energy arising from electron-electron interaction except the Hartree energy, defined by

$$E_{xc}[n(\mathbf{r})] = \langle T\rangle + \langle U\rangle - T_s[n(\mathbf{r})] - \frac{e^2}{2}\int \frac{n(\mathbf{r})n(\mathbf{r}')}{|\mathbf{r}-\mathbf{r}'|}d\mathbf{r}d\mathbf{r}'. \tag{2.10}$$

Then, Eq. (2.7) can be rewritten as

$$E_v[n(\mathbf{r})] = T_s[n(\mathbf{r})] + \int v(\mathbf{r})n(\mathbf{r})d\mathbf{r}$$

$$+\frac{e^2}{2}\int\frac{n(\mathbf{r})n(\mathbf{r}')}{|\mathbf{r}-\mathbf{r}'|}d\mathbf{r}d\mathbf{r}'+E_{xc}[n(\mathbf{r})]. \tag{2.11}$$

Under the condition that the number of electrons is constant

$$N=\int n(\mathbf{r})d\mathbf{r}, \tag{2.12}$$

taking variation Eq. (2.11) is

$$\frac{\delta T_s[n]}{\delta n(\mathbf{r})}+v(\mathbf{r})+e^2\int\frac{n(\mathbf{r}')}{|\mathbf{r}-\mathbf{r}'|}d\mathbf{r}'+\frac{\delta E_{xc}[n]}{\delta n(\mathbf{r})}-\mu=0 \tag{2.13}$$

where μ is the Lagrange multiplier. It is led to the following self-consistent equations

$$\left[-\frac{\hbar^2}{2m}\nabla^2+v_{eff}(\mathbf{r})\right]\psi_i(\mathbf{r})=\epsilon_i\psi_i(\mathbf{r}), \tag{2.14}$$

$$n(\mathbf{r})=\sum_{i=1}^{N}|\psi_i(\mathbf{r})|^2. \tag{2.15}$$

where

$$v_{eff}(\mathbf{r})=v(\mathbf{r})+e^2\int\frac{n(\mathbf{r}')}{|\mathbf{r}-\mathbf{r}'|}d\mathbf{r}'+\frac{\delta E_{xc}[n]}{\delta n(\mathbf{r})}. \tag{2.16}$$

According to the theorems, a problem solving the ground state of the N-electron system can be interpreted the problem solving self-consistent equations (2.14) and (2.15) under the effective potential $v_{eff}(\mathbf{r})$ given by Eq. (2.16). Equation (2.14) is known to be the Kohn–Sham equation [2.2]. However, this can not be solved because the functional form of $E_{xc}[n(\mathbf{r})]$ is unknown. For practical application of Kohn–Sham equation, appropriate approximations of $E_{xc}[n(\mathbf{r})]$ are necessary.

2.3 Local Density Approximation

In local density approximation [2.3, 2.4], we consider that density of exchange-correlation energy can be written as the product of the local exchange-correlation density of the homogeneous electron gas ϵ_{xc} and its density $n(\mathbf{r})$.

$$E_{xc}[n(\mathbf{r})]=\int\epsilon_{xc}[n(\mathbf{r})]n(\mathbf{r})d\mathbf{r} \tag{2.17}$$

Therefore, the local density approximation is strict in many-electron system in which electron density is homogeneous.

When exchange correlation energy is expressed as (2.17), functional differential of the density, which comparable to exchange correlation potential of electrons, is also local expression as

$$\mu_{xc}(\mathbf{r}) = \frac{\delta E_{xc}[n(\mathbf{r})]}{\delta n(\mathbf{r})} = \left.\frac{d(\epsilon_{xc}(n)n)}{dn}\right|_{n=n(\mathbf{r})}. \tag{2.18}$$

Then, (2.16) become

$$v_{eff}(\mathbf{r}) = v(\mathbf{r}) + e^2 \int \frac{n(\mathbf{r}')}{|\mathbf{r}-\mathbf{r}'|} d\mathbf{r}' + \mu_{xc}(\mathbf{r}). \tag{2.19}$$

2.4 Generalized Gradient Approximation

In generalized gradient approximation [2.5,2.6], gradient of electron density is included to improve the accuracy of calculation.

$$E_{xc}[n(\mathbf{r})] = \int f[n(\mathbf{r}), |\nabla n(\mathbf{r})|] d\mathbf{r} \tag{2.20}$$

Because of inhomogeneous distribution of electron density in real system, generalized gradient approximation with judiciously choice f, which must be parameterized analytic functions, can improve the physical quantities of atoms, molecules, and solids obtained by the local density approximation.

2.5 Pseudopotential

In practical calculations using density functional theory (DFT) on real materials, it takes large computational cost for treating all atomic potentials because high energy wave functions are necessary to express core region. A concept of pseudopotential is reduction of computational cost without decrease in accuracy of valence electron states by replacing the deep potential at core region with the shallow pseudopotential.

Let us start with the Schrödinger equation

$$\hat{\mathcal{H}} |\psi_n\rangle = E_n |\psi_n\rangle \tag{2.21}$$

with $n = c, v$ which denote the core and valence electrons. To express the valence wave functions $|\psi_v\rangle$ by smooth functions $|\phi_v\rangle$, which is called pseudo wave functions, $|\psi_v\rangle$ is written as

$$|\psi_v\rangle = |\phi_v\rangle + \sum_c |\psi_c\rangle \langle\psi_c|\phi_v\rangle. \tag{2.22}$$

Then, Eq. (2.21) become

$$\hat{\mathcal{H}} |\phi_v\rangle = E_v |\phi_v\rangle + \sum_c (E_c - E_v) |\psi_c\rangle \langle\psi_c|\phi_v\rangle \tag{2.23}$$

This equation means that the pseudo wave functions $|\phi_v\rangle$ satisfy the Schrödinger equation with the pseudopotential $\hat{V}^{PP}$:

$$(\hat{T} + \hat{V}^{PP})\,|\phi_v\rangle = E_v\,|\phi_v\rangle \tag{2.24}$$

where

$$\hat{V}^{PP} = \hat{V} - \sum_c (E_c - E_v)\,|\psi_c\rangle\,\langle\psi_c| \tag{2.25}$$

where $\hat{V}$ is the true potential.

In this thesis, we use the ultrasoft pseudopotential developed by Vanderbilt [2.7]. An all-electron calculation is carried out on a free atom in some reference configuration, leading to a screened potential $V^{AE}(r)$ and the all-electron wave function $\left|\psi_i^{AE}\right\rangle$:

$$(T + V^{AE} - \epsilon_i)\left|\psi_i^{AE}\right\rangle = 0 \tag{2.26}$$

where i is a set of quantum number $\{nlm\}$. The pseudo wave function $|\phi_i\rangle$ and the local pseudopotential V_{loc} is constructed under constraint that they smoothly join to $\left|\psi_i^{AE}\right\rangle$ and V^{AE} at cutoff radius r_c:

$$\phi_i(r) = \psi_i^{AE}(r) \qquad (r \geq r_c), \tag{2.27}$$

$$V_{loc}(r) = V^{AE}(r) \qquad (r \geq r_c). \tag{2.28}$$

The local wave function, which vanishes at and beyond R where all pseudo– and all-electron quantities agree, is defined as

$$|\chi_i\rangle = (\epsilon_i - T - V_{loc})\,|\phi_i\rangle \tag{2.29}$$

and then, forming the matrix of inner products

$$B_{ij} = \langle\phi_i|\chi_j\rangle \tag{2.30}$$

and defining a set of local wave functions, which are dual to the $|\phi_i\rangle$,

$$|\beta_i\rangle = \sum_j (B^{-1})_{ji}\,|\chi_j\rangle \tag{2.31}$$

where j is a composite index as i. The deficit charge density is defined as

$$Q_{ij}(\mathbf{r}) = \psi_i^{*AE}(\mathbf{r})\psi_j^{AE}(\mathbf{r}) - \phi_i^*(\mathbf{r})\phi_j(\mathbf{r}) \tag{2.32}$$

$$Q_{ij} = \int d^3r Q_{ij}(\mathbf{r}) \tag{2.33}$$

and the matrix D_{ij} is constructed as

$$D_{ij} = B_{ij} + \epsilon_j Q_{ij}. \tag{2.34}$$

It is straightforward to verify that the $|\phi_k\rangle$ obey the secular equation:

$$\left(T + V_{loc} + \sum_{ij} D_{ij} |\beta_i\rangle \langle\beta_i| \right) |\phi_k\rangle = \epsilon_k \left(1 + \sum_{ij} Q_{ij} |\beta_i\rangle \langle\beta_i| \right) |\phi_k\rangle \tag{2.35}$$

where k is a composite index as i and j.

2.6 Effective Screening Medium Method

In conventional first-principles calculation, Poisson equation, which express the electrostatic interaction, is solved under periodic boundary condition. However, we can not obtain reasonable results because of the unphysical dipole interaction with the image cells in the case of electrostatic potentials do not connect to each other at the cell boundaries, arising from the external electric field, polarity of the target materials, and so on. The Effective screening medium (ESM) method [2.8] can overcome the problem by considering the semi-infinite media of appropriate permittivity at the cell boundaries.

As ordinary DFT calculations, wave functions are solved under the periodic boundary condition with cell length of $2z_0$, where the electrons are confined to the region $z \in [-z_0, z_0]$, in ESM method. The total-energy functional is modified as

$$E[\rho_e, V] = T[\rho_e] + E_{xc}[\rho_e] - \int d\mathbf{r} \left[\frac{\epsilon(\mathbf{r})}{8\pi} |\nabla V(\mathbf{r})|^2 + \rho_{tot}(\mathbf{r}) V(\mathbf{r}) \right] \tag{2.36}$$

where $\rho_{tot}(\mathbf{r})$ and $V(\mathbf{r})$ denote the total charge density and the electrostatic potential, respectively. By taking the variation by electrostatic potential, we can get a modified Poisson equation

$$\nabla \cdot [\epsilon(\mathbf{r})\nabla] V(\mathbf{r}) = -4\pi\rho_{tot}(\mathbf{r}). \tag{2.37}$$

This Poisson equation contains spatially nonuniform relative permittivity. By introducing the Green's function, the Poisson equation becomes

$$\nabla \cdot [\epsilon(\mathbf{r})\nabla] G(\mathbf{r}, \mathbf{r}') = -4\pi\delta(\mathbf{r} - \mathbf{r}'). \tag{2.38}$$

Then, electrostatic potential $V(\mathbf{r})$ is expressed as

$$V(\mathbf{r}) = \int d\mathbf{r}' G(\mathbf{r}, \mathbf{r}') \rho_{tot}(\mathbf{r}'). \tag{2.39}$$

Here, we assumed that the relative permittivity only depends on z. Then, the Poisson equation

$$\{\partial_z[\epsilon(z)\partial_z] + \epsilon(z)\nabla_{\parallel}^2\}G(\mathbf{r}_{\parallel} - \mathbf{r}'_{\parallel}, z, z') = -4\pi\delta(\mathbf{r}_{\parallel} - \mathbf{r}'_{\parallel})\delta(z - z'), \tag{2.40}$$

becomes

$$\partial_z[\epsilon(z)\partial_z] - \epsilon(z)\mathrm{g}_{\parallel}^2 G(\mathbf{g}_{\parallel}, z, z') = -4\pi\delta(z - z'), \tag{2.41}$$

where $\mathbf{g}_{\parallel}$ and $\mathrm{g}_{\parallel}$ denote the wave vector parallel to the surface and absolute value of $\mathbf{g}_{\parallel}$. Green's function is determined under appropriate boundary conditions. In this thesis, we use the following two boundary conditions.

(i) Open boundary condition
$\partial_z V(\mathbf{g}_{\parallel}, z)|_{z=\pm\infty} = 0, \qquad \epsilon(z) = 1;$

(ii) Metal/vacuum/metal condition
$V(\mathbf{g}_{\parallel}, z_1) = 0, \qquad \epsilon(z) = \begin{cases} 1 & \text{if } |z| \leq z_1 \\ \infty & \text{if } |z| \geq z_1 \end{cases};$

Note that, in condition (ii), we can apply electric field to the system by setting the potential difference between two ESMs.

References

[1] P. Hohenberg and W. Kohn, *Phys. Rev.* **136**, B864 (1964).

[2] W. Kohn and L.J. Sham, *Phys. Rev.* **140**, A1133 (1965).

[3] J.P. Perdew and A. Zunger, *Phys. Rev. B* **23**, 5048 (1981).

[4] D.M. Ceperley and B.J. Alder, *Phys. Rev. Lett.* **45**, 566 (1980).

[5] J.P. Perdew, K. Burke, and M. Ernzerhof, *Phys. Rev. Lett.* **77**, 3865 (1996).

[6] J.P. Perdew, K. Burke, and M. Ernzerhof, *Phys. Rev. Lett.* **78**, 1396 (1997).

[7] D. Vanderbilt, *Phys. Rev. B* **41**, 7892 (1990).

[8] M. Otani and O. Sugino, *Phys. Rev. B* **73**, 115407 (2006).

Chapter 3

Geometric and Electronic Properties of Graphene Edges

3.1 Introduction

In recent years, graphene has attracted much attention in the fields of nanoscience and nanotechnology because of its unique electronic and geometric properties [3.1, 3.2]. A honeycomb network of sp^2 C atoms with single-atom thickness causes a pair of linear dispersion bands at the Fermi level (E_F) [3.3], leading to peculiar physical properties such as the unusual quantum Hall effect [3.4–3.7]. On the other hand, the electronic structure of graphene is known to be fragile with respect to external perturbations such as insulating substrates [3.8–3.10], metal electrodes [3.11, 3.12], other graphene/graphite layers [3.13–3.16], and an external electric field [3.17–3.22]. For example, graphene has an energy gap of a few tens of meV when adsorbed on SiO_2 surfaces [3.9]. Bilayer graphene possesses quadric dispersion bands at the E_F with zero band gap, rather than the linear dispersion band, that are tunable from metallic to semiconducting by applying a normal electric field [3.17–3.22]. In addition to the hybrid structure perpendicular to the layer, hybrid structures within the layer also affect their electronic properties. Atomic defects and edges are regarded as negative foreign atoms, which strongly modulate the electronic structure of graphene [3.23–3.28]. Furthermore, heterogeneous sheets with h-BN also modulate the characteristic electronic structure of graphene [3.29]. These are serious problems when incorporating graphene as an emerging material in future nanoscale devices because some of these hybrid structures are inherent and essential in such devices.

To utilize graphene for the devices, it is important to precisely control their geometric and electronic structures under hybrid structures with foreign materials and external environments. The geometric and electronic structures of graphene edges have been intensively studied for the past two decades because edges are the one of important procedures for electronic structure tuning and functionalization of graphene [3.30]. It is well known that graphene nanoribbons possess peculiar electronic structures depending on their width and edge atomic arrangements: graphene nanoribbons with zigzag edges possess edge localized states known as edge states [3.23–3.26, 3.29] arising from the topological condition, while ribbons with armchair edges have either metallic or semiconducting properties depending on the discretized conditions imposed on graphene. Additionally, the edge roughness induces further variations in their electronic structures [3.31, 3.32]. The energetics of graphene nanoribbons in terms of the edge structures has been also theoretically studied. Previous theoretical works have pointed out that the armchair edge is energetically more stable than the zigzag edge because of the small density of states (DOS) at the E_F [3.32–3.37]. However, despite much effort devoted to elucidate the energetics and electronic structure of the edges of graphene [3.32–3.38], the correlation between energetics and electronic structures of graphene nanoribbons with respect to the edge atomic structures is still not fully understood.

Among the various external factors that can form hybrid structures with graphene, electric fields are one of the main factors determining the electronic properties of graphene in device structures. Because an electric field is essential for operating and functionalizing electronic devices, it is necessary to understand the fundamental behavior of graphene under the influence of electric fields. There have been several theoretical studies investigating the fundamental properties of graphene under normal electric fields [3.20–3.22]. However, it is still unknown how the electronic properties of graphene are influenced by a lateral electric field [3.39, 3.40]. In the case of carbon nanotubes, which are tubular structure of graphene sheets, screening against an external electric field strongly depends on local atomic arrangement [3.45–3.47]. Therefore, because of the similarity of the local atomic structures of graphene to carbon nanotubes, graphene is also expected to exhibit unusual field screening against a lateral electric field.

In this chapter, we show the edge stability and the electronic structures of graphene nanoribbons with various edge shapes, from armchair to zigzag edges, with and without hydrogen termination. In addition, we also show the electronic properties of graphene nanoribbons with various edge angles under a parallel electric field to give theoretical insight into the fundamental issues for utilizing graphene in electronic devices, because the external electric field is essential for functionalizing graphene nanoribbons as in electronic device structures.

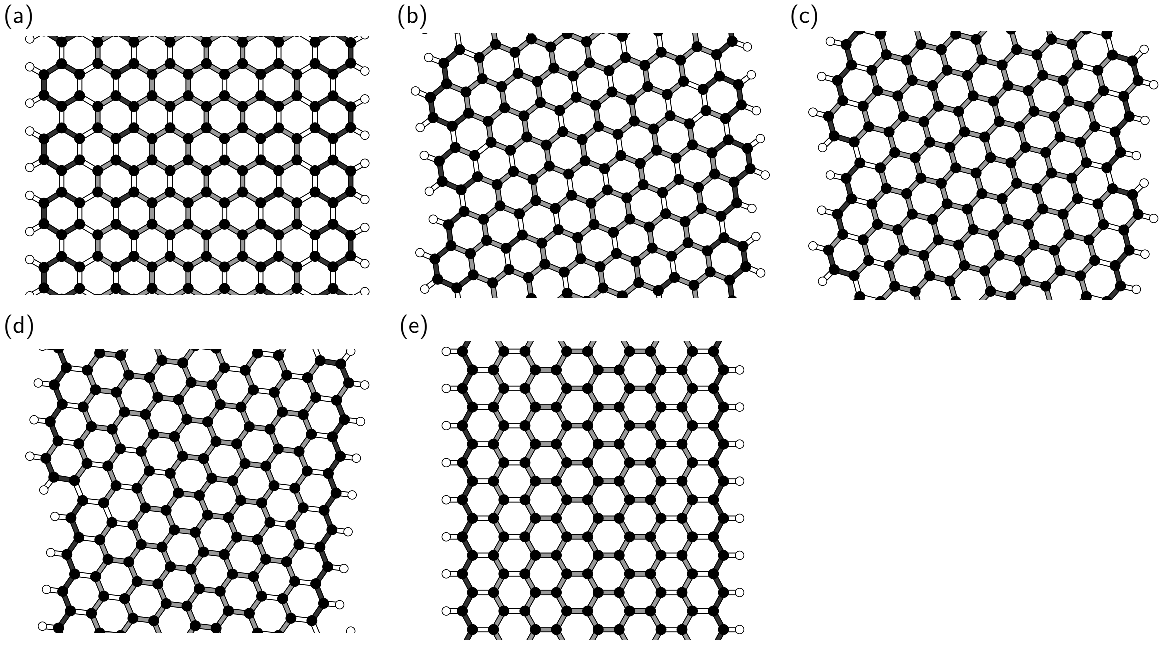

Figure3.1 Optimized geometries of graphene nanoribbons with (a) armchair edge ($\theta = 0°$), chiral edges (b) $\theta = 8°$, (c) $\theta = 16°$, (d) $\theta = 23°$, and (e) zigzag edge ($\theta = 30°$). Black and white circles denote carbon and hydrogen atoms, respectively. Dark shaded, pale shaded, and white bonds indicate short (–1.41 Å), medium (1.41–1.42 Å), and long (1.42 Å–) bonds, respectively. White bonds situated at the edge of the nanoribbons correspond to C–H bonds.

3.2 Energetics and Electronic structure

We considered several edge structures between armchair and zigzag of graphene to investigate the energetics and electronic structures of graphene edges. To simulate graphene edges with various edge shapes, we considered nanoribbons with hydrogenated and clean edges with edge angles of 0 (armchair), 8, 16, 23, and 30° (zigzag) (Figs. 3.1 and 3.2). To make quantitative discussion of the energetics of the nanoribbons with various edge shapes, the ribbons possessed similar widths and unit lengths of about 1.8–2.1 and 1.7–2.0 nm, respectively. The geometric structures of graphene nanoribbons were optimized until the force acting on atoms was less than 0.005 Ry/Å under the fixed lattice parameter along the ribbons, which was determined by the bulk bond length of 1.42 Å.

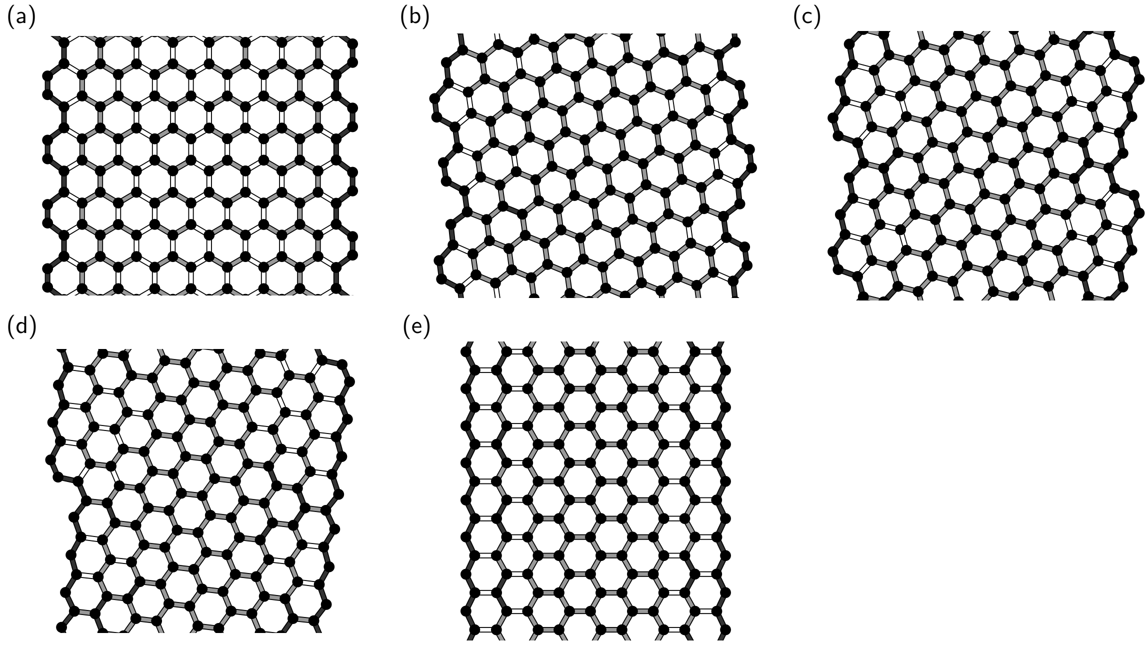

Figure3.2 Optimized geometries of graphene nanoribbons with (a) armchair edge ($\theta = 0°$), chiral edges (b) $\theta = 8°$, (c) $\theta = 16°$, (d) $\theta = 23°$, and (e) zigzag edge ($\theta = 30°$). Black circles denote carbon atoms. Dark shaded, pale shaded, and white bonds indicate short (–1.41 Å), medium (1.41–1.42 Å), and long (1.42 Å–) bonds, respectively.

3.2.1 Hydrogenated Edges

Figure 3.1 shows the optimized structures of hydrogenated graphene nanoribbons with various edge angles. In all cases, the bond lengths of nanoribbons are not equivalent to each other: covalent bonds associated with hydrogenated carbon atoms are found to be shorter than the other bonds. The optimized bond lengths are 1.37 Å or shorter. This short bond length is ascribed to the environment arising from the hydrogen atoms attached to the carbon atoms. In this case, because of the chemical species difference, one of three bonds of the carbon atoms is not equivalent to the remaining two. The bonds adjacent to these short bonds are basically longer than the initial bond length of 1.42 Å. For ribbons with near-armchair edges, there is a clear bond alternation with respect to the C_2 dimer rows along the ribbon direction. This bond alternation leads to stepwise screening against the external electric field, which will be discussed later. In contrast, for ribbons with near-zigzag edges, bond alternation rapidly decreases approaching an inner region of the ribbons. Indeed, the bond length at the center of the ribbons is almost equivalent to the initial length of 1.42 Å.

Figure 3.3(a) shows the edge formation energy of hydrogenated graphene nanorib-

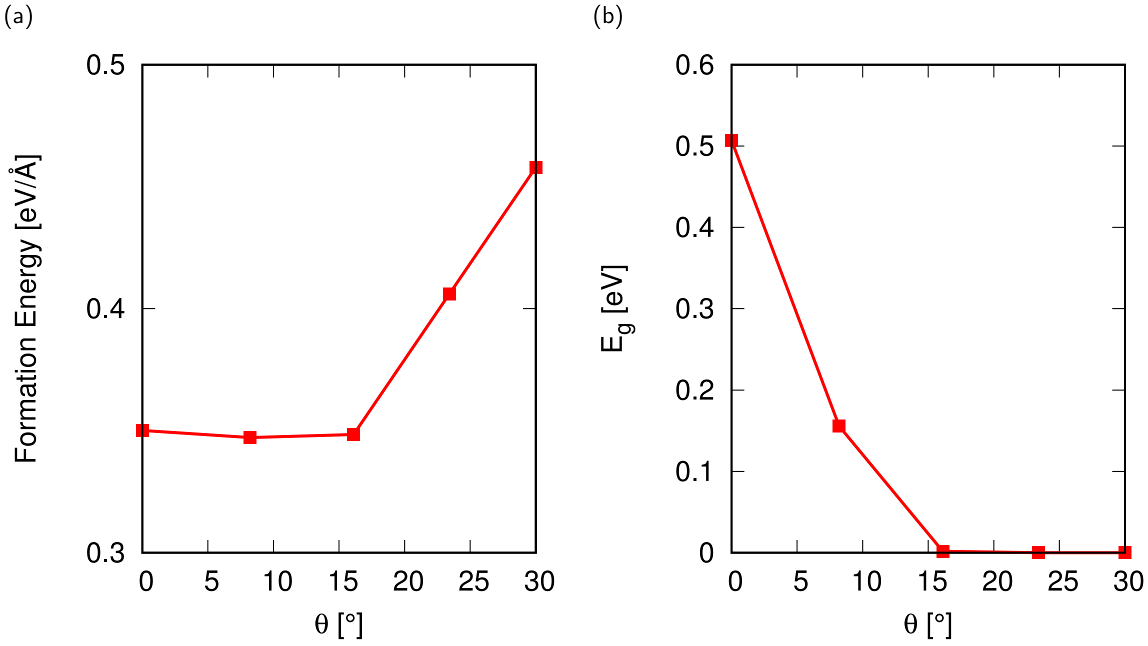

Figure3.3 (a) Edge formation energy and (b) energy gap of hydrogenated graphene nanoribbons as a function of the edge angle θ.

bons as a function of the edge angle. The edge formation energy E_{edge} is evaluated using the following formula:

$$E_{\mathrm{edge}} = (E_{\mathrm{total}} - N_{\mathrm{C}}\mu_{\mathrm{C}} - N_{\mathrm{H}}\mu_{\mathrm{H}})/L_{\mathrm{edge}} \tag{3.1}$$

where E_{total}, N_{C}, N_{H}, μ_{C}, μ_{H}, and L_{edge} denote the total energy of ribbons, the number of carbon atoms, the number of hydrogen atoms, the chemical potential of carbon atoms, the chemical potential of hydrogen atoms, and the edge length in a unit cell, respectively. The chemical potentials of carbon and hydrogen atoms are evaluated by the total energies per atom of graphene and hydrogen in benzene molecules, respectively. As shown in Fig. 3.3(a), the edge formation energy remains constant up to $\theta = 16^\circ$. Because the edge formation energy remains constant up to the edge angle of 16°, the graphene flakes preferentially possess armchair edges with a small portion of zigzag edges. This result implies that the armchair edges of graphene inherently possess edge roughness, containing zigzag edges under thermal equilibrium conditions. In sharp contrast, above the critical angle of $\theta = 16^\circ$, the edge formation energy rapidly increases with increasing edge angle, so that the edge formation energy sensitively correlates with the portion of perfect zigzag edges [3.38]. This fact corroborates that the edges of graphene prefer armchair or near-armchair shapes over a zigzag shape. However, it is well known that the graphene with zigzag edges have been occasionally observed in transmission electron microscope and scanning tunneling microscope experiments. These implies that the edge shape of graphene flakes strongly depends on their formation process. Note that it has been reported that the formation energy of hydrogenated nanoribbons with armchair and zigzag edges is almost constant with respect to the ribbon width except ribbons narrower than 10 Å [3.34].

Figure 3.3(b) shows the energy gap between the highest occupied (HO) and the lowest unoccupied (LU) states of graphene nanoribbons studied here. We found that graphene nanoribbons with edge angles up to 15° are semiconductors. From armchair to the edge angle of 15°, the band gap monotonically decreases with increasing edge angle. Finally, at 16°, the graphene nanoribbon is a zero gap semiconductor. Furthermore, nanoribbons with near-zigzag edges are metals. By comparing Figs. 3.3(a) and 3.3(b), we found a correlation between the edge formation energy and the energy gap: semiconducting graphene nanoribbons have small edge formation energy. It should be noted that the edge formation energy is insensitive to the detailed electronic structure of the graphene nanoribbons with a finite energy gap [3.34]. On the other hand, metallic graphene nanoribbons have higher edge formation energy which increase with increasing the edge angle. Thus, the energetics of graphene edges with near zigzag shapes depends on their detailed electronic structures.

Figure 3.4 shows the electronic structure of hydrogenated graphene nanoribbons with various edge angles. The HO and LU states lose their dispersion with increasing edge angle. We found a pair of flat bands around the Γ point at the E_F for graphene nanoribbons of which edge angle θ equals to or larger than 16°. The flat band region monotonically increases with increasing edge angle. Indeed, in the ribbon with the edge angle of $\theta = 23°$, the HO and LU states are perfectly degenerated and have flat dispersion throughout the Brillouin zone. In the case of $\theta = 30°$, we found that four flat dispersion bands including HO and LU states emerge at the E_F. Thus, the number of states at the E_F monotonically increases with increasing edge angle θ from 16 to 30°. This is the origin of the increase in the edge formation energy of the near-zigzag edges, as the large number of states at the E_F leads to instability for the electron system. Note that we impose eight times periodicities along the ribbon direction for the ribbon with zigzag edges to guarantee numerical accuracy for comparing the total energies of ribbons in these calculations. Thus, flat band states associated with the edge states are folded multiple times into the Γ point.

The flat band nature of the HO and LU states implies that these states possess an edge state nature [3.23–3.25, 3.29]. To unravel the origin of the flat band states, we investigate the wave function of the electron states near the E_F. Figure 3.5 shows the contour plots of squared wave functions of the electronic states at the Γ point within the energy range from $E_F - \Delta$ to $E_F + \Delta$, where $\Delta = 0.2$ eV. For graphene nanoribbons with armchair edges, the states extend throughout the ribbon, showing

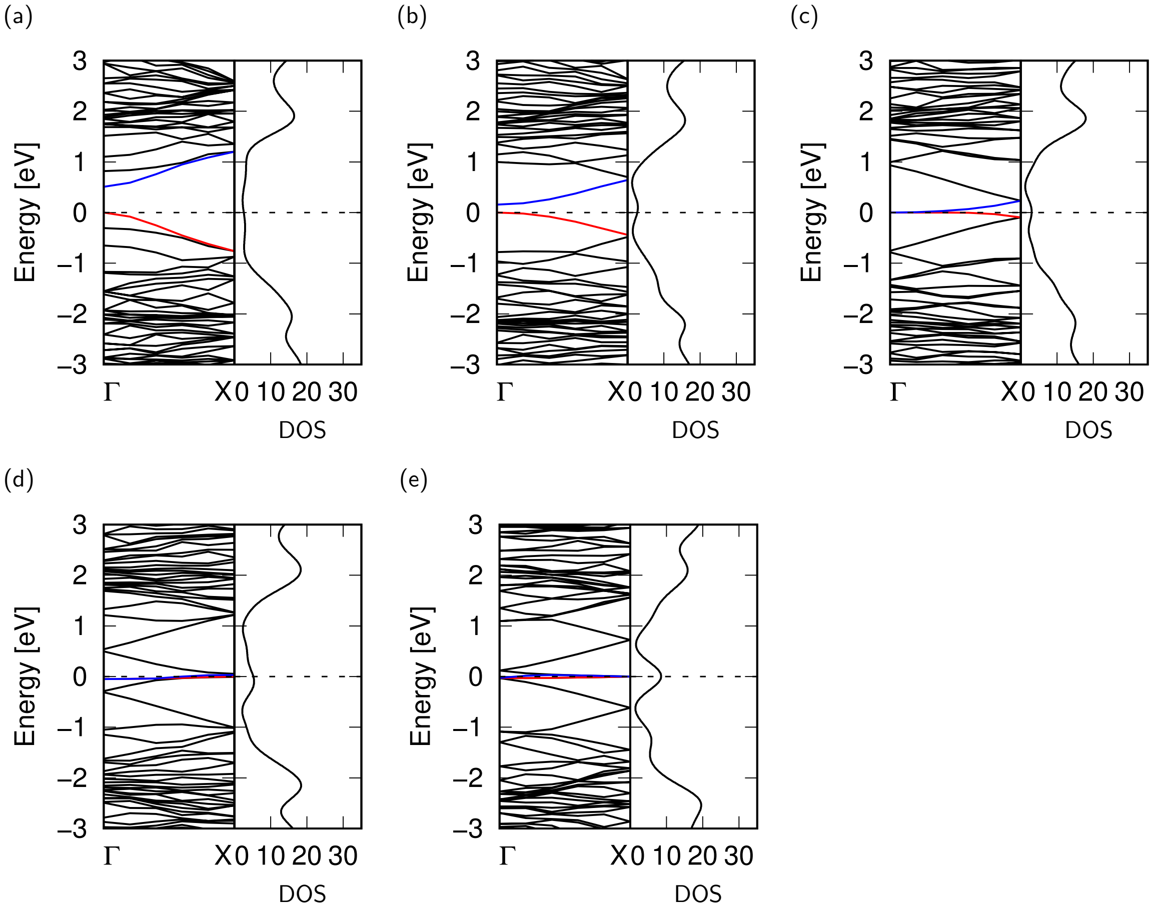

Figure3.4 Electronic structure and density of states (DOS) of hydrogenated graphene nanoribbons. Each figure denote the nanoribbons with (a) armchair edge ($\theta = 0°$), chiral edges (b) $\theta = 8°$, (c) $\theta = 16°$, (d) $\theta = 23°$, and (e) zigzag edge ($\theta = 30°$). Red and blue lines indicate the highest occupied state and lowest unoccupied state, respectively. Energies are measured from the E_F and the top of the valence bands for metallic and semiconducting nanoribbons, respectively. Unit of DOS is states/eV.

the conventional π electron nature. However, the wave functions of the nanoribbons with edge angle $\theta = 8°$ show a localized nature near the edge atomic site. With further increase in the edge angle, the wave functions are more concentrated at the edge atomic site in the nanoribbons, as in the case of edge angles of $\theta = 16$ and $23°$, indicating their edge state nature. For graphene nanoribbons with zigzag edges, $\theta = 30°$, the states are perfectly localized at the edge atomic sites. Therefore, the flat dispersion bands in the graphene nanoribbons with finite edge angles θ are classified as edge states. These facts indicate that the edge states are basically observed on the various graphene flakes of ribbons in scanning tunneling microscope experiments because the edge roughness is inherent in graphene edges with respect to the energetics.

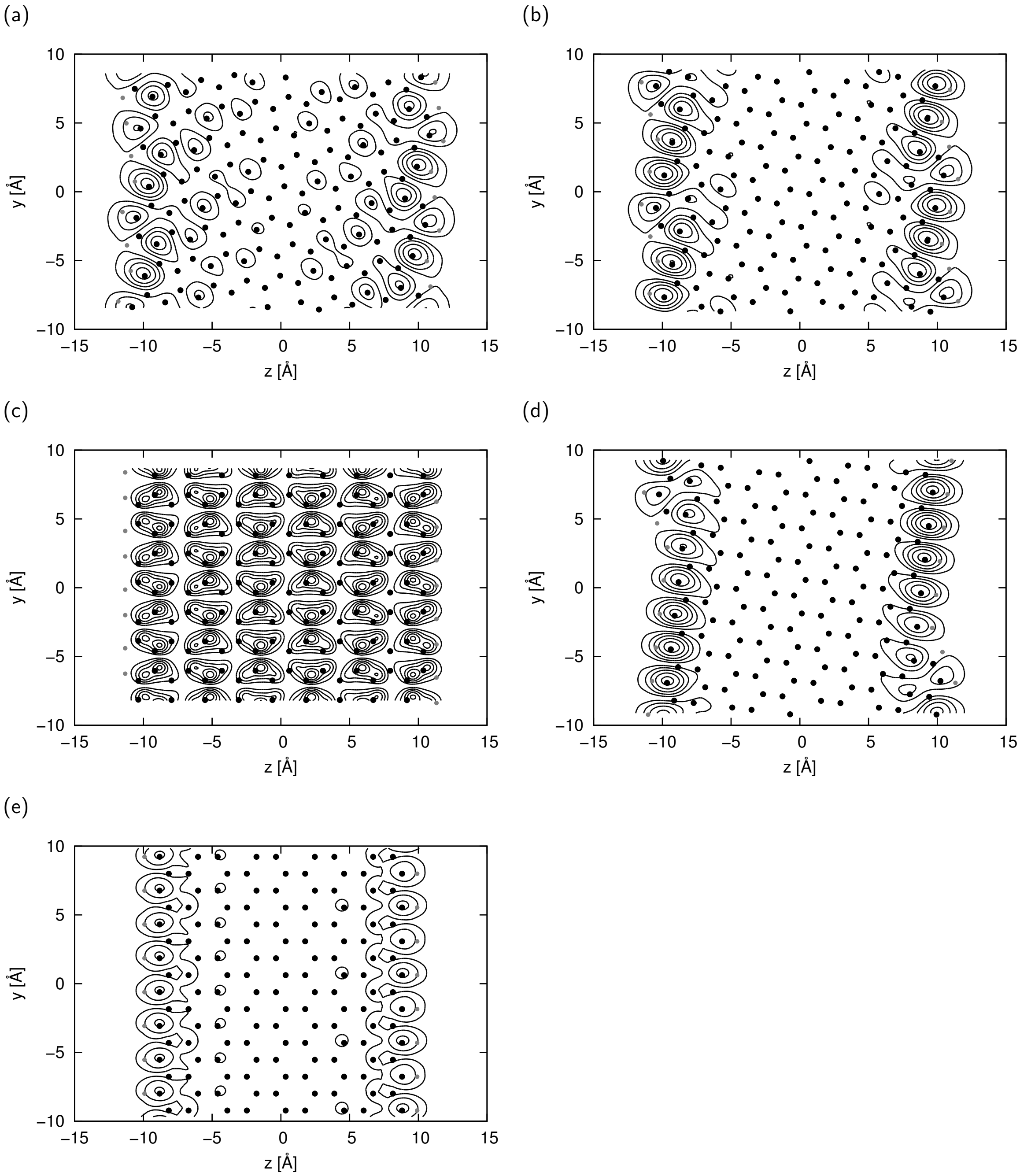

Figure3.5 Contour plots of wave functions at the Γ point near the E_F of hydrogenated graphene nanoribbons. Each figure denote the nanoribbons with (a) armchair edge ($\theta = 0°$), chiral edges (b) $\theta = 8°$, (c) $\theta = 16°$, (d) $\theta = 23°$, and (e) zigzag edge ($\theta = 30°$).

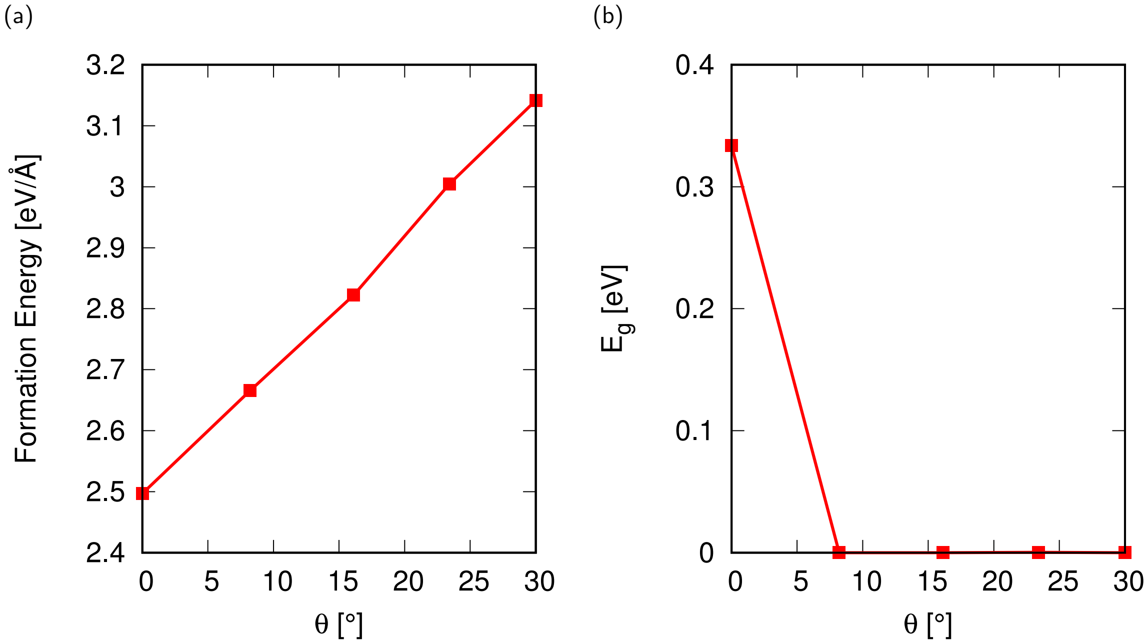

Figure3.6 (a) Edge formation energy and (b) energy gap of graphene nanoribbons with clean edges as a function of the edge angle θ.

3.2.2 Clean Edges

We discuss the geometric and electronic structures of graphene nanoribbons with clean edges. Fig. 3.2 shows the optimized geometries of graphene nanoribbons with clean edges of which angles are θ=0 (armchair), 8, 16, 23, and 30° (zigzag). In all nanoribbons with any edge angles, structural reconstruction occurs at the edge atoms to reduce electron energy arising from the dangling bonds with increasing lattice energies. In particular, the bonds forming the armchair edge are remarkably shrunken by the structural reconstruction. The calculated bond length is about 1.23 Å, possessing an sp nature rather than sp^2. This value is consistent with an early calculation on armchair ribbons with clean edges [3.41]. In the case of zigzag edges, the relaxed bond length near the edges is still shorter than that of conventional sp^2 bonds.

Because of the dangling bonds at the edge atomic sites, it is thought that the clean edges are more unstable than the hydrogenated edges. Figure 3.6(a) shows the edge formation energies of graphene nanoribbons with clean edges as a function of the edge angles evaluated by the following equation.

$$E_{\text{edge}} = (E_{\text{total}} - N_{\text{C}}\mu_{\text{C}})/L_{\text{edge}} \tag{3.2}$$

where E_{total}, N_{C}, μ_{C}, and L_{edge} denote the total energy of ribbons, the number of carbon atoms, the chemical potential of carbon atoms evaluated with respect to the graphene energy, and the edge length of a unit cell, respectively. As shown in Fig. 3.6(a), the formation energy of clean edges is 7 to 8 times larger than that of hydrogenated edges. In contrast to nanoribbons with hydrogenated edges, the edge formation energy monotonically increases with increasing edge angle without any plateaus. By analogy with the relation between edge formation energies and electronic structure in hydrogenated edges, the monotonic increase of the edge energy implies that nanoribbons with clean edges are metals with a number of electron states near the E_F.

Figure 3.6(b) shows the energy gap of graphene nanoribbons with clean edges. In contrast to nanoribbons with hydrogenated edges, we found that the ribbon with armchair edges is a semiconductor, while the others are all metals. The semiconducting nature of the armchair ribbons makes the armchair edge the most energetically stable edge among the five edge angles. In the case of nanoribbons with armchair edges, as stated above, the edge carbon atoms are tightly dimerized with each other, forming a short bond of which length is 1.23 Å. Because of this strong dimerization, these atoms possess an sp nature, rather than sp^2, so they do not possess dangling bonds even though they are not terminated by hydrogen atoms. By focusing on the detailed edge atomic arrangement for the finite edge angles, we find that the armchair regions of these edges tend to form a C-C dimer with a short bond length of 1.2 Å. Thus, the monotonic increase in the edge formation energy is ascribed to the decrease in the amount of C-C dimer structures at the edges.

By comparing Figs. 3.6(a) and 3.6(b), as in the case of hydrogenated edges, we also found a correlation between edge formation energy and energy gap in the case of clean edges. Semiconducting armchair nanoribbons have the smallest edge formation energy. For the other metallic nanoribbons, the edge formation energy is larger than that of the armchair nanoribbon.

Figure 3.7 shows the electronic structure of nanoribbons with clean edges. Comparing with the electronic structures of nanoribbons with hydrogenated edges, nanoribbons with clean edges have extra states near the E_F, of which the dispersion is very small, arising from the dangling bonds of carbon atoms situated at the edges. Because of the localized nature of the dangling bonds, these states are basically degenerate each other. As stated above, the dangling bonds are absent at the atomic sites associated with the armchair edges. Thus, the increase in the states corresponds to that of the portion of zigzag edges. Because of the edge states and dangling bond states, the number of states at the E_F monotonically increases with increasing edge angle θ from 8 to 30°. As in the case of hydrogenated nanoribbons, this large number of states at the E_F induces instability in edges with angles θ from 8 to 30°.

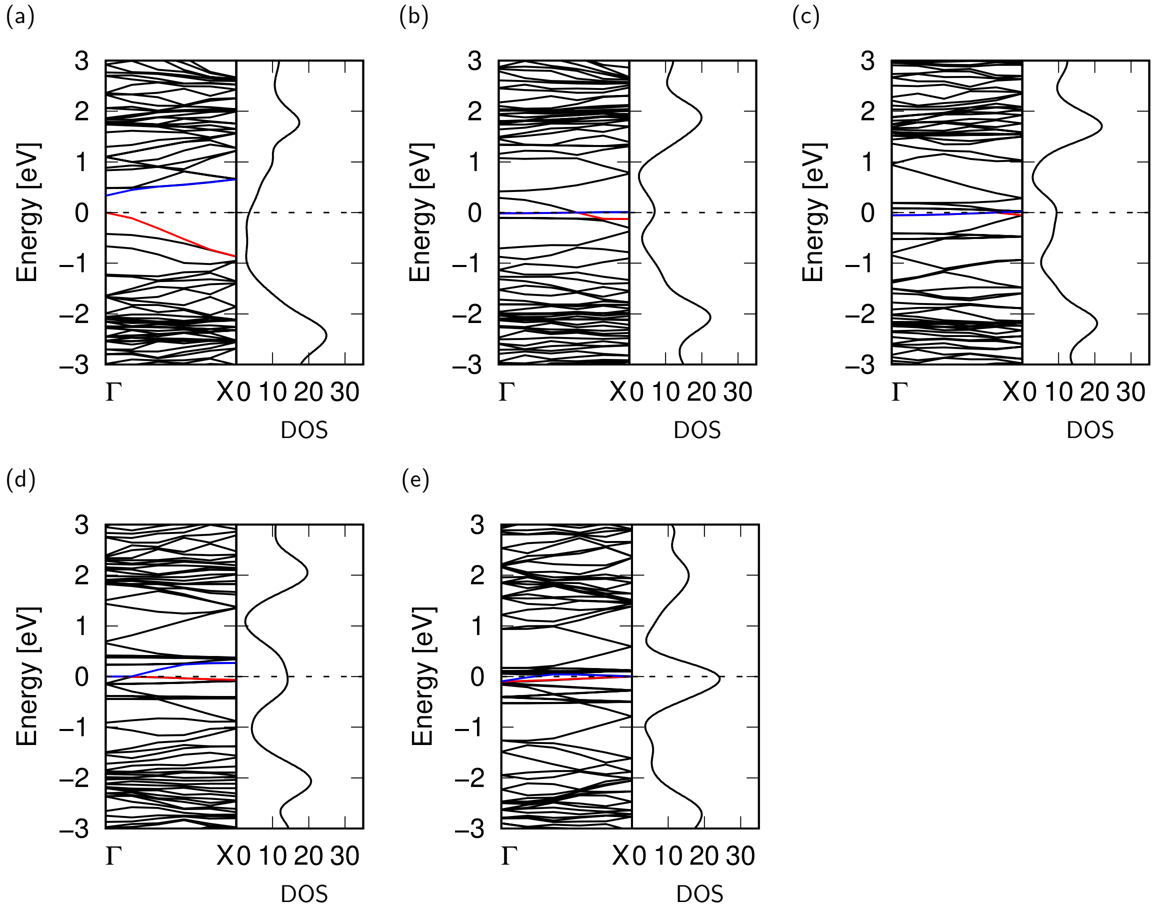

Figure3.7 Electronic structures and density of states (DOS) of graphene nanoribbons with clean edges. Each figure denote the nanoribbons with (a) armchair edge ($\theta = 0°$), chiral edges (b) $\theta = 8°$, (c) $\theta = 16°$, (d) $\theta = 23°$, and (e) zigzag edge ($\theta = 30°$). Red and blue lines indicate the highest occupied state and lowest unoccupied state, respectively. Energies are measured from the E_F. Unit of DOS is states/eV.

It is worth investigating the detailed properties of the flat band states that appeared around the E_F. To unravel the origin of the states, we calculate the wave function of the electron states near the E_F. Fig. 3.8 shows the squared wave function of nanoribbons with edge angles of 0, 8, 16, 23, and 30° at the Γ point near the E_F. In the case of the nanoribbon with armchair edges, the states extend throughout the ribbons, revealing their π and π^* natures. On the other hand, for nanoribbons with finite edge angles except $\theta = 30°$, the wave functions are localized and distributed aside on the edge atomic sites, especially constituting of zigzag shapes. Thus, the states are classified as dangling bond states arising from the unsaturated covalent bond of carbon atoms at the apex of the edge with zigzag shapes. It should be noted that such states are absent at the atomic sites belonging to the edge with armchair

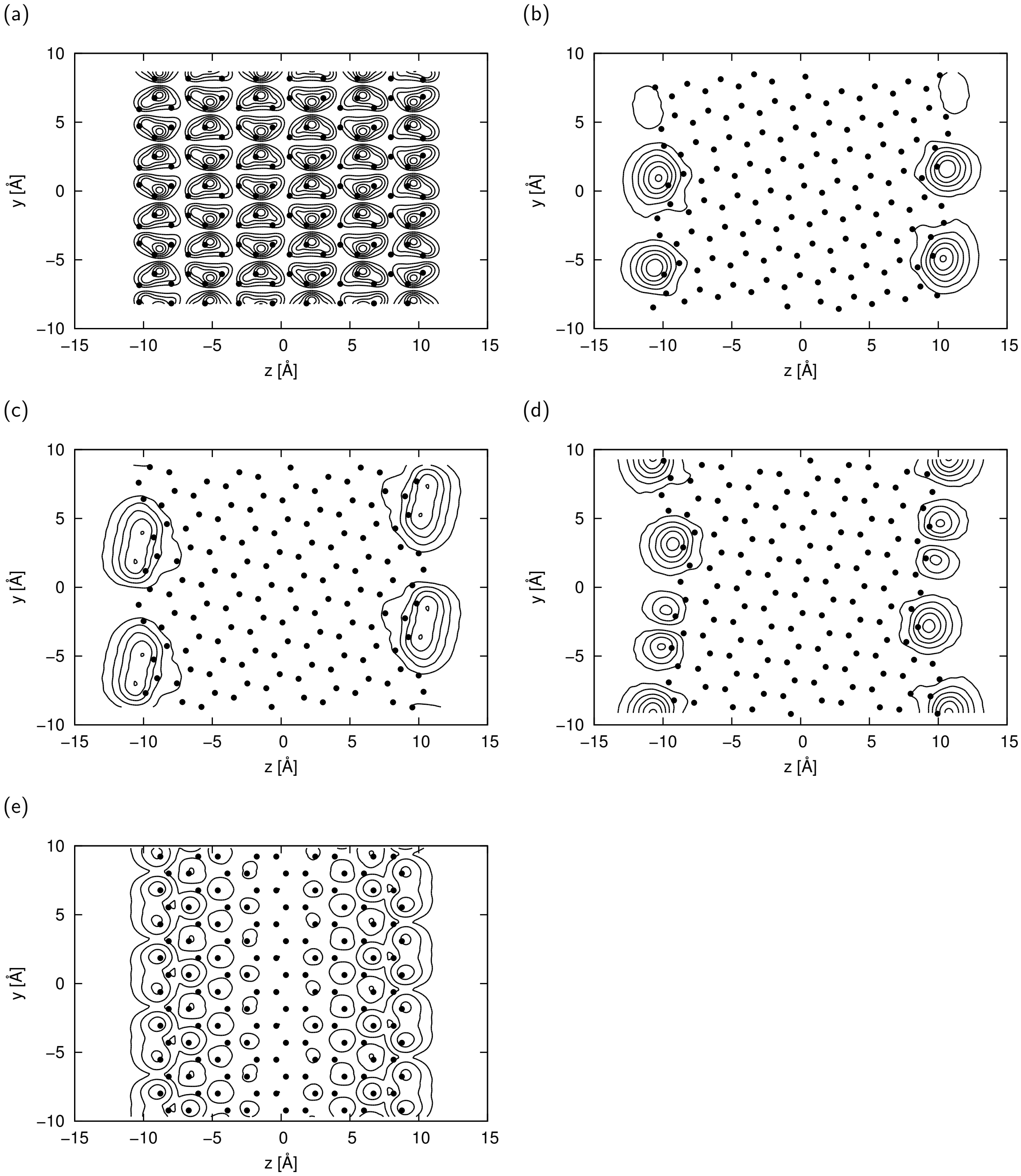

Figure3.8 Contour plots of wave functions at the Γ point near the E_F of graphene nanoribbons with clean edges. Each figure denote the nanoribbons with (a) armchair edge ($\theta = 0°$), chiral edges (b) $\theta = 8°$, (c) $\theta = 16°$, (d) $\theta = 23°$, and (e) zigzag edge ($\theta = 30°$).

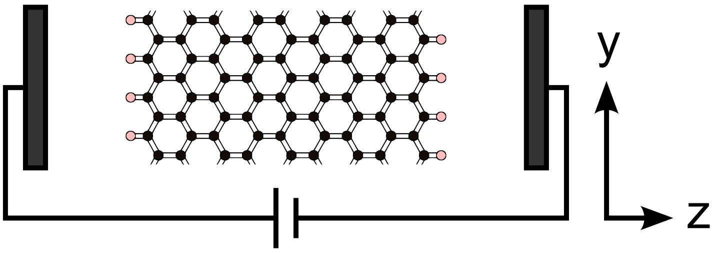

Figure3.9 Structural models of graphene nanoribbons under parallel electric fields. Dark shaded rectangles represent metal electrodes simulated by the effective screening medium method.

shapes. In this case, the dimerization of edge atoms leads to substantial upward and downward shift for states with antibonding and bonding natures, respectively. For nanoribbons with zigzag edges, we can see the hybridized nature of the wave function of edge states and that of dangling bond states because they are almost degenerate.

3.3 Electrostatic Potential under an Electric Field

To simulate the behavior of nanoribbons under a lateral electric field, we used the effective screening medium method to solve the Poisson equation including the external electric field. We applied a parallel electric field between two metal electrodes simulated by the effective screening medium that were situated alongside the rightmost and leftmost atoms of the nanoribbons with 8 Å vacuum regions (see Fig. 3.9). Here, we considered several edge structures between armchair and zigzag to investigate the effect of edge structure on electric field screening. We constructed nanoribbons with five representative edge shapes with indexes of armchair (4,4), (5,3), (6,2), (7,1), and zigzag (9,0) (Fig. 3.1). The width of these nanoribbons was about 20 Å to exclude the size effect from the screening phenomenon. The atomic structures were fully optimized under zero electric field until the force acting on each atom was less than 5 mRy/Å. During calculations under the condition of a finite electric field of 0.25 V/Å, the geometries were fixed to those under the condition of a zero electric field. Force acting on atoms under the electric field is less than about 10^{-4} HR/au. Therefore, the atomic displacement due to the electric field is hardly expected to occur.

Figure 3.10 shows the calculated electrostatic potential at each atomic site of the nanoribbons under an electric field. The electrostatic potential strongly depends on the local atomic arrangement. In the case of armchair edges [the (4,4)-H ribbon], the potential exhibits a stepwise profile along the direction of the electric field, which can be explained by considering the geometric properties of the nanoribbon. The potential is almost constant between the atoms that are connected by short covalent

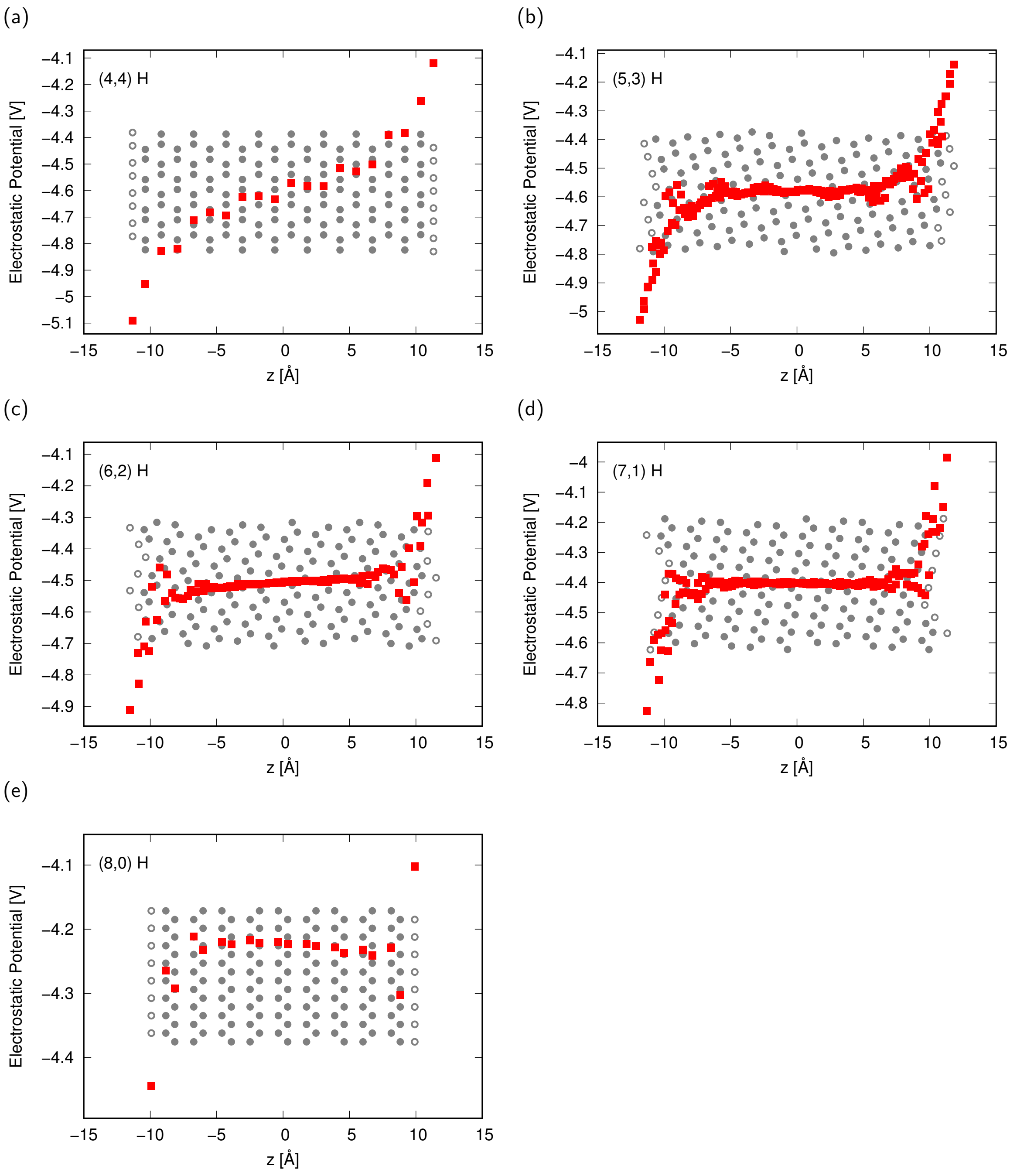

Figure3.10 Electrostatic potential along the direction of electric field at each atomic site of graphene nanoribbons with (a) armchair edge ($\theta = 0°$), chiral edges (b) $\theta = 8°$, (c) $\theta = 16°$, (d) $\theta = 23°$, and (e) zigzag edge ($\theta = 30°$). The squares denote the electrostatic potentials at the atomic sites indicated by the circles.

bonds of less than 1.415 Å. In contrast, a substantial potential gradient is found at the atomic sites associated with long covalent bonds of longer than 1.415 Å. These trends indicate that short C-C bonds lead to strong screening against an external electric field, while long C-C bonds provide weak screening. This behavior can be explained by considering the chemical bonding of the atoms: short bonds possess double-bond character, in which the electron density is higher than that of the long bonds corresponding to single bonds. Therefore, the stepwise potential profile is ascribed to the bond alternation of the nanoribbons, which results from the H-terminated carbon atoms at their edges.

In contrast to the (4,4)-H nanoribbon with armchair edges, the electrostatic potential exhibits anomalous features in other types of nanoribbons. The potential oscillates near the edge atomic site where the potential gradient near the edge atomic sites is opposite to the external electric field. In this region, therefore, the electrons are subjected to potential barriers to transfer through the nanoribbons under the influence of an external field. This fact also indicates that the electrons injected via the electrodes are intrinsically scattered by the oscillating local potential near the edges of the nanoribbons, except for those with armchair edges, under a finite bias voltage between the source and drain electrodes, despite the nanoribbons forming ohmic contacts with the metal electrodes.

The anomalous behavior of the electrostatic potential of the nanoribbons is found to depend on the portion of the edges with zigzag atomic arrangement. In the case of (8,0)-H ribbons with zigzag edges, the potential oscillation is damped rapidly; the oscillation penetrates the second sub-edge atomic site, and the inner part of the ribbon has almost constant potential profile. In sharp contrast, in the cases of other ribbons with general edge shapes (imperfect zigzag edges), the potential oscillation penetrates inside the nanoribbons slightly. We also deduced that the penetration length of the potential oscillation increases with decreasing ratio of zigzag structure. However, in all cases, the modulation is localized around the edge of the nanoribbon. These results imply that the anomalous potential profile is caused by the unique edge-localized states (edge states) of graphene nanoribbons with zigzag edges [3.23–3.25, 3.29]. The edge state is perfectly localized at the edge atomic site, at the zone boundary of the one-dimensional Brillouin zone, while being extended throughout the nanoribbon at two-thirds of the one-dimensional Brillouin zone corresponding to the K point of two-dimensional graphene.

Figure 3.11 shows the wave function distribution at the Γ point of the highest branch of the valence band for the nanoribbons with different edge structures. These states are basically localized at the edge atomic sites except for the armchair edges, indicating the features of the edge state of graphene nanoribbons at the zone boundary.

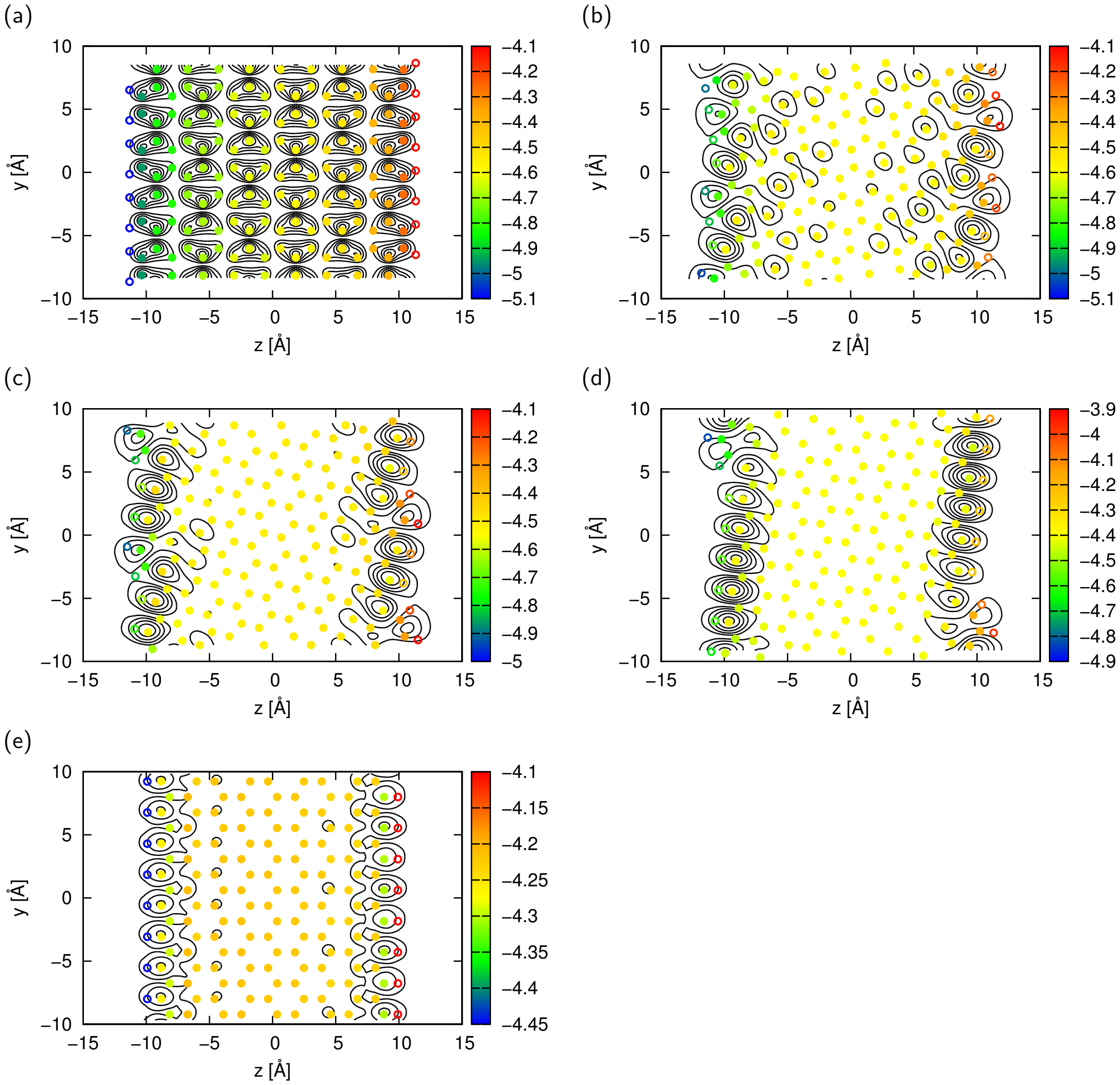

Figure3.11 Electrostatic potential and contour plots of wave functions at the Γ point near the E_F of hydrogenated graphene nanoribbons with (a) armchair edge ($\theta = 0°$), chiral edges (b) $\theta = 8°$, (c) $\theta = 16°$, (d) $\theta = 23°$, and (e) zigzag edge ($\theta = 30°$). Circle colors correspond with the potential depth.

More importantly, the distribution of the edge-localized states of these nanoribbons helps us to uncover the physical mechanisms of over-screening around the edges of the nanoribbons. By focusing on one of two edges, the wave function is only distributed at one of two sublattices in the hexagonal network: substantial distribution is observed at the edge and third sub-edge atomic sites, while the second sub-edge sites are nodal points of the wave function distribution. Because of the absence of wave function distribution at the second sub-edge atomic sites, these sites are not affected by the electric field compared with the edge atomic sites where the wave function shows a substantial distribution. In accordance with the wave function distribution, the over-screening between adjacent atomic sites occurs near the edges of the zigzag nanoribbons.

It is worth investigating the detailed electrostatic potential and electric field in/around the graphene nanoribbons in terms of the edge shapes and edge termination. Figures 3.12 and 3.13 show the contour plots of the electrostatic potential of graphene nanoribbons with hydrogenated and clean edges, together with the corresponding electric field. For ribbons with hydrogenated edges, there is a substantial potential gradient inside the ribbon with armchair edges. As pointed above, the potential gradient is ascribed to the bond alternation arising from the edge C-H bonds. With increasing edge angle, the potential gradient inside the ribbon monotonically decreases. For instance, the sizable potential gradient is absent inside the ribbon with zigzag edges, and the potential drop only occurs at the edge carbon atoms.

The electric field outside the edges strongly depends on the edge shape and termination. In the case of hydrogenated edges, the electric field is strongly concentrated at the protuberant regions of edges where the armchair and zigzag edges coexist. Thus, field emission may occur at protuberances on the hydrogenated graphene nanoribbons [3.42, 3.43]. By removing the hydrogen atoms, we found a different field distribution outside the edges: in contrast to the hydrogenated edges, the field concentrates at the atoms belonging to the zigzag edge close to the protuberant region. In this case, edge reconstruction flattens the atomic sites at the convex region to reduce the energy cost arising from the dangling bonds. Therefore, the zigzag edges are dominant for field emission in graphene nanoribbons with clean edges.

3.4 Electron Injection into Nearly Free Electron States

To investigate the electronic structure of graphene under a parallel electric field, we consider zigzag and armchair graphene nanoribbons with various ribbon widths whose edge atomic sites are fully terminated by hydrogen atoms. This eliminates the dangling bonds at the edge atomic site possessing two-fold coordination, allowing the investigation of the effects of the edge structure and width on the electric field. To simulate the behavior of nanoribbons in a lateral electric field, we adopted effective screening medium method to solve the Poisson equation, including the external electric field. We applied a parallel electric field between two metal electrodes, simulated by effective screening medium, which are situated alongside the rightmost and the leftmost edges of the nanoribbons with 6 Å vacuum regions (Fig. 3.9). In the case,

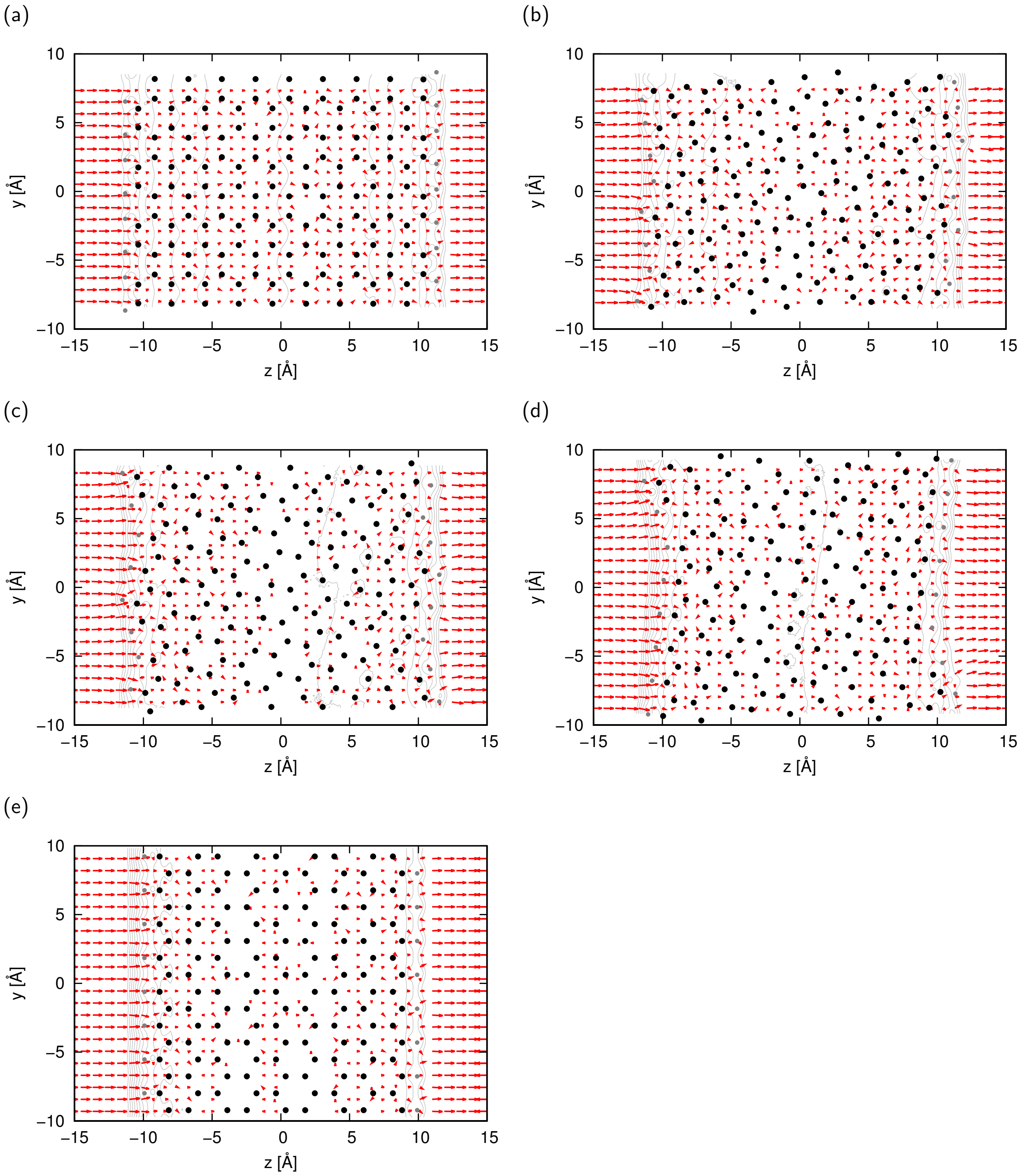

Figure3.12 Contour and vector plots of the electrostatic potential and electric field, respectively, of hydrogenated graphene nanoribbons under an external electric field. Each figure denote the nanoribbons with (a) armchair edge ($\theta = 0^\circ$), chiral edges (b) $\theta = 8^\circ$, (c) $\theta = 16^\circ$, (d) $\theta = 23^\circ$, and (e) zigzag edge ($\theta = 30^\circ$). For both plots, the deep attractive potentials arising from nuclei are subtracted by taking the difference between the potentials with and without the external electric field. Black and gray circles denote carbon and hydrogen atoms, respectively.

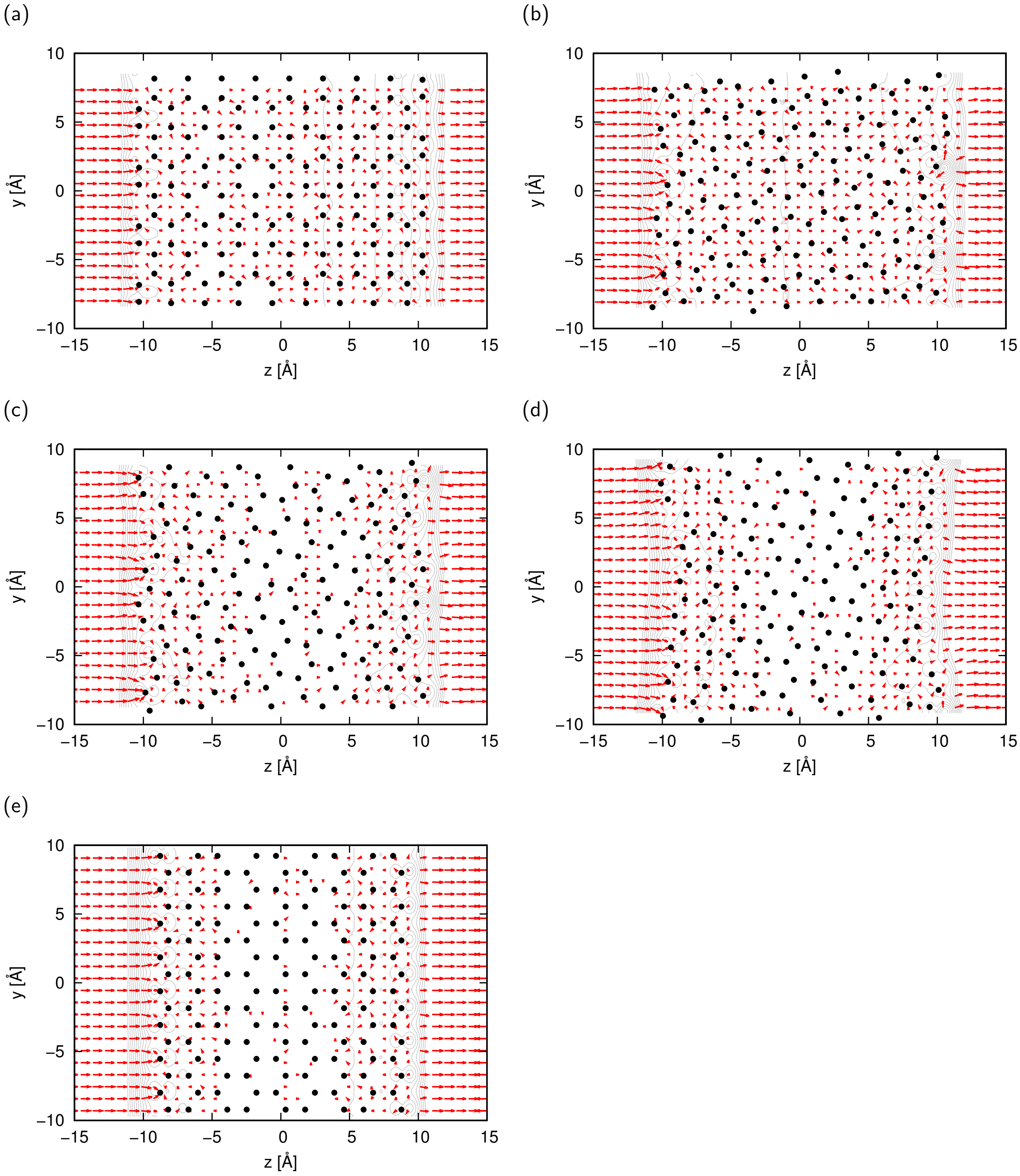

Figure3.13 Contour and vector plots of the electrostatic potential and electric field, respectively, of clean graphene nanoribbons under an external electric field. Each figure denote the nanoribbons with (a) armchair edge ($\theta = 0°$), chiral edges (b) $\theta = 8°$, (c) $\theta = 16°$, (d) $\theta = 23°$, and (e) zigzag edge ($\theta = 30°$). For both plots, the deep attractive potentials arising from nuclei are subtracted by taking the difference between the potentials with and without the external electric field. Black circles denote carbon atoms.

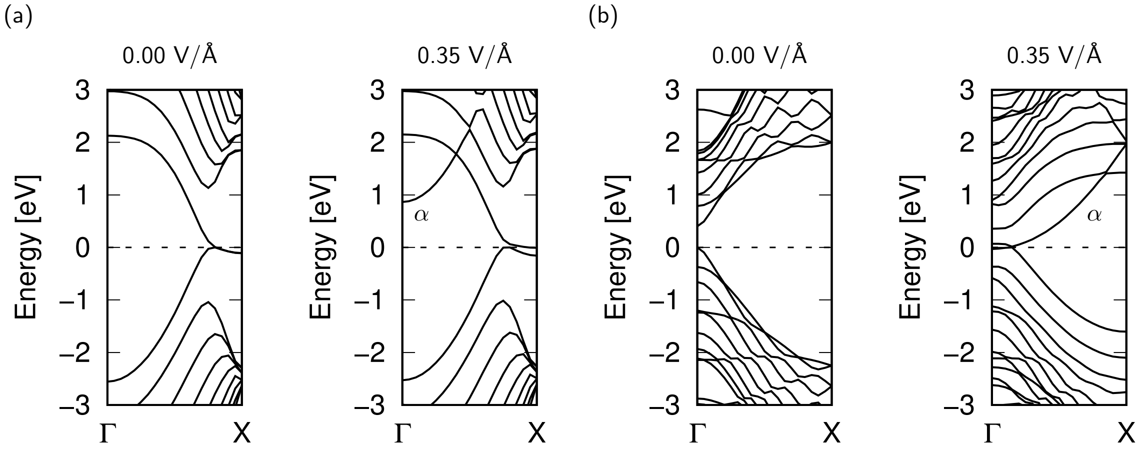

Figure3.14 Electronic energy band of (a) hydrogenated zigzag graphene nanoribbon with 1.8 nm width and (b) hydrogenated armchair graphene ribbon with 2.1 nm width under zero and 0.35 V/Å lateral electric fields. The energies are measured from that of the Fermi level E_F. The label α denotes the NFE state.

the anode and cathode electrodes are set to the leftside ($z = -z_0$) and the rightside ($z = z_0$) of the unit cell as shown in Fig. 3.9. The atomic structures were fully optimized under a zero electric field until the force acting on each atom was less than 5 mRy/Å. Integration over Brillouin zone was carried out using equidistant k-point sampling in which 4 and 6 k-points were taken along a ribbon direction in the armchair and the zigzag edges, respectively. During calculations under the condition of a finite electric field up to 1.0 V/Å, the geometries were fixed to those under the condition of a zero electric field. Force acting on atoms under the electric field is less than about 10^{-4} HR/au. Therefore, the atomic displacement due to the electric field is hardly expected to occur.

Figure 3.14 shows the electronic energy band of graphene nanoribbons under lateral electric fields of zero and 0.35 V/Å. In both zigzag and armchair ribbons, a quadric dispersion band emerges near the E_F around the Γ point in the electric field, while such a state is absent in the case of a zero electric field. The quadric dispersion seems to be similar to the case of the nearly free electron (NFE) state of a graphene sheet in a perpendicular electric field, which is distributed both above and below the atomic layer.

To elucidate the physical properties of the quadric dispersion band, we depict the contour plot of the wave function of the state at the Γ point in Fig. 3.15. The maxima of the state are distributed alongside the leftmost edges of the zigzag and armchair ribbons, with 3.6 and 3.4 Å vacuum region, respectively. The state is primarily

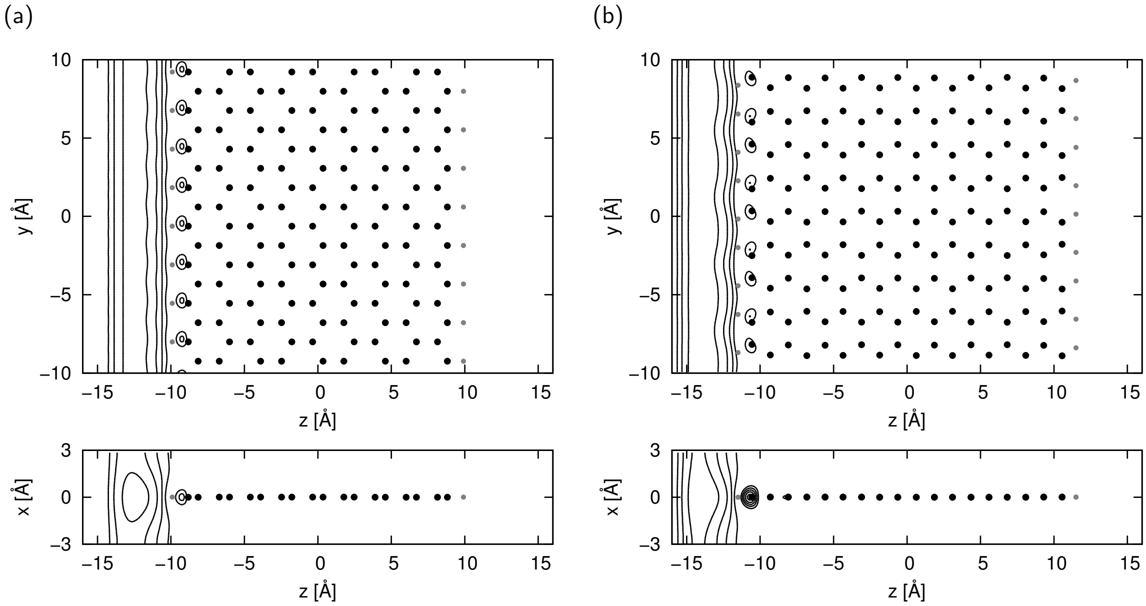

Figure3.15 Top and side views of contour plots of the NFE states of (a) zigzag ribbon and (b) armchair ribbon under the lateral electric field of 0.35 V/Å. Black and gray circles denote atomic positions of carbon and hydrogen, respectively.

distributed at the vacuum region dislodged from the leftmost edge atomic site and is also slightly distributed at the atomic site near the edge atomic site. Furthermore, the state is extended in the direction parallel to the ribbon with almost uniform distribution in the vacuum region. The characteristic distribution of the state as well as the quadric dispersion band allows it to be classified as an NFE state at the edge of the atomic networks.

Next, we investigate how the NFE state of the graphene nanoribbon depends on the lateral electric field. Figure 3.16 shows the eigenvalue of the NFE state with respect to the E_F as a function of the lateral electric field. The NFE state monotonically shifts downward with increasing electric field strength and eventually crosses the E_F. The NFE state is located 3.1 eV above the E_F under a zero electric field and crosses the E_F under electric fields of 0.35 V/Å and 0.46 V/Å for armchair and zigzag nanoribbons, respectively. This downward shift is qualitatively the same as that observed in graphite thin films under the perpendicular electric field. Furthermore, once the state crosses the E_F, the NFE state remains almost constant with increasing electric field strength above the critical values.

It is worth to discuss the physical origin of the remarkable shift of the NFE state. The NFE is the empty state and distributed in the vacuum region where atoms and electrons are absent. Therefore, the NFE state directly feels the potential gradient in the vacuum region due to electric field, resulting in the downward shift of the

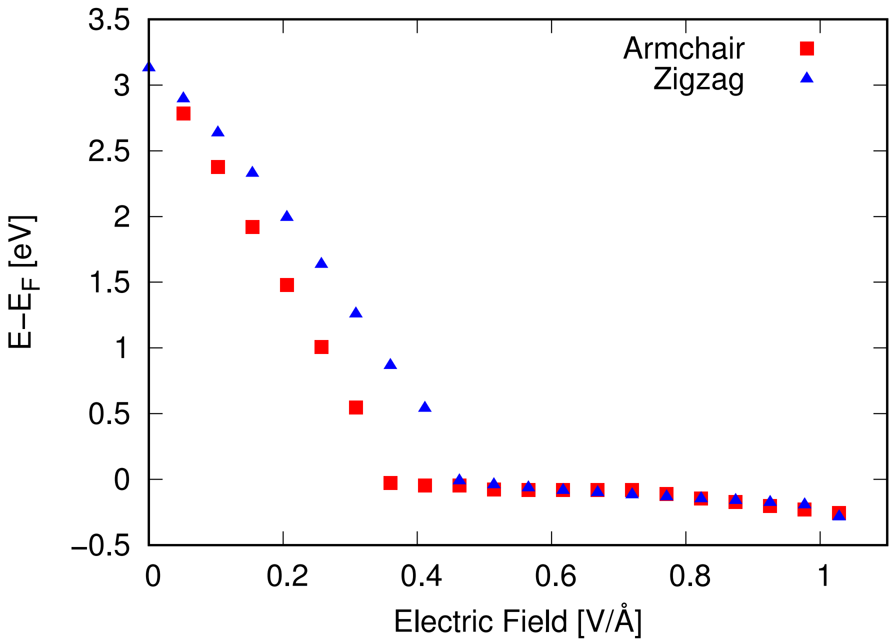

Figure3.16 NFE position of the zigzag ribbon with 1.8 nm width and the armchair ribbon with 2.1 nm as a function of the lateral electric field. The energies are measured from that of the Fermi level E_F. Triangles and squares denote the values for the zigzag and armchair ribbons, respectively.

state. In sharp contrast to the NFE state, the remaining states, π and σ states, are occupied states which are distributed on and in the atomic network, so that the electrons distributed in the atomic networks screen the electric field preventing the downward shift of these state. The mechanism well explain the weak field dependence of the NFE state on the electric field above the critical field: electrons accommodated into the state screen the external field and prevent the further downward shift of the NFE state against the field.

Figure 3.17 shows the plane-averaged electrostatic potential of graphene nanoribbons under the parallel electric field along the z direction. The armchair and zigzag ribbons screen the external electric field, while the potential gradient appears in the vacuum regions. In both ribbons, we find a substantial gradient of the electrostatic potential outside the leftmost edge atomic sites because of the external electric field. The gradient outside the ribbon where the NFE state is distributed and the unoccupied nature of the NFE state leads to a substantial downward shift of the state with respect to the external electric field. It should be noted that the E_F is still located below the bottom of the potential at the left electrode, excluding the physically irrelevant origin of the state caused by the extrinsic spilled electrons at the left electrode.

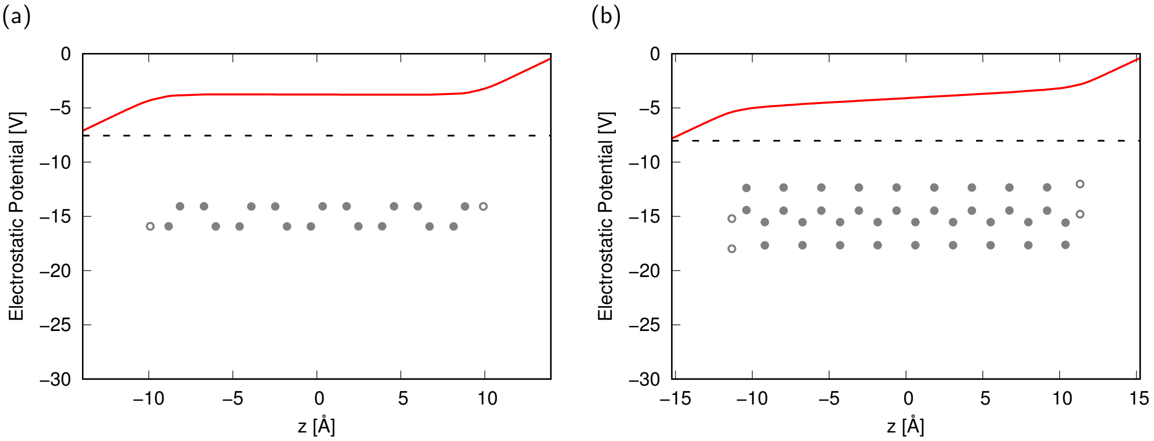

Figure3.17 Plane-averaged electrostatic potential along the z direction of (a) zigzag and (b) armchair ribbons. Dotted horizontal lines denote the Fermi level E_F.

The critical electric field inducing electron injection into the NFE state for the armchair ribbon is slightly different from that for the zigzag ribbon. The widths of these ribbons are slightly different from each other. Therefore, the results indicate that the critical electric field for electron injection is expected to depend on the width of the ribbon. Figure 3.18 shows the critical electric field for electron injection into the NFE state as a function of the width of the graphene nanoribbon. The critical electric field depends on the width of the ribbon and monotonically decreases with increasing ribbon width. Note that the width dependence of the critical field is ascribed to the modulation of the potential gradient in the vacuum region from the initially applied field due to the strong screening at the atomic networks of graphene ribbons.

Finally, we focused on the electronic structure of the armchair ribbon under the electric field in addition to the NFE state. The dispersion relation of the top of the π and the bottom of the π^* state near the Γ point is modulated from that under the zero electric field. Under the lateral electric field, the dispersions of these states are modulated from that under zero electric field. The π and π^* states possess narrower dispersion comparing with that they are in a zero field, resulting in an increase in their effective masses for electrons and holes. The increase in the effective masses is ascribed to the small potential gradient inside the armchair nanoribbon leading to the decrease of the electron transfer between adjacent dimer lows, in which the potential exhibits a stepwise profile normal to the ribbon direction because of the bond alternation as mentioned in Sec. 3.3 [3.48].

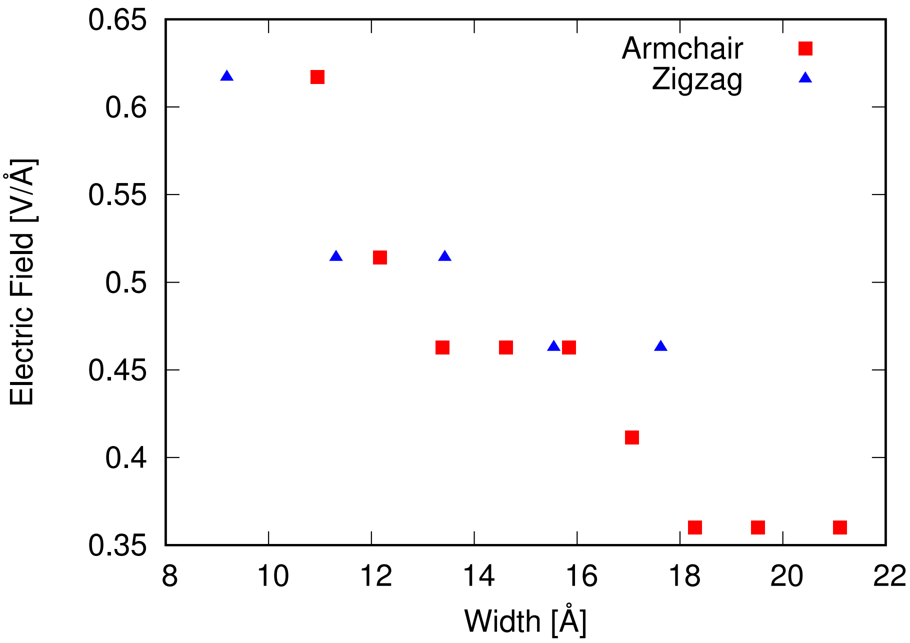

Figure3.18 Critical electric field for electron injection into the NFE state as a function of the width of the graphene ribbons. Triangles and squares denote the values for zigzag and armchair ribbons, respectively.

3.5 Influence of Local Electric Field on Nearly Free Electron States

To investigate the influence of the electric field direction on the NFE states of graphene nanoribbons, we consider zigzag and armchair graphene nanoribbons whose edge atomic sites are fully terminated by hydrogen atoms. We applied an electric field between two parallel metal electrodes, simulated by an effective screening medium, which are situated alongside the rightmost and the leftmost edges of the nanoribbons with $d = 6$ Å vacuum regions (Fig. 3.19). We set the potential barrier with a height of 6.0 eV at 3.5 Å from the rightmost edges of the nanoribbons to prevent the unintentional electron spill under a strong electric field. To investigate the electronic structures of the graphene nanoribbons with respect to the relative direction to the electric field, we rotated the nanoribbons around the ribbon axis with angles between 0° and 90°. The atomic structures of the nanoribbons were fully optimized under a zero electric field until the force acting on each atom was less than 5 mRy/Å. Integration over the Brillouin zone was carried out using equidistant k-point sampling in which 4 and 6 k-points were taken in the ribbon direction for the armchair and

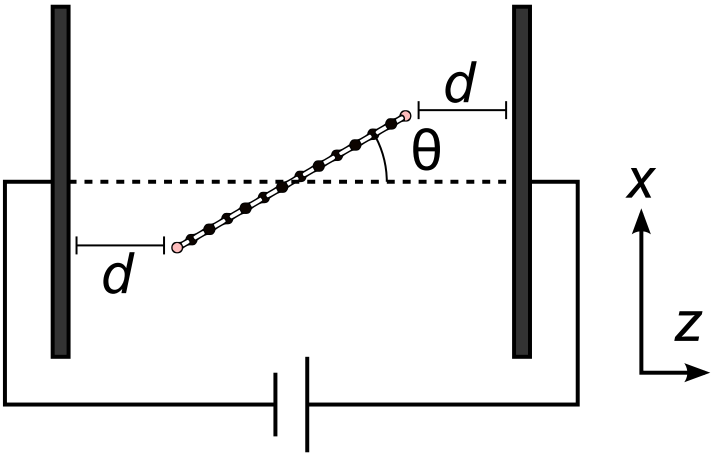

Figure3.19 Structural model of graphene nanoribbons under an electric field. Dark shaded rectangles represent metal electrodes simulated by the effective screening medium method.

the zigzag ribbons, respectively. During the calculations under the condition of a finite electric field up to 0.5 V/Å, the atomic positions were fixed to those under the condition of a zero electric field. Force acting on atoms under the electric field is less than about 10^{-4} HR/au. Therefore, the atomic displacement due to the electric field is hardly expected to occur.

Figure 3.20 shows the electronic energy band of graphene nanoribbons under zero and 0.5 V/Å electric fields. For both zigzag and armchair ribbons, the NFE states shift to lower energies for all rotation angles under the external electric field. The downward shift of the NFE states strongly depends on the rotation angle θ. For $\theta = 0°$, the lowest branch of the NFE states is shifted by 2.84 and 3.44 eV compared with those under zero field for zigzag and armchair ribbons, respectively. In contrast, shifts from the zero-field values are 0.36 and 0.22 eV for zigzag and armchair ribbons, respectively, with the rotation angle of $\theta = 90°$.

Figure 3.21 shows the contour plots of the squared wave function of NFE states above the E_F under a parallel electric field of 0.5 V/Å. For the ribbons with a rotation angle of $\theta = 0°$, the lowest unoccupied (LU) state has NFE nature with the maximum distribution existing outside the graphene edge and also extending along the edge in both the zigzag and armchair ribbons. By focusing on the higher branches of the quadric dispersion bands above the E_F at the Γ point, we found that the LU+2 in the zigzag ribbon and LU+3 in the armchair ribbon exhibit NFE state nature, which is also distributed outside the rightmost atomic sites with a node with respect to the ribbon layer.

The NFE states exhibit a hybrid nature with the π, σ, and other NFE states for the

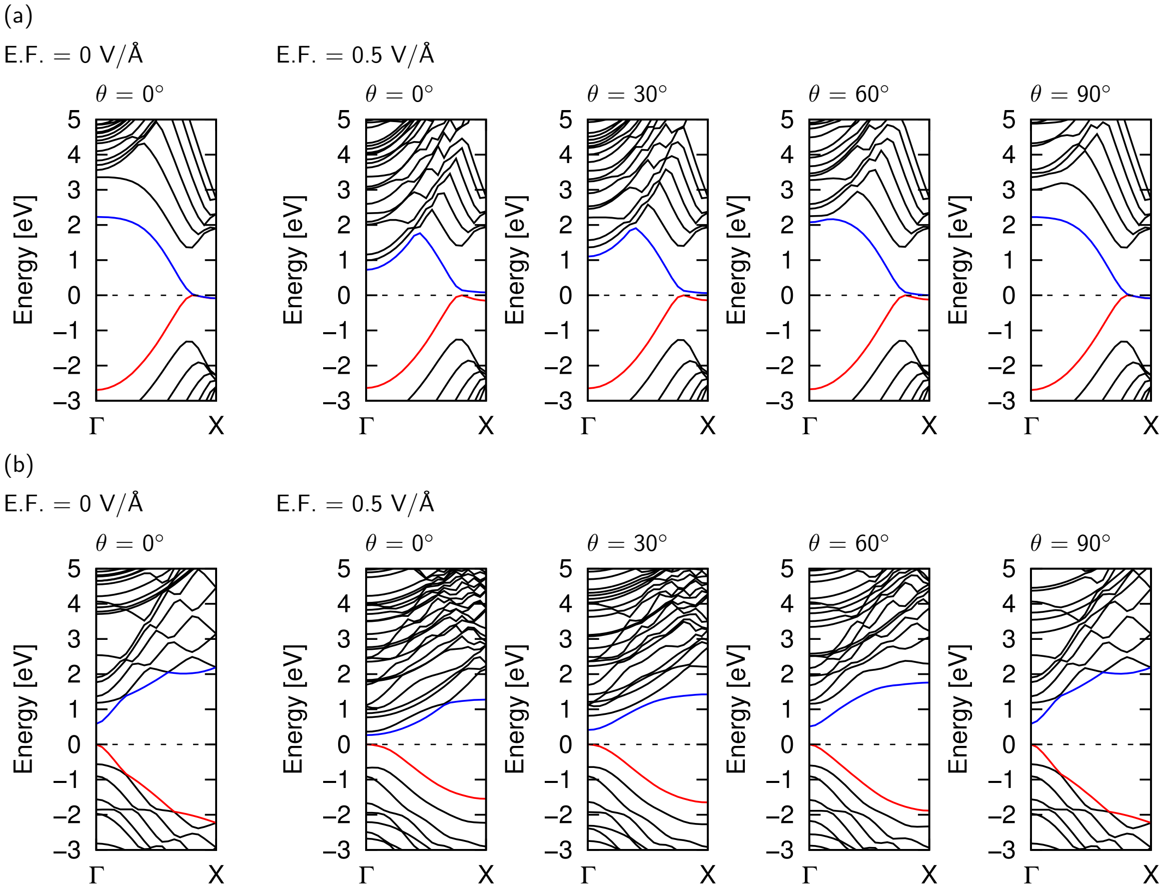

Figure3.20 (Color online) Electronic energy band of (a) zigzag and (b) armchair graphene nanoribbons under zero and 0.5 V/Å electric field. The energies are measured from that of the Fermi level E_F.

rotation angle of 60°. The LU state is mainly distributed in the vacuum region outside the zigzag ribbon along with a small distribution on the π states [Fig. 3.21(a): LU state under θ=60°]. A similar hybrid nature on the localized states of the graphene ribbons is also observed in the LU+3 in the zigzag ribbon and the LU+4 in the armchair ribbon. The LU+3 in the zigzag ribbon has a hybridized nature between the NFE states alongside the edge and above and below the ribbon [Fig. 3.21(a): LU+3 state under θ=60°]. On the other hand, the NFE state is hybridized with σ states in the LU+4 in the armchair ribbon [Fig. 3.21(b): LU+4 state under θ=60°].

For the zigzag ribbons with a rotation angle of $\theta = 90°$, we can observe two different distributions of the NFE states: the lowest branch of the NFE is distributed outside both edges of the ribbon while the next lowest branch of the NFE states is distributed above the ribbon, as observed for the conventional NFE states of bulk graphene. For these NFE states, the external electric field dislodges their distributions to the electrode side. In sharp contrast, in the case of an armchair ribbon with a rotation

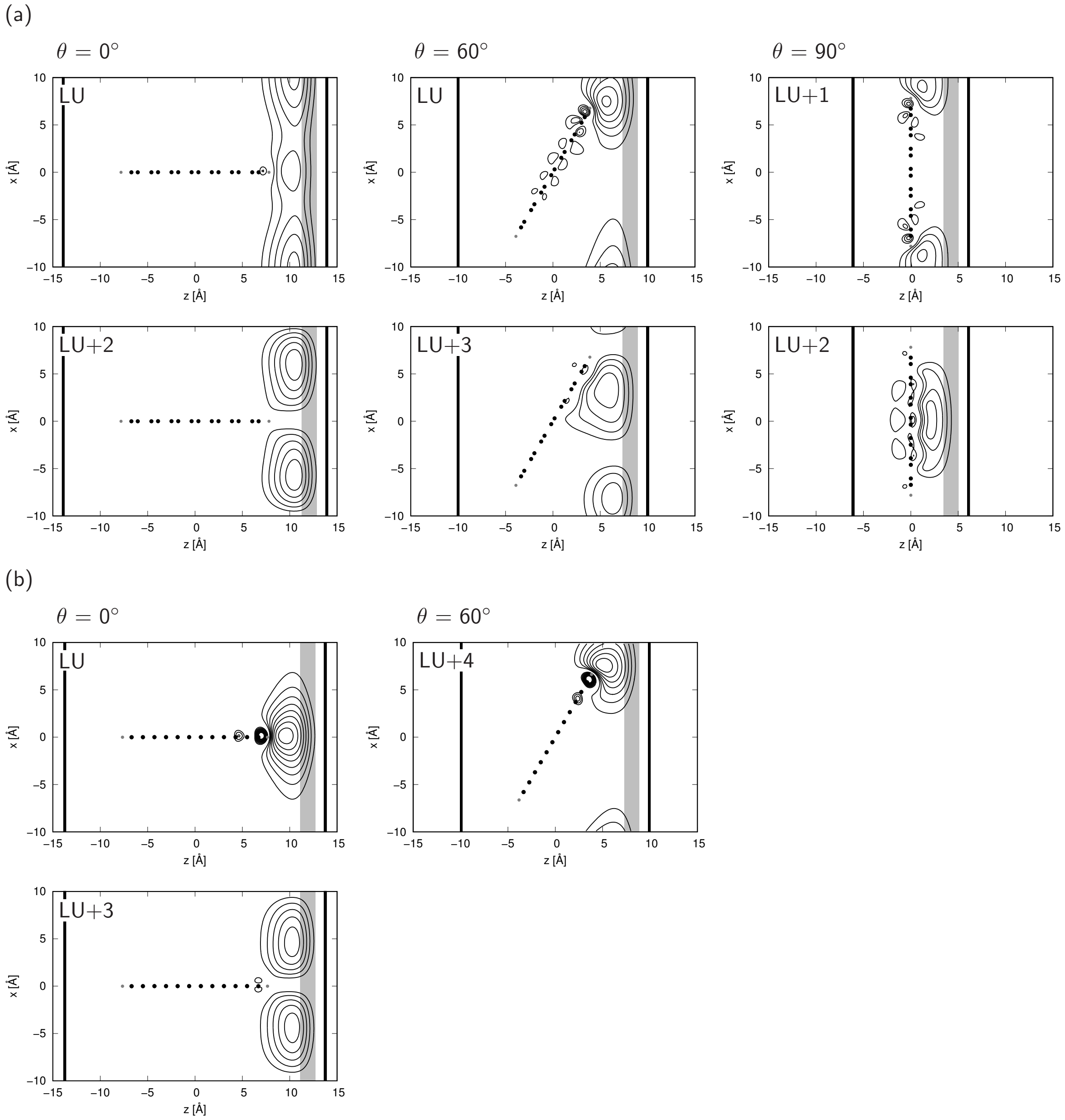

Figure3.21 Side views of contour plots of the NFE states of (a) zigzag and (b) armchair nanoribbons under a 0.5 V/Å electric field. Black and gray circles denote the atomic positions of carbon and hydrogen, respectively. Gray rectangles denote the potential barriers to prevent unintentional electron spill. Thick black lines on the left and right sides of the cell denote the positions of the electrodes.

angle of 90°, no NFE states are observed in the lower conduction bands. These results indicate that the distribution of NFE states strongly depends on the mutual arrangement of the graphene nanoribbons with respect to the electric field.

Next, we investigate how the NFE states of the graphene nanoribbons depend on the

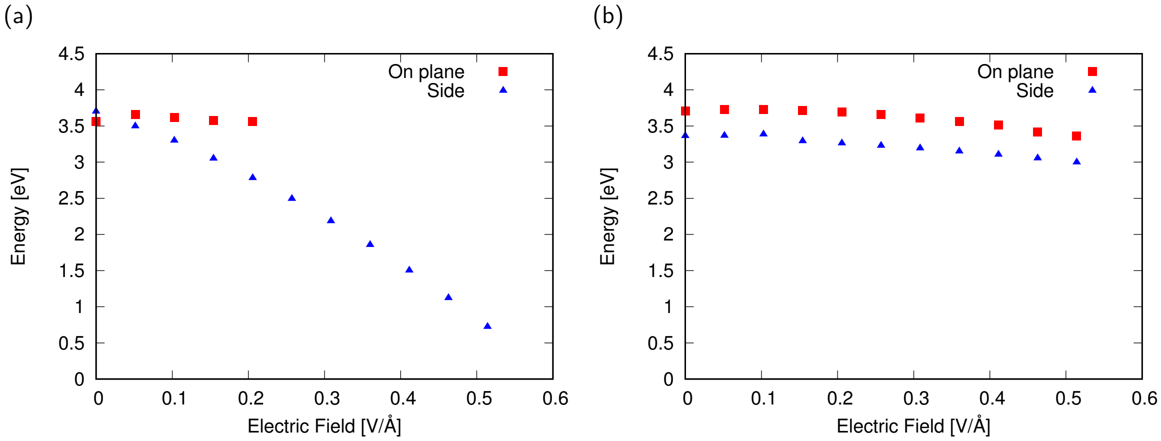

Figure3.22 (Color online) NFE positions for the zigzag ribbon where rotation angles θ are (a) 0° and (b) 90° as a function of the electric field. The energies are measured from that of the Fermi level E_F. Triangles and squares denote the NFE states that are distributed beside and on the plane of the ribbons, respectively.

electric field strength. Figure 3.22 shows the NFE position of the zigzag nanoribbon as a function of the parallel electric field. For the zigzag ribbon with a rotation angle of $\theta = 0°$, the NFE state distributed at the ribbon side rapidly shifts to lower energy with increasing electric field, while the NFE states distributed above the plane gradually shift downward with increasing electric field. For the ribbon with an angle of $\theta = 90°$ or with a perpendicular field, both NFE states weakly depend on the external field. The magnitude of the downward shifts is a tenth smaller than that for the side NFE state under a parallel field. Thus, the NFE state at the ribbon side depends sensitively on the parallel electric field. It should be noted that the NFE states rapidly shift downward by removing the potential barriers at the right side of the cell, because of the increase of the vacuum region that decreases the kinetic energy of the states.

To elucidate the physical origin of the influence of the field direction on the NFE states, we investigated the electrostatic potential on the ribbons as well as the electric field evaluated by taking the gradient of the potential. Figure 3.23 shows the contour and vector plots of the electrostatic potential and the calculated electric field, respectively. For the zigzag ribbons with a rotation angle of $\theta = 0°$, the electric field is highly concentrated around the graphene edge. By increasing θ, the field concentration decreases, and the ribbon finally does not modulate the external field for a rotation angle of $\theta = 90°$. By comparing Fig. 3.22 with Fig. 3.23, we observed that the distribution of the NFE states is qualitatively the same as the regions where an electric field concentration occurs. The electric field concentration causes a substantial electrostatic potential gradient around the edge atomic sites, leading to the downward

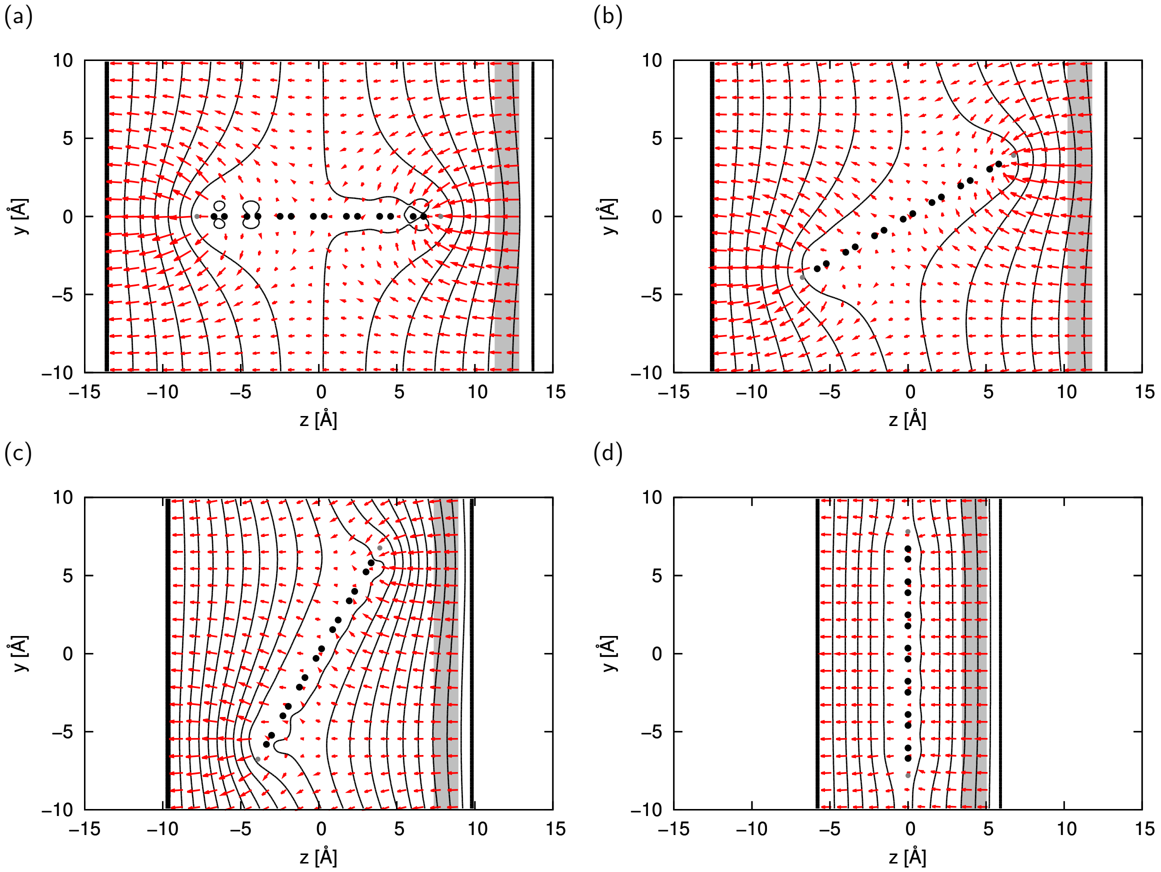

Figure3.23 (Color online) Contour and vector plots of the electrostatic potential and electric field, respectively, of zigzag ribbons with rotation angles θ of (a) 0°, (b) 30°, (c) 60°, and (d) 90° under a 0.5 V/Å electric field. Black and gray circles denote carbon and hydrogen atomic positions, respectively. Gray rectangles denote the potential barriers to prevent unintentional electron spill.

shift of NFE states alongside the edge. Thus, the electric field concentration is the physical origin of the sensitivity of NFE states with respect to the field direction and strength.

Our results indicate that the graphene nanoribbons could provide one-dimensional free electron carriers in the vacuum space alongside the ribbon under a lateral electric field. Since the NFE carriers are free from scatterers, such as atomic vacancies and adatoms on the atomic network, the carriers are expected to possess moderate mobility with remarkable stability. Furthermore, the emergence of the NFE states near the E_F under the electric field also provide a theoretical insight into the field emission images from the edge of the graphene nanoribbons.

3.6 Conclusion

In this chapter, we studied the geometric and electronic structures of graphene nanoribbons with edge angles from armchair to zigzag using density functional theory. Our calculations showed that the edge stability and electronic structure of graphene nanoribbons strongly depends on the detailed edge structures. The edge formation energy retains a constant value around the armchair edges, while it monotonically increases with increasing a portion of zigzag shapes. This fact indicates that graphene nanoribbons and nanoflakes inherently possess edge roughnesses within the angle deviation of $\pm 16^\circ$ around the armchair edges. Furthermore, the edge stability strongly correlates with the electronic structures of graphene nanoribbons: ribbons with near-armchair edges are semiconductors with a finite energy gap, while ribbons with near-zigzag edges are metals in which the DOS at the E_F monotonically increases with increasing a portion of zigzag edges. By analyzing the wave functions near the E_F, we found that the edge state soon appeared around the E_F, even though the nanoribbons do not have perfect zigzag edges. Based on these facts, we conclude that edge states induced by the zigzag portion of the graphene edges crucially determine the stability of the edge structure of nanoribbons and nanoflakes of graphene. For ribbons with clean edges, because the dangling bond states appeared near the E_F, the edge formation energy monotonically increases with increasing a portion of zigzag edges.

We also studied the electronic properties of graphene nanoribbons with several edge structures under a parallel electric field using density functional theory with the effective screening medium method. Our calculations showed that the edge atomic sites of the nanoribbons with zigzag edges anomalously screen an electric field. In these nanoribbons, the electrostatic potential oscillates rapidly, leading to over-screening in the vicinity of edge carbon atomic sites. The penetration depth of the anomalous screening also depends on the edge structure of nanoribbons. The anomalous screening occurs at the edge and second sub-edge atomic sites of perfect zigzag edges, and around edge atomic sites with a depth of up to a few angstroms depending on the portion of zigzag-shaped edge in a nanoribbon. Our detailed analysis indicated that anomalous screening arises from the edge state that is inherent in zigzag edges of sp^2 carbon materials. Conversely, in the case of the nanoribbon with perfect armchair edges, the potential exhibits a stepwise profile reflecting the bond alternation arising from the C-H bonds situated at the edge atomic sites. We also investigate the electric field profile around the edge atomic sites. In the case of edge termination by hydrogen atoms, the electric field is concentrated at the protuberant region corresponding with the boundary of zigzag and armchair edges. In sharp contrast, the field is concentrated at the edge atomic sites with zigzag shapes for clean edges. These facts give theoretical insights in the practical application of graphene edges for field emission devices.

In the analysis of the electronic structure of graphene under the electric field, we also found that the NFE state appears not only in the vacuum region above the atomic layer of graphene, but also in the vacuum region outside the leftmost or rightmost atomic sites. Furthermore, the NFE state substantially shifts downward with the application of a lateral electric field, and it eventually crosses the E_F, at which the nearly free electron carriers are injected outside the graphene nanoribbons. We also demonstrated that the critical electric field for injecting electrons into the NFE state strongly depends on the width of the graphene nanoribbon. The present findings indicate the possibility of an unusual one-dimensional electron system outside and along the edge atomic site of graphene in a lateral electric field. Furthermore, the accumulated electrons may decrease the contact resistance between graphene and metal electrodes.

To further investigate the NFE states of graphene, we study the electronic structure under an electric field in terms of the field direction and strength. We found that the NFE states strongly depend on the mutual arrangements of graphene nanoribbons with respect to the electric field. The NFE states distributed outside the edge depend sensitively on the lateral electric field, while the states weakly depend on the normal electric field. In contrast, the NFE states above and below the ribbons weakly depend on the electric field irrespective of the field directions. Detailed analysis on the electrostatic potential of the graphene ribbons under an electric field clarified that the physical origin of the field direction dependence is the electric field concentration around the ribbon edges as in classical electrodynamics. The field concentration around the edges enhances the gradient of electrostatic potential around the edge atomic sites, leading to a substantial downward shift of NFE states with an increasing electric field.

References

[1] M. S. Dresselhaus and G. Dresselhaus, *Adv. Phys.* **30** 139 (1981).

[2] A.H. Castro Neto, F. Guinea, N.M.R. Peres, K.S. Novoselov, and A.K. Geim, *Rev. Mod. Phys.* **81**, 109 (2009).

[3] Th. Seyller, K.V. Emtsev, K. Gao, F. Speck, L. Ley, A. Tadich, L. Broekman, J.D. Riley, R.C.G. Leckey, O. Rader, A. Varykhalov, and A.M. Shikin, *Surf. Sci.* **600**, 3906 (2006).

[4] K.S. Novoselov, A.K. Geim, S.V. Morozov, D. Jiang, M.I. Katsnelson, I.V. Grigorieva, S.V. Dubonos, and A.A. Firsov, *Nature* **438**, 197 (2005).

[5] Y. Zhang, Y.-W. Tan, H.L. Stormer, and P. Kim, *Nature* **438**, 201 (2005).

[6] X. Du, I. Skachko, F. Duerr, A. Luican, and E. Y. Andrei, *Nature* **462**, 192 (2009).

[7] K.I. Bolotin, F. Ghahari, M.D. Shulman, H.L. Stormer, and P. Kim, *Nature* **462**, 196 (2009).

[8] S. Okada, *Jpn. J. Appl. Phys.* **49**, 020204 (2010).

[9] N.T. Cuong, M. Otani, and S. Okada, *Phys. Rev. Lett.* **106**, 106801 (2011).

[10] K. Kamiya, N. Umezawa, and S. Okada, *Phys. Rev. B* **83**, 153413 (2011).

[11] Y. Takagi and S. Okada, *Jpn. J. Appl. Phys.* **51**, 085102 (2012).

[12] Y. Takagi and S. Okada, *Jpn. J. Appl. Phys.* **51**, 100203 (2012).

[13] M. Koshino and T. Ando, *Phys. Rev. B* **76**, 085425 (2007).

[14] M. Koshino and T. Ando, *Phys. Rev. B* **77**, 115315 (2008).

[15] M. Otani, M. Koshino, Y. Takagi, and S. Okada, *Phys. Rev. B* **81**, 161403(R) (2010).

[16] M. Otani, M. Koshino, Y. Takagi, and S. Okada, *Appl. Phys. Lett.* **96**, 242504 (2010).

[17] E. McCann, *Phys Rev. B* **74**, 161403 (2006).

[18] E.V. Castro, K.S. Novoselov, S.V. Morozov, N.M.R. Peres, J.M.B. Lopes dos Santos, J. Nilsson, F. Guinea, A.K. Geim, and A.H. Castro Neto, *Phys. Rev. Lett.* **99**, 216802 (2007).

[19] J.B. Oostinga, H.B. Heersche, L. Liu, A.F. Morpurgo, and L.M.K. Vandersypen, *Nature Mater.* **7**, 151 (2008).

[20] H. Miyazaki, K. Tsukagoshi, A. Kanda, M. Otani, and S. Okada, *Nano Lett.* **10**, 3888 (2010).

[21] M. Otani and S. Okada, *J. Phys. Soc. Jpn.* **79**, 073701 (2010).

[22] S. Konabe and S. Okada, *J. Phys. Soc. Jpn.* **81**, 113702 (2012).

[23] M. Fujita, K. Wakabayashi, K. Nakada, and K. Kusakabe, *J. Phys. Soc. Jpn.* **65**, 1920 (1996).

[24] K. Nakada, M. Fujita, G. Dresselhaus, and M.S. Dresselhaus, *Phys. Rev. B* **54**, 17954 (1996).

[25] Y. Miyamoto, K. Nakada, and M. Fujita, *Phys. Rev. B* **59**, 9858 (1999).

[26] Y. Kobayashi, K. Fukui, and T. Enoki, *Phys. Rev. B* **73**, 125415 (2006).

[27] A. Hashimoto, K. Suenaga, A. Gloter, K. Urita, and S. Iijima, *Nature* **430**, 870 (2004).

[28] Y. Ma, P.O. Lehtinen, A.S. Foster, and R.M. Nieminen, *New J. Phys.* **6**, 68 (2004).

[29] S. Okada and A. Oshiyama, *Phys. Rev. Lett.* **87**, 146803 (2001).

[30] K. Kusakabe and M. Maruyama, *Phys. Rev. B* **67**, 092406 (2003).

[31] Y. Shimomura, Y. Takane, and K. Watanabe, *J. Phys. Soc. Jpn.* **80**, 054710 (2011).

[32] N.T. Cuong, M. Otani, and S. Okada, *Phys. Rev. B* **87**, 045424 (2013).

[33] V. Barone, O. Hod, and G.E. Scuseria, *Nano Lett.* **6**, 2748-54 (2006).

[34] S. Okada, *Phys. Rev. B* **77**, 041408 (2008).

[35] B. Huang, M. Liu, N. Su, J. Wu, W. Duan, B.L. Gu, and F. Liu, *Phys. Rev. Lett.* **102**, 166404 (2009).

[36] P. Koskinen, S. Malola, H. Häkkinen, *Phys. Rev. Lett.* **101**, 115502 (2008).

[37] C.K. Gan and D.J. Srolovitz, *Phys. Rev. B* **81**, 125445 (2010).

[38] S. Suda and A. Oshiyama, *J. Phys. Soc. Jpn.* **84**, 024704 (2015).

[39] Y.-W. Son, M. L. Cohen, and S. G. Louie, *Nature* **444**, 347 (2006).

[40] S. Dutta, A. K. Manna, and S. K. Pati, *Phys. Rev. Lett.* **102**, 096601 (2009).

[41] T. Kawai, Y. Miyamoto, O. Sugino, and Y. Koga, *Phys. Rev. B* **62**, R16349 (2000).

[42] K. Tada and K. Watanabe, *Phys. Rev. Lett.* **88**, 127601 (2002).

[43] M. Araidai, Y. Nakamura, and K. Watanabe, *Phys. Rev. B* **70**, 245410 (2004).

[44] J.-H. Chen, C. Jang, S. Xiao, M. Ishigamim and M. S. Fuhrer, *Nat. Nanotechnol.* **3**, 206 (2008).

[45] A. Yamanaka and S. Okada, *Appl. Phys. Express* **5**, 095101 (2012).

[46] A. Yamanaka and S. Okada, *Appl. Phys. Express* **6**, 045101 (2013).

[47] A. Yamanaka and S. Okada, *Jpn. J. Appl. Phys.* **52**, 06GD04 (2013).

[48] A. Yamanaka and S. Okada, *Phys. Status Solidi C* **10**, 1624 (2013).

Chapter 4

Geometric and Electronic Properties of h-BN

4.1 Introduction

Hexagonal boron nitride (h-BN) is known to be a prototypical layered material in which each layer is composed of B and N atoms arranged in a hexagonal network like the C atoms of graphite [4.1–4.3]. Along the direction normal to each layer, in sharp contrast to graphite, each layer is weakly bound in an AA' arrangement, in which N atoms are situated just above/below B atoms in adjacent layers, and *vice versa*, due to the interlayer Coulomb interaction between B and N atoms [4.4]. The chemical difference between B and N atoms makes h-BN an insulator with a large energy gap of 5 eV between the valence-band top (VBT) and conduction-band bottom (CBB) at a K point localized on N and B atoms, respectively [4.5, 4.6]. Due to its atomically flat network, h-BN has been used as the supporting substrates for graphene devices that exhibit remarkable carrier mobility [4.7–4.10]. On the other hand, h-BN itself is attracting attention because of its structural similarity to graphene [4.11–4.14]. By the analogy with the graphene, h-BN can form various derivatives being applicable to wide-ranging areas of modern technology: nanoscale tubes and flakes of h-BN have been synthesized by rolling or cutting h-BN sheets with appropriate boundary conditions [4.15–4.25]. For many of the applications of nanoscale h-BN derivatives, it is critical to precisely control their geometric and electronic structures. In particular, the energetics of the nanoflakes yield fundamental insights into the practical procedures to control the structures of nanoscale h-BN derivatives.

Ribbons with nanometer width are a relevant structural model to investigate the energetics and electronic structures of h-BN nanoflakes. Several studies have demonstrated the stability and electronic structures of h-BN nanoribbons with armchair and zigzag edges [4.26–4.31]. However, the stability and electronic structure of h-BN with chiral edges are still unknown because these h-BN nanoflakes may possess edges with arbitrary shapes. In the case of graphene nanoribbons, energetics and electronic structure strongly correlate with their detailed edge structure and edge termination as mentioned in Sec. 3.2. Because of the structural similarity between h-BN and graphene, an analogous correlation between the edge geometries and physical properties of h-BN nanoribbons with arbitrary edge shapes to that of graphene is expected. In addition, the edges in such planar h-BN nanostructures possess an intrinsic polarity, except for perfect armchair edge, because of the nonstoichiometric appearance of B and N atoms at the edges. Polarity at the edges or surfaces of semiconducting and insulating materials can cause unusual geometric and electronic properties, which can be applicable in optoelectronic and piezoelectric devices.

In this chapter, we show the correlation between the edge shape and physical properties of hydrogenated and clean h-BN nanoribbons with various edge shapes, including armchair, zigzag, and chiral edges. In addition, we also show the polar properties of h-BN nanoribbons with respect to the edge shape, hydrogenation, and uniaxial strain.

4.2 Energetics and Electronic Structure

We considered several edge structures between armchair and zigzag of h-BN to investigate their energetics and electronic structures. To simulate h-BN edges with various edge shapes, we considered nanoribbons with hydrogenated and clean edges with edge angles of 0 (armchair), 5, 8, 14, 16, 22, 23, and 30° (zigzag) (Figs. 4.1 and 4.2). To allow quantitative discussion of the energetics of the nanoribbons with various edge shapes, the ribbons possessed similar widths and unit lengths of about 1.8–2.2 and 1.5–2.0 nm, respectively. The geometric structures of h-BN nanoribbons were optimized until the force acting on atoms was less than 0.005 Ry/Å under the fixed lattice parameter along the ribbons, which was determined by the bulk bond length of 1.45 Å.

The effective screening medium (ESM) method was adopted to avoid unphysical dipole interactions with the periodic images arising from their polar edges in the framework of the conventional DFT calculations. This is because h-BN nanoribbons with arbitrary edge shapes intrinsically possess lateral polarization arising from the chemical difference between B and N atoms. In this case, to simulate the open boundary condition in lateral inter-ribbon directions, we put ESM with a relative permittivity of 1, which simulates vacuum conditions in this region ($\varepsilon_0 = 8.854 \times 10^{-12}$ Fm^{-1}), at the cell boundaries with vacuum spacing of 8 Å to the rightmost and leftmost atoms of the nanoribbons (Fig. 4.3).

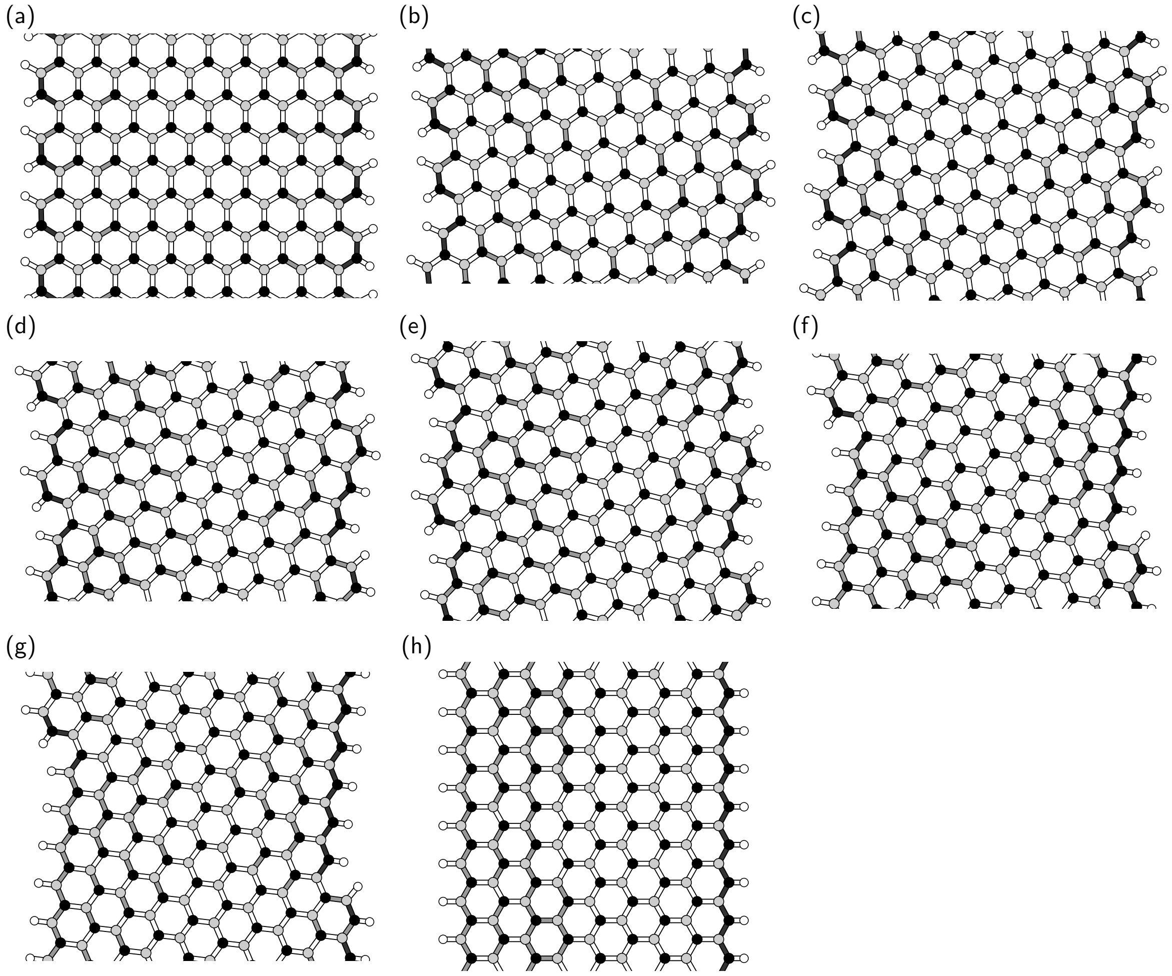

Figure4.1 Optimized geometries of h-BN nanoribbons with (a) an armchair edge ($\theta = 0°$), chiral edges with (b) $\theta = 5°$, (c) $\theta = 8°$, (d) $\theta = 14°$, (e) $\theta = 16°$, (f) $\theta = 22°$, (g) $\theta = 23°$, and (h) a zigzag edge ($\theta = 30°$). Black, gray, and white circles denote nitrogen, boron, and hydrogen atoms, respectively. Black, gray, and white bonds indicate short (–1.44 Å), medium (1.44–1.45 Å), and long (1.45 Å–) bonds, respectively. White bonds situated at the edge of the nanoribbons correspond to B–H and N–H bonds.

4.2.1 Hydrogenated edges

Figure 4.1 shows the optimized structures of h-BN nanoribbons with various edge angles. In all cases, the bond lengths of the nanoribbons are not equivalent. Bonds associated with hydrogenated N atoms are shorter than the other bonds. The bond lengths around hydrogenated N atoms are 1.44 Å or shorter due to the inward structural reconstruction increasing the π nature of edge N atoms to accommodate excess electrons provided by H atoms. For a ribbon with armchair edges, there is a symmet-

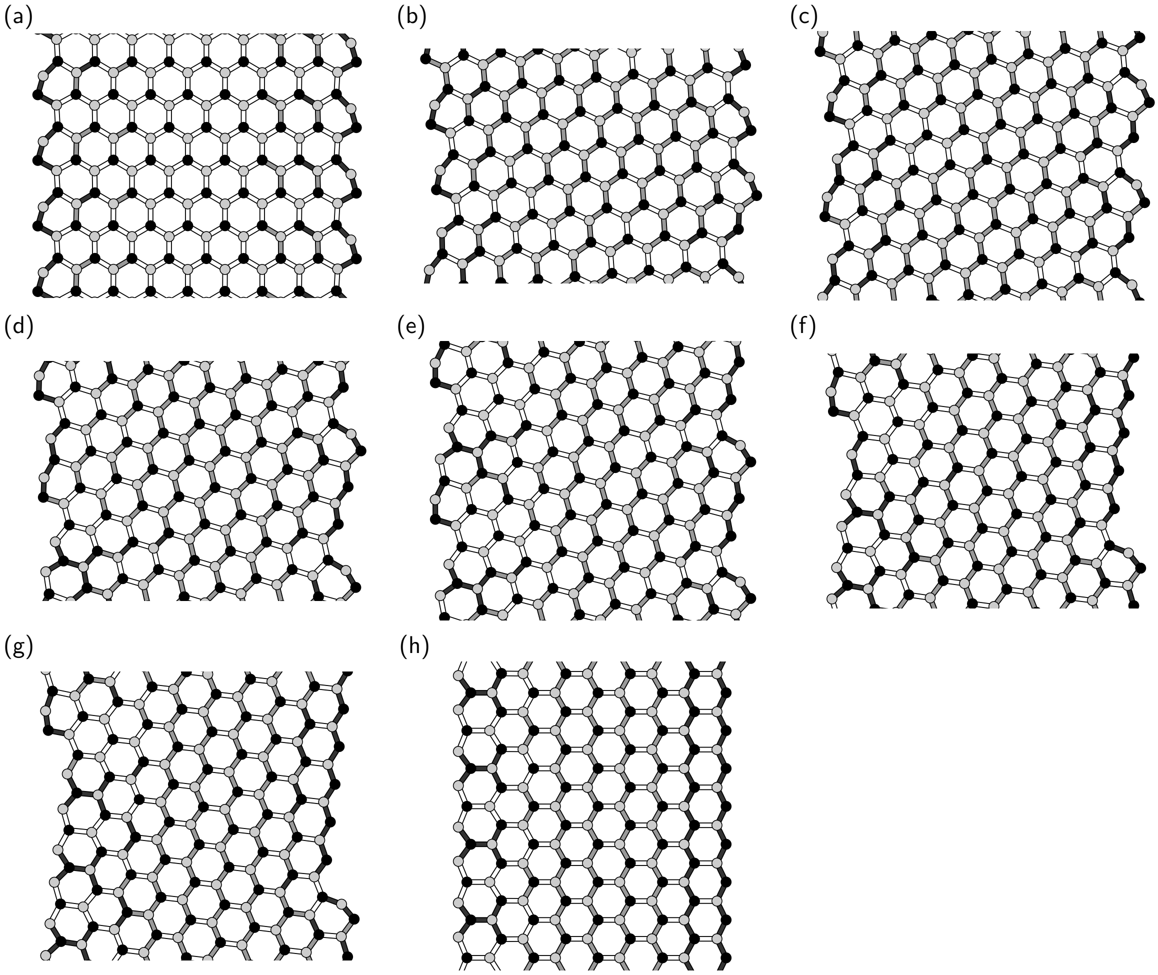

Figure4.2 Optimized geometries of h-BN nanoribbons with (a) an armchair edge ($\theta = 0°$), chiral edges with (b) $\theta = 5°$, (c) $\theta = 8°$, (d) $\theta = 14°$, (e) $\theta = 16°$, (f) $\theta = 22°$, (g) $\theta = 23°$, and (h) a zigzag edge ($\theta = 30°$). Black, gray, and white circles denote nitrogen, boron, and hydrogen atoms, respectively. Black, gray, and white bonds indicate short (–1.44 Å), medium (1.44–1.45 Å), and long (1.45 Å–) bonds, respectively.

ric bond alternation along the ribbon direction. In contrast, for other ribbons, bond alternation is asymmetric because of the asymmetric atomic arrangement at edges. In particular, significant asymmetric structural reconstruction occurs in the ribbons with zigzag edges. In this case, the bond length retains its bulk value near the N edge while substantial bond alternation occurs near the B edge.

Before investigating the energetics of h-BN ribbons with hydrogenated edges with arbitrary edge shapes, we investigated the edge formation energy of h-BN nanoribbons with armchair and zigzag edges with respect to ribbon width, because the edge formation energy of graphene nanoribbons strongly depends on their width [4.32].

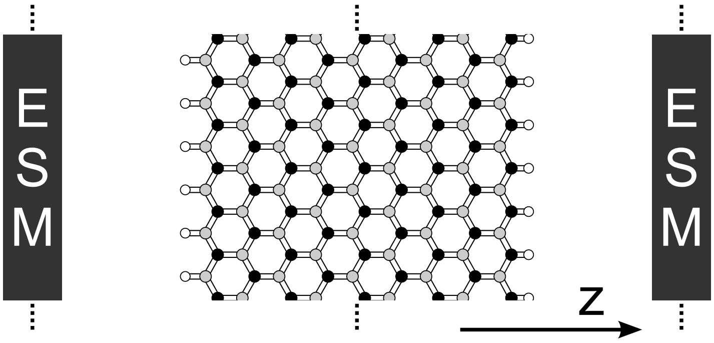

Figure4.3 Structural model of h-BN nanoribbons under the open boundary condition in which the ribbon is sandwiched by two ESM situated at the cell boundaries.

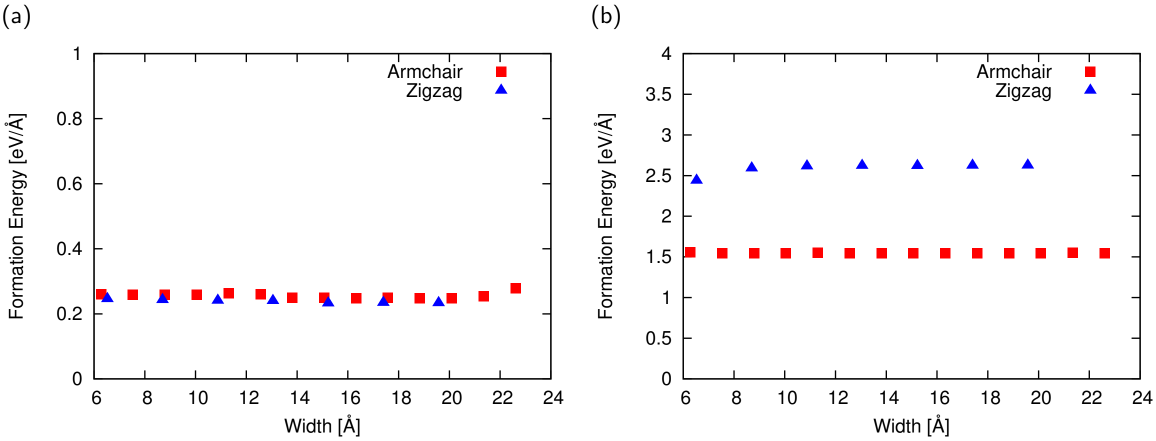

Figure4.4 Edge formation energy of h-BN nanoribbons with (a) hydrogenated and (b) clean edges as a function of ribbon width. Red squares and blue triangles denote the edge formation energy of nanoribbons with armchair and zigzag edges, respectively.

Figure 4.4(a) shows the edge formation energy of hydrogenated h-BN nanoribbons as a function of ribbon width. The edge formation energy E_{edge} was evaluated using the following formula:

$$E_{\mathrm{edge}} = (E_{\mathrm{total}} - N_{\mathrm{BN}}\mu_{\mathrm{BN}} - N_{\mathrm{H}}\mu_{\mathrm{H}})/L_{\mathrm{edge}} \tag{4.1}$$

where E_{total}, N_{BN}, N_{H}, μ_{BN}, μ_{H}, and L_{edge} denote the total energy of ribbons, the number of pairs of B and N atoms, the number of H atoms, the energy potential of h-BN per BN pair, the chemical potential of H atoms, and the edge length of a unit cell, respectively. μ_{H} is evaluated by the total energy per atom of H_2 molecules. As shown in Fig. 4.4(a), edge formation energy of the hydrogenated h-BN nanoribbons is almost constant up to a width of 22 Å for both zigzag and armchair ribbons. Thus, the

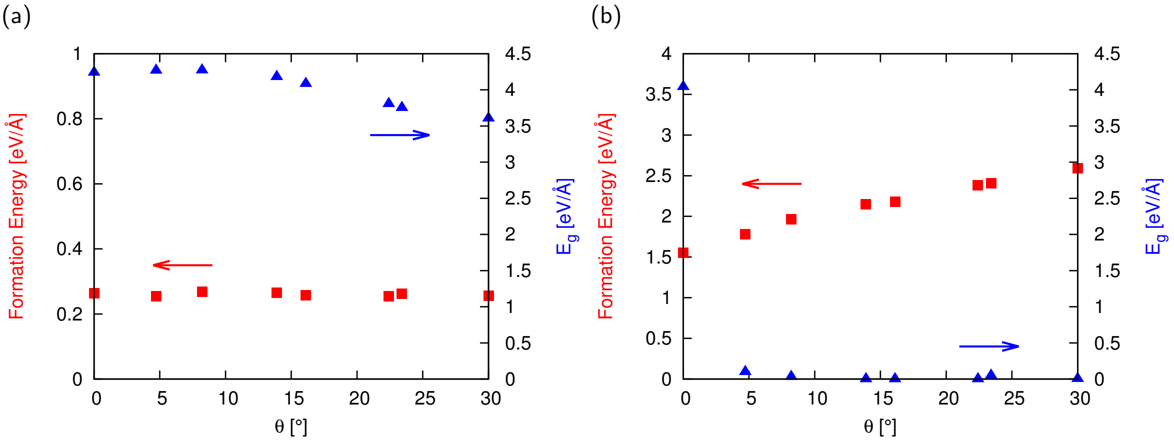

Figure4.5 Edge formation energy and energy gap of h-BN nanoribbons with (a) hydrogenated and (b) clean edges as a function of edge angle θ.

edge formation energy of the H-terminated h-BN nanoribbons is nearly independent of the ribbon width and edge shape. Note that the edge formation energy contains a numerical error of 5 meV, which arises from the total energies of ribbons with different numbers of BN pairs depending on their unit cell size.

Although the edge energy of the hydrogenated h-BN nanoribbon with zigzag edges is almost the same as that with armchair edges, it is worth investigating the detailed edge angle dependence of the edge formation energy. Figure 4.5(a) shows the edge formation energy and the energy gap between VBT and CBB of hydrogenated h-BN nanoribbons as a function of the edge angle. As shown in Fig. 4.5(a), the edge formation energy retains a constant value for all edge angles. Thus, based on the energetics, *i.e.* the constant edge formation energy, h-BN flakes are unlikely to possess preferential edge shape under static conditions. This result implies that the h-BN flakes inherently possess edge roughness. The h-BN nanoribbons are insulators with an energy gap of about 5 eV, irrespective of the edge angle θ. In the case of graphene nanoribbons with hydrogenated edges, the edge formation energy retains constant up to the angle $\theta = 16°$, where the ribbons possess semiconducting electronic structure with a finite energy gap. Thus, the constant edge formation energy of the h-BN nanoribbons is ascribed to their insulating electronic structure.

Figure 4.6 shows the electronic energy bands and density of states (DOS) of hydrogenated h-BN nanoribbons with various edge angles. All ribbons are insulators with an energy gap of about 4 eV. This energy gap is considerably narrower than that of bulk h-BN, indicating that the detailed electronic properties of h-BN ribbons around the gap are different from those of bulk h-BN. As shown in Fig. 4.6, the CBB retains a constant value up to the angle of 8°, and then gradually shifts downward with in-

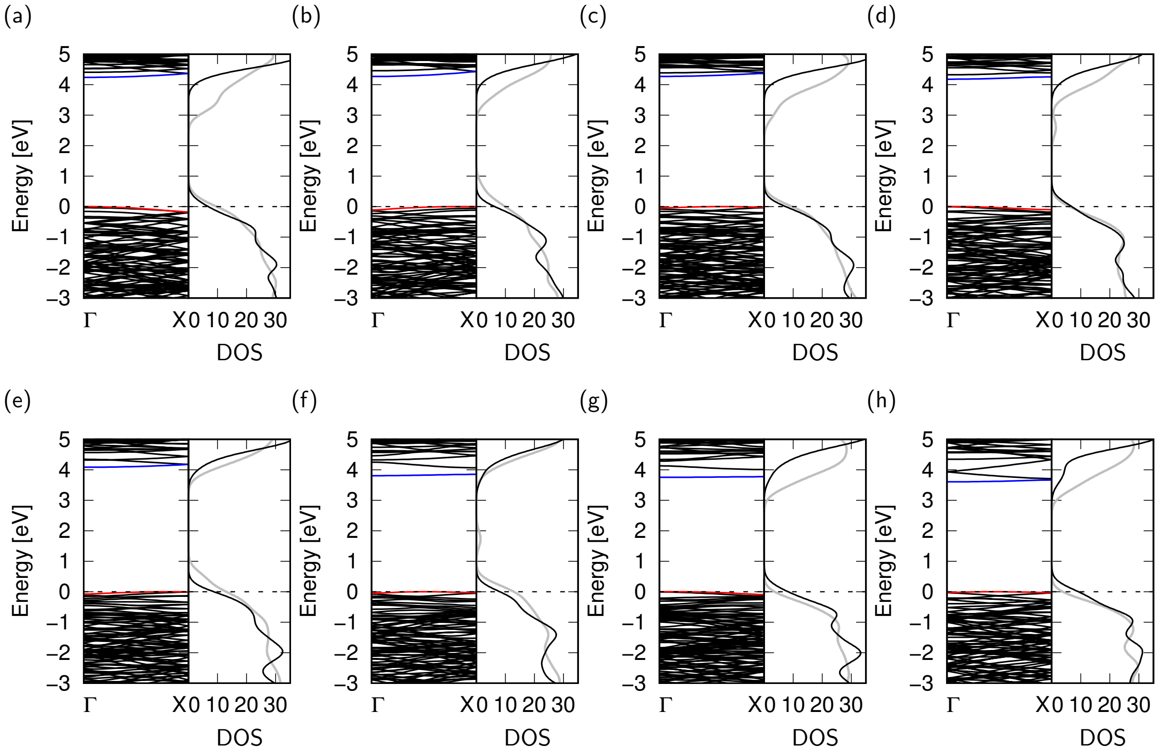

Figure4.6 Electronic structure and density of states (DOS) of hydrogenated h-BN nanoribbons with edge angles θ of (a) 0°, (b) 5°, (c) 8°, (d) 14°, (e) 16°, (f) 22°, (g) 23°, and (h) 30°. Red and blue lines indicate the VBT and CBB states, respectively. Gray lines denote the DOS at the temperature of 1000 K. Energies are measured from the VBT. Unit of DOS is states/eV.

creasing the edge angle θ, resulting in a decrease of the energy gap. The dependence of the electronic structure on edge angle implies that the polarization of h-BN around its edges plays an important role in determining the positions of the lower branches of the conduction band. For the ribbons with $\theta = 14°$ or larger, the lowest branch of the conduction band is separated from the bulk states, leading to an additional structure in the DOS of unoccupied states. It is worth investigating how the electronic structures of h-BN nanoribbons depend on the structural corrugation or rippling formed at elevated temperature. To check the DOS of the ribbons at elevated temperature, we performed *ab initio* molecular dynamics calculations at 1000 K. After a simulation time of 100 fs, all h-BN nanoribbons possess structural corrugation of up to 2 Å. The structural corrugation due to the finite temperature decreases the band gap of the nanoribbons, but does not affect the qualitative shape of the DOS.

To unravel the physical origin of the detailed electronic structure modulation in the lower branches of the conduction band with respect to the edge angle, we investigated the wave function distribution of VBT and CBB states at the Γ point. Figure 4.7

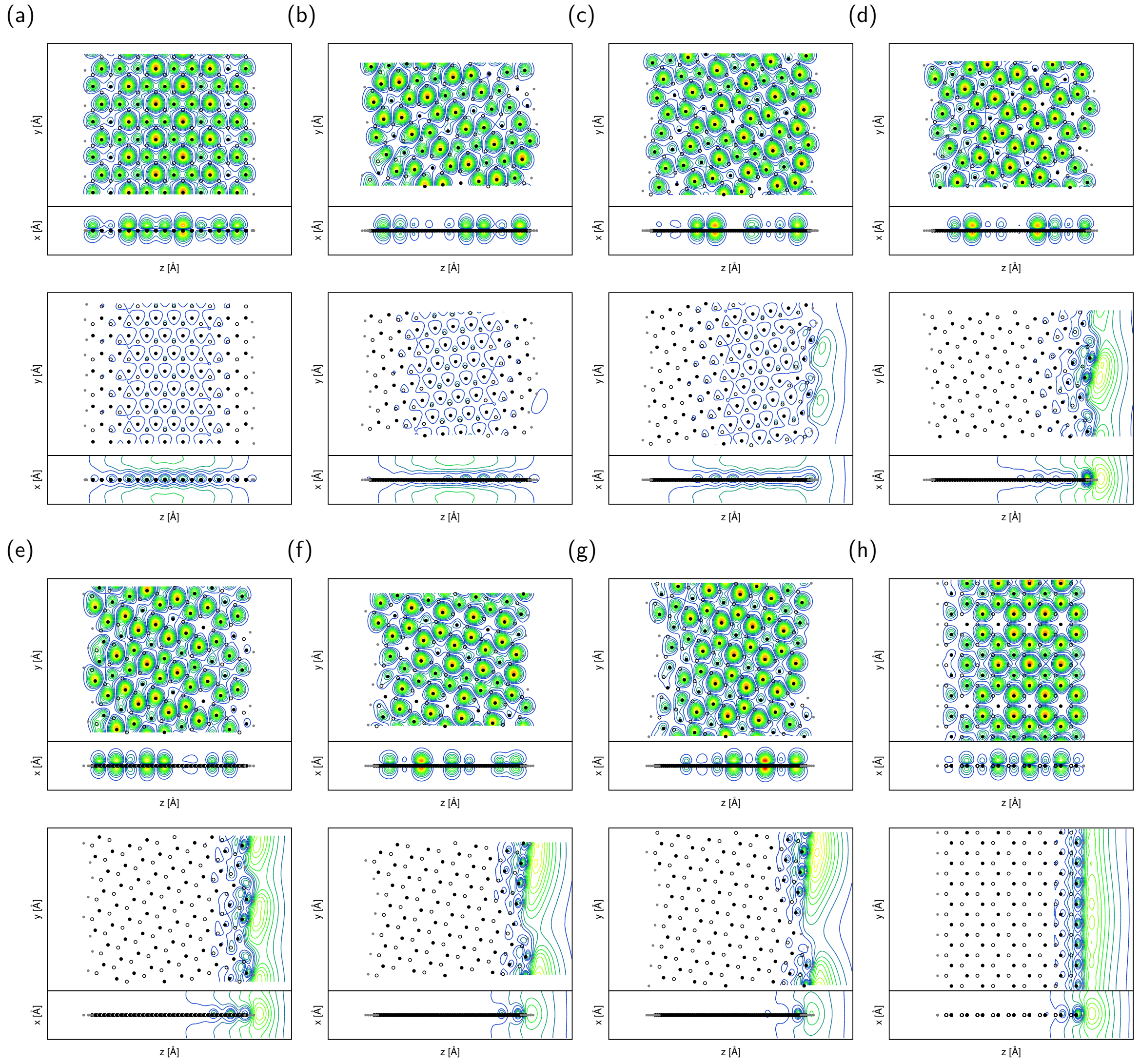

Figure4.7 Top ($x = 0$) and side ($y = 0$) views of contour plots of wave functions at the Γ point near the Fermi level E_F of hydrogenated h-BN nanoribbons with edge angles θ of (a) 0°, (b) 5°, (c) 8°, (d) 14°, (e) 16°, (f) 22°, (g) 23°, and (h) 30°. In each figure, upper and lower panels denote VBT and CBB states, respectively. Black, white, and gray circles denote the atomic positions of nitrogen, boron, and hydrogen atoms, respectively.

presents the contour plots of squared wave functions of the VBT and CBB states of h-BN with various edge angles at the Γ point. For the h-BN ribbons with all edge angles, the VBT state is distributed on N atoms and extended throughout the ribbon. The distribution is qualitatively the same as that of the VBT of bulk h-BN. On the other hand, the distribution exhibits different characteristics to that of graphene nanoribbons. In the case of graphene nanoribbons, except for those with armchair edges, the VBT state is localized at the edge atomic sites with zigzag structure because of its edge state nature. However, as shown in Fig. 4.7, the VBT state of the h-BN nanoribbon does not exhibit an edge-localized nature even though the ribbon has perfect zigzag edges.

In contrast to the VBT state, the CBB state exhibits an unusual nature, which is totally different from those of bulk h-BN and graphene nanoribbons. The CBB state of all h-BN ribbons is not distributed on the atomic sites but in the vacuum region where atoms are absent, exhibiting the nearly free electron (NFE) state nature which is inherent in the layered materials, such as graphene [4.33–4.36], h-BN [4.5, 4.6], and transition metal dichalcogenides [4.37]. For the ribbons with edge angles up to 8°, CBB states are distributed in the vacuum region above and below the ribbons, similar to the conventional NFE states of h-BN sheets and graphene. For ribbons with zigzag and near-zigzag edges, the maxima of the CBB states are distributed alongside the rightmost (N-rich) edges of the ribbons with about 3 Å vacuum region. The states are primarily distributed in the vacuum region separated from the rightmost edge atomic site and are also slightly distributed at the atomic site near the edge. Furthermore, the states are extended along the direction parallel to the ribbon with small undulations in the vacuum region that reflect the edge atomic arrangement. The characteristic distribution of these states as well as the quadratic dispersion band indicate that the CBB states of ribbons with near-zigzag and zigzag edges are the NFE states at the edge of the atomic networks, as in the case of graphene nanoribbons under a lateral electric field as mentioned in Secs. 3.4 and 3.5 [4.36]. Calculating the effective electron mass from the energy band revealed that the effective masses of nanoribbons are ranging from 0.9 to 1.1 m_e, where m_e is the bare electron mass. Thus, the lowest branch of the conduction band of h-BN nanoribbons still possesses NFE nature. Furthermore, because the NFE nature is sensitive to the electrostatic potential, the CBB state with edge NFE nature shifts downward with increasing edge angle, corresponding to an increase in the number of N atoms that deepen the electrostatic potential outside the ribbon.

4.2.2 Clean edges

As shown in Fig. 4.2, substantial structural reconstruction occurs at edge atoms to reduce electron energy arising from the dangling bonds with increasing lattice energies in all nanoribbons except the edge angle of 30° (zigzag). In particular, atoms situated at the armchair portion are remarkably deformed from the ideal sp^2 bond angles by the reconstruction. N atoms protrude from the edges to increase their $2s$ nature to accommodate excess electrons. According to the protruding nature of N atoms, B atoms shift inward to form a linear sp-hybridized chain with neighboring N atoms supplying their valence electrons to N atoms. In addition to the substantial structural reconstruction, the ribbon with near-zigzag edges exhibits bond alternation both along and normal to the ribbon. For the ribbon with zigzag edges, the bond alternation normal to the ribbon occurs around the N edge. On the other hand, around the B edge, long-range bond modulation occurs along the ribbon direction.

Because of the dangling/unsaturated bonds at the edge atomic sites, it is thought that the clean edges are less stable than the hydrogenated edges. Figure 4.4(b) shows the edge formation energy of h-BN nanoribbons with clean edges as a function of ribbon width. The edge formation energy E_{edge} was evaluated using the following formula:

$$E_{\text{edge}} = (E_{\text{total}} - N_{\text{BN}}\mu_{\text{BN}})/L_{\text{edge}} \tag{4.2}$$

where E_{total}, N_{BN}, μ_{BN}, and L_{edge} denote the total energy of ribbons, the number of pairs of B and N atoms, the energy potential of h-BN per BN pair, and the edge length of a unit cell, respectively. As shown in Fig. 4.4(b), the formation energy of clean edges is six to ten times larger than that of hydrogenated edges. In contrast to the nanoribbons with hydrogenated edges, edge formation energy of armchair edges is smaller than that of zigzag edges for the h-BN nanoribbons with clean edges. This indicates that in the case of h-BN nanoribbons with clean edges, the armchair edges are more stable than the zigzag edges because the large structural reconstruction decreases the electron energy arising from the unsaturated B/N bonds. On the other hand, the edge formation energy remains constant in the ribbons with a width of 7 Å or wider as in the case of hydrogenated edges.

Figure 4.5(b) shows the edge formation energy and the energy gap of h-BN nanoribbons with clean edges as a function of the edge angle. In contrast to nanoribbons with hydrogenated edges, the edge formation energy monotonically increases with increasing the edge angle without any plateaus. By analogy with the relationship between edge formation energies and electronic structure in graphene nanoribbons, the monotonic increase of the edge formation energy implies that nanoribbons with clean edges are metals with a number of electron states at Fermi level (E_F).

We also found that the ribbons with armchair edges and an edge angle of $\theta = 5°$ are semiconductors while the other ribbons are metals, in contrast to nanoribbons with hydrogenated edges. The ribbons with an edge angle of 0 and 5° have fundamental gaps of 4 and 0.1 eV, respectively. The semiconducting nature of the armchair ribbons makes the armchair edge the most energetically stable among the eight edge angles. The semiconducting electronic structure of the ribbon with armchair edges is ascribed to the substantial atomic reconstruction at the edges. Because of this reconstruction, B atoms at the armchair edge possess an sp nature with empty π states, while N atoms

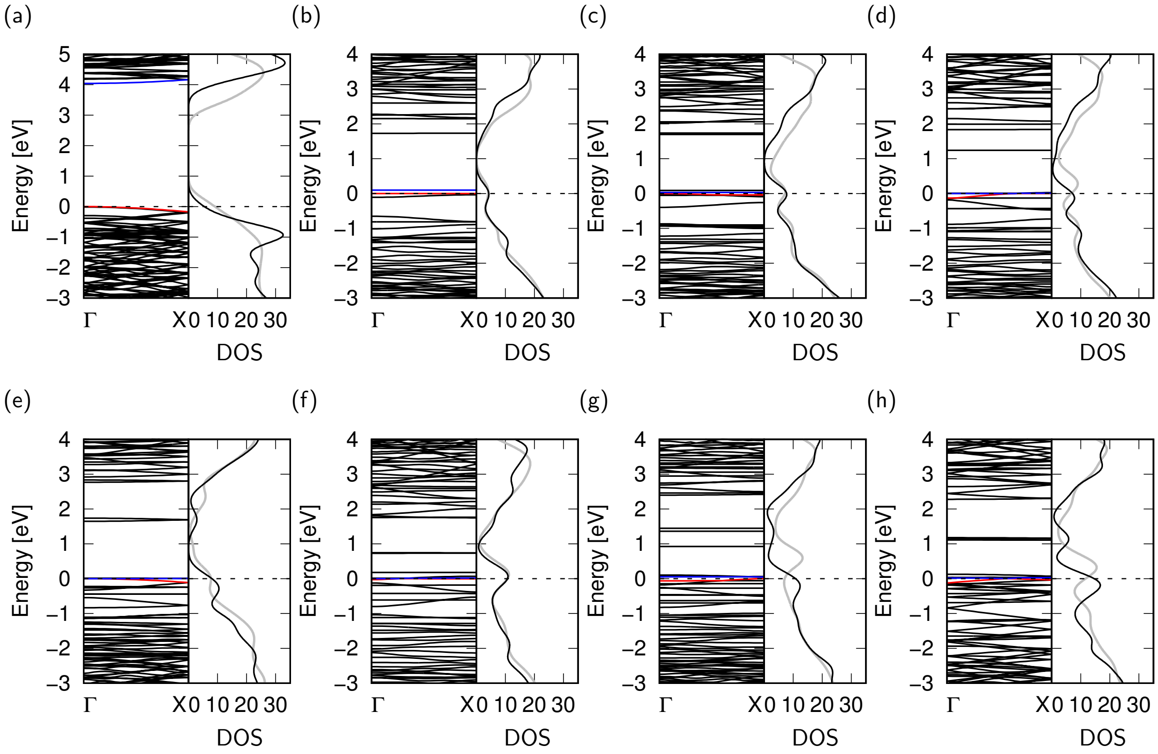

Figure4.8 Electronic structures and density of states (DOS) of h-BN nanoribbons with clean edges of which edge angles are (a) 0°, (b) 5°, (c) 8°, (d) 14°, (e) 16°, (f) 22°, (g) 23°, and (h) 30°. Red and blue lines indicate VBT and CBB states, respectively. Gray lines denote the DOS of the nanoribbons at the temperature of 1000 K. Energies are measured from E_F and VBT for metallic and semiconducting nanoribbons, respectively. Unit of DOS is states/eV.

possess decomposed s and p states that are fully filled by electrons. In accordance with the reconstruction, this nanoribbon does not possess unsaturated bonds even though it is not terminated by H atoms. By focusing on the detailed edge atomic arrangement of the ribbons with respect to the edge angle, we find that substantial structural reconstruction occurs around the armchair regions of the edges. Thus, the monotonic increase in the edge formation energy is ascribed to the decrease of armchair portions. As shown if Fig. 4.5(b), as in the case of hydrogenated edges, there is a correlation between edge formation energy and energy gap. Semiconducting armchair nanoribbons have small edge formation energies while metallic nanoribbons have edge formation energies larger than that of the armchair nanoribbon.

Figure 4.8 shows the electronic energy band structure and DOS of nanoribbons with clean edges. Compared with the electronic structures of nanoribbons with hydrogenated edges, nanoribbons with clean edges have extra states around E_F with less dispersion, arising from the dangling/unsaturated bonds of B and N atoms situated at the edges. Because of the localized nature of the dangling bond states, these states cause the flat dispersion band at E_F. Because of the substantial atomic reconstruction, the dangling bonds are absent at the atomic sites at the armchair edges. Thus, the number of states at E_F increases with increasing portion of zigzag edges. Indeed, the DOS at E_F monotonically increases with increasing edge angle θ from 5 to 30°. This large number of states at E_F causes instability in the energy of the edges with these angles, similar to the case of graphene nanoribbons. As in the case of nanoribbons with hydrogenated edges, the electronic structure of nanoribbons with clean edges is less sensitive to the structural corrugations under the finite temperature.

It is worth investigating the detailed properties of the electronic states at or near E_F. To unravel the origin of these states, we depict the squared wave function of the electron states of nanoribbons with edge angles of 0, 5, 8, 14, 16, 22, 23, and 30° at or near E_F in Fig. 4.9 at the Γ point. For the nanoribbon with armchair edges, its VBT state is distributed on N atoms with π nature and extends throughout the ribbons. The CBB state has an NFE nature, which is distributed in the vacuum region above and below the ribbon, as in the case of the nanoribbons with hydrogenated edges. For the remaining ribbons, the state at E_F is primarily localized on N atoms situated near the N-rich edges with π and σ natures. By focusing on the wave function of the ribbon with zigzag edges, we find that VBT and CBB states are localized at the N atoms at the N-rich edge with σ and π natures, respectively. Thus, the states with σ nature are classified as dangling bond states arising from the unsaturated bond of N atoms at the edges with zigzag shapes. It should be noted that such states are absent at the atomic sites of edges with armchair shapes. In this case, the edge reconstruction at the armchair region leads to substantial upward and downward shifts of states induced by a considerable change of orbital hybridization. In contrast to the ribbons with hydrogenated edges, no delocalized states with NFE nature emerge at or near E_F for the ribbons with finite edge angles.

4.3 Polarity of Edges

To investigate the polar properties of h-BN edges, we considered nanoribbons with hydrogenated and clean edges with edge angles of 0 (armchair), 5, 8, 14, 16, 22, 23, and 30° (zigzag). The Brillouin zone integration was carried out with an equidistance 1 k-point along the ribbon direction, which correspond to 8 k-points sampling in the conventional cell of h-BN. This gave sufficient convergence of the total energies and electronic structures for the h-BN ribbons. The geometric structures of h-BN nanoribbons were optimized until the force acting on atoms was less than 0.005 Ry/Å under the fixed lattice parameter along the ribbons, which was determined by the

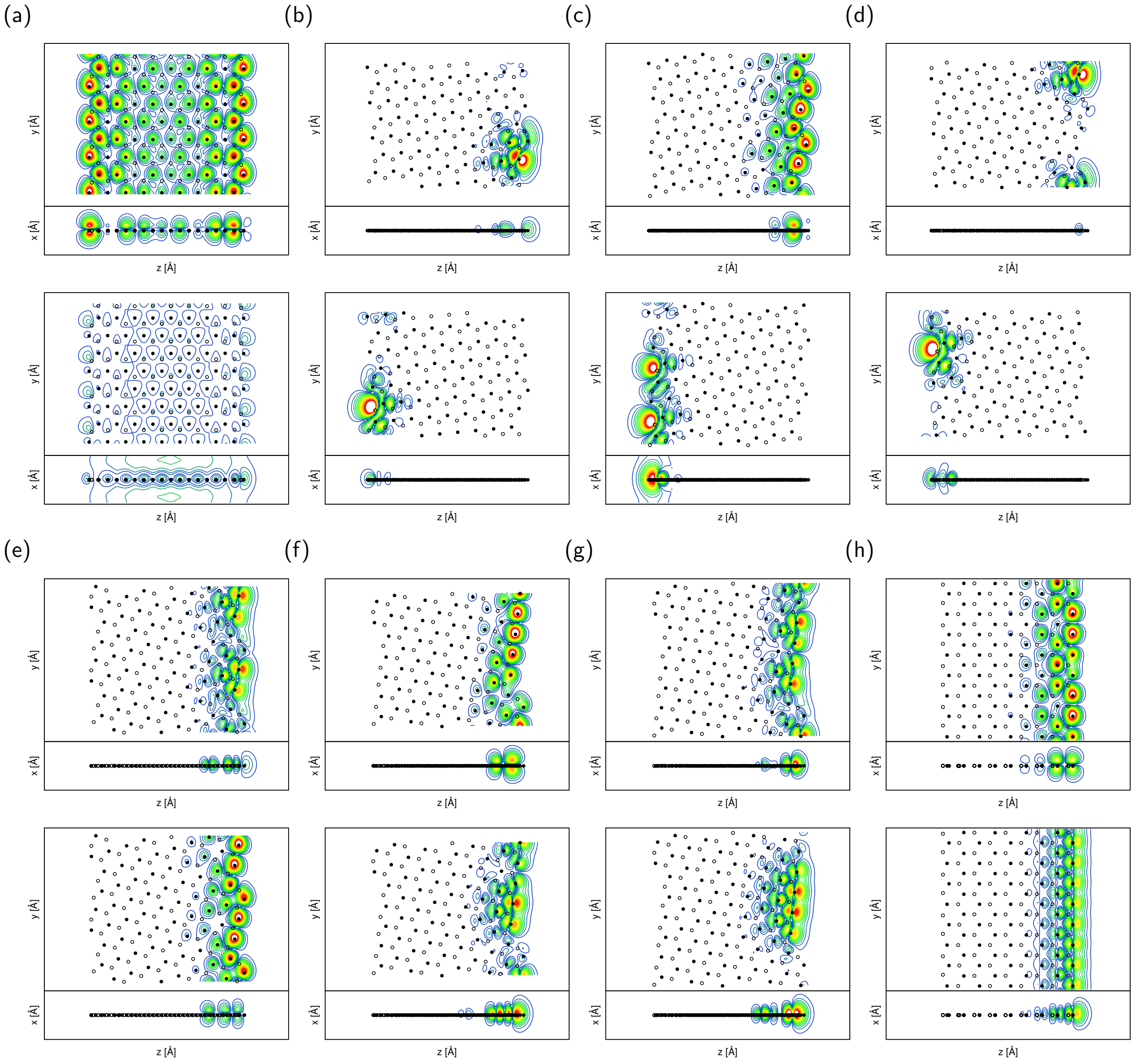

Figure4.9 Top ($x = 0$) and side ($y = 0$) views of contour plots of wave functions at the Γ point near the Fermi level E_F of h-BN nanoribbons with clean edges of which edge angles θ of (a) 0°, (b) 5°, (c) 8°, (d) 14°, (e) 16°, (f) 22°, (g) 23°, and (h) 30°. In each figure, upper and lower panels denote VBT and CBB states, respectively. Black and white circles denote the atomic positions of nitrogen and boron atoms, respectively.

bulk bond length of 1.45 Å. To simulate the open boundary condition in lateral inter-ribbon directions because h-BN nanoribbons with arbitrary edge shapes intrinsically possess polarity, which arises from non-stoichiometric arrangements of B and N atoms at each edge, we set the ESM with a relative permittivity of 1 alongside the rightmost and leftmost atoms of the nanoribbons with 8 Å vacuum spacing (Fig. 4.3).

Figure 4.10 shows the electrostatic potential of h-BN nanoribbons with hydrogenated and clean edges. For the majority of edge angles we found a potential dif-

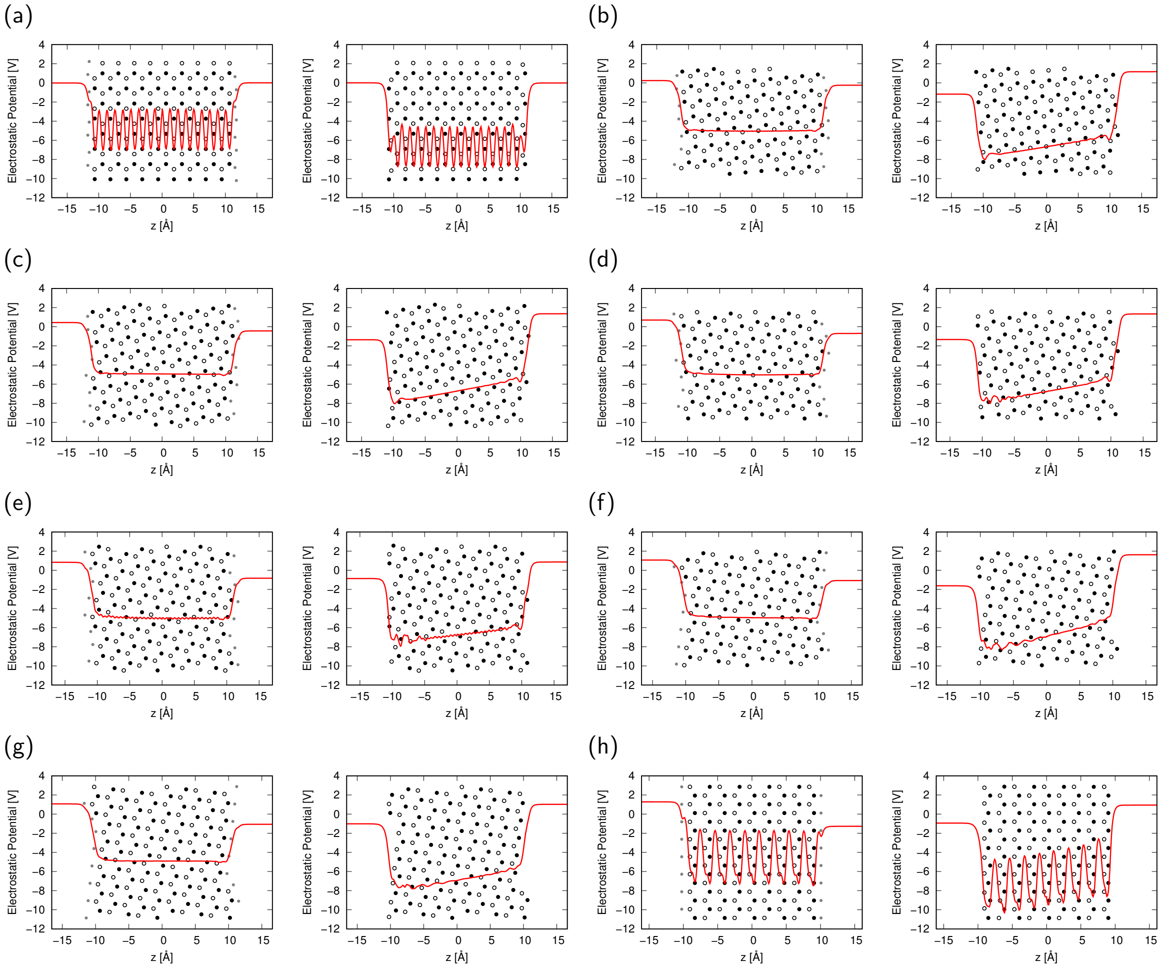

Figure4.10 Plane averaged electrostatic potential normal to the h-BN nanoribbons with the edge angles of (a) 0, (b) 8, (c) 16, (d) 23, and (e) 30. Left and right panels denote the hydrogenated and clean edges, respectively. Black, white, and gray circles denote the atomic positions of N, B, and H atoms, respectively.

ference between the left (B rich edge) and right (N rich edge) vacuum regions of the nanoribbons, except at 0°, which corresponded to an armchair edge. These results indicate that these h-BN nanoribbons have polarity between B and N rich edges. Interestingly, the direction of the polarity for the hydrogenated nanoribbons was opposite to that of nanoribbons with clean edges. However, because of the symmetric atomic arrangement, with respect to the ribbon axis, no polar properties occurred in the ribbons with armchair edges.

Figure 4.11 shows the edge angle dependence of polarity which is defined by the potential difference between the left and right vacuum of the nanoribbons. For the case of hydrogenated nanoribbons, the polarity was proportional to the edge angle. The potential difference increased with increasing the edge with zigzag shape, because

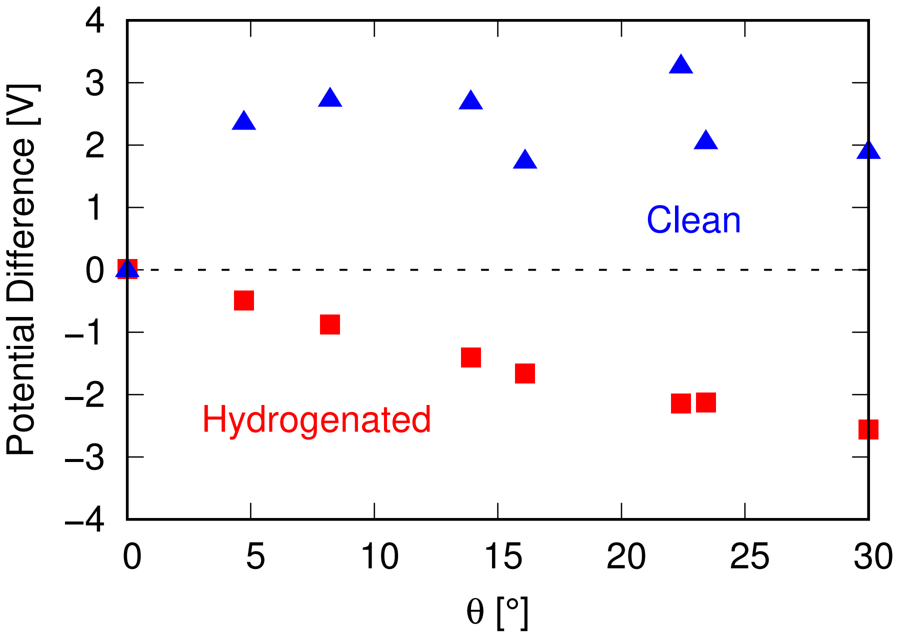

Figure4.11 Potential difference between leftmost and rightmost vacuum of the h-BN nanoribbons as a function of edge angle θ. Red squares and blue triangles denote the hydrogenated and clean edges, respectively.

of the imbalance in the number of B and N atoms between the two edge atomic sites. In contrast, the potential difference was insensitive to the edge angle for the ribbon with clean edges. The potential difference ranged from 2 to 3 V depending on the edge angle. This edge angle dependence is attributed to atomic reconstruction of the clean edges of h-BN nanoribbon: edge atomic structures are sensitive to the edge angle. In view of the polarity direction, the potential difference of the hydrogenated nanoribbons was opposite to that of nanoribbons with clean edges at all edge angles.

We also investigated the width dependence of the polarity in h-BN nanoribbons. Figure 4.12 shows the potential difference of zigzag nanoribbons as a function of their width. In both nanoribbons with hydrogenated and clean edges, the potential difference remained almost constant at all widths. The reversal of the direction of the edge polarization on hydrogenation of the edges was also unchanged. This result indicated that the polarization of h-BN nanoribbons does not depend on ribbon width, but only on the atomic arrangement and hydrogenation of the edges.

To investigate the hydrogen concentration dependence of the polarity of the h-BN ribbons, we calculated the polarity of zigzag h-BN nanoribbons with edges asymmetrically terminated by H atoms. As shown in Fig. 4.13, at most hydrogen concentrations, the electrostatic potential at the N edge was higher than that at the B edge. In contrast, a high H coverage of the N edges caused polarity inversion of the h-BN ribbon,

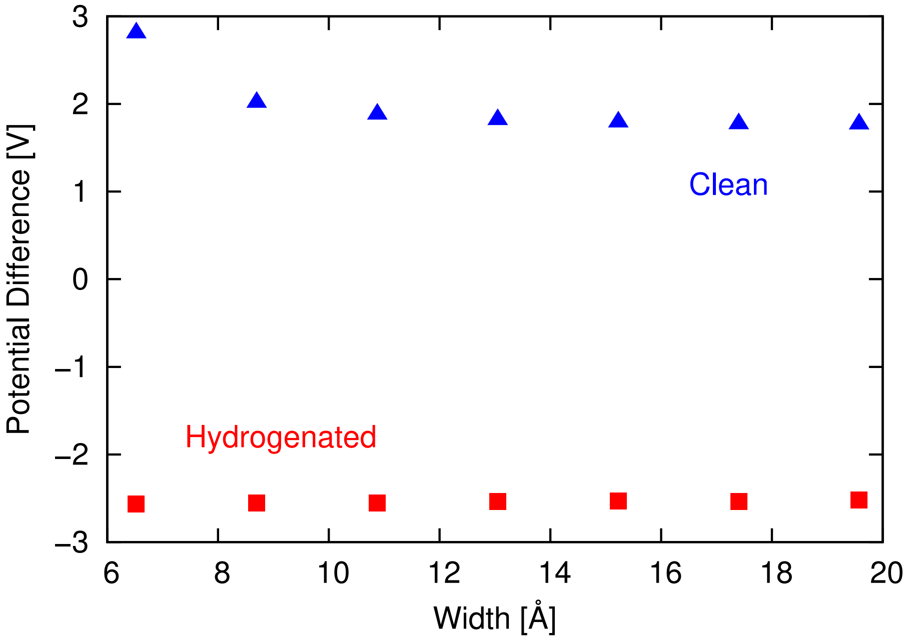

Figure4.12 Potential difference between leftmost and rightmost vacuum of the h-BN nanoribbons as a function of ribbon width. Red squares and blue triangles denote the hydrogenated and clean edges, respectively.

and the potential at the B edge became higher than that at the N edge. It should be noted that nanoribbons with hydrogen concentrations of 87.5% and 50∼87.5% at the N and B edges, respectively, exhibited non-polar properties, although the ribbons possessed zigzag edges. These results indicate that the polarization of h-BN nanoribbons might be tunable through changing hydrogen pressure and reaction temperature during synthesis that cause the asymmetric hydrogen concentration at the edge atomic sites.

In addition to hydrogenation, the polarity of the h-BN nanoribbon may also depend on structural deformation under the strain. Figure 4.14 shows the polarity of the h-BN ribbons with hydrogenated zigzag edges under uniaxial tensile and compressive strain along the direction of the ribbons. Under application of the tensile strain, the polarity monotonically decreased with increasing strain, and changed its direction at a critical strain. This suggests that the tensile strain can invert the polarity of h-BN nanoribbons. The critical strain depended slightly on the edge angle, because the polarity of the ribbons at the zero strain was proportional to the edge angles. The critical strain for ribbons with the zigzag edges was 16% while those for the ribbons with shallower angles were between 12% and 15% depending on the edge angles (Fig. 4.14). In contrast, the polarity of the ribbon slightly increased under compressive strain, and saturated at a strain of 5% at which the polarity depended

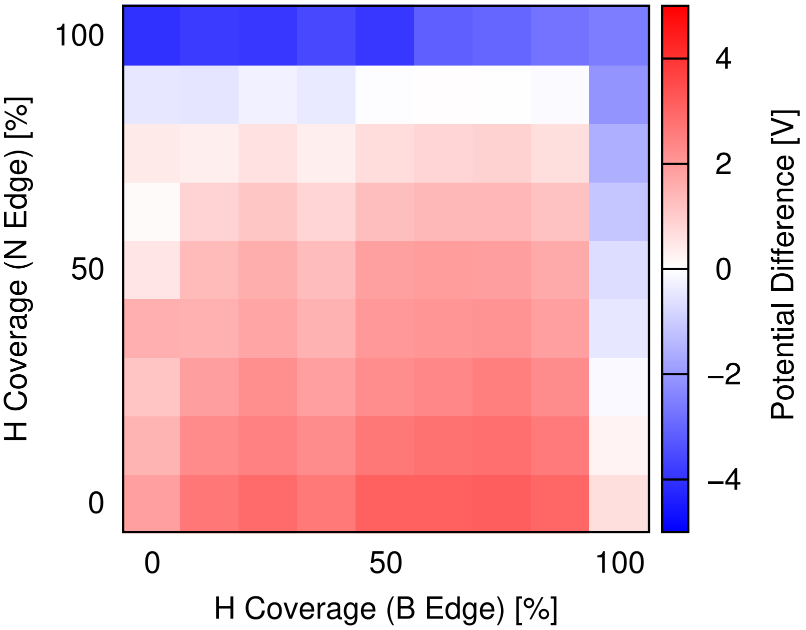

Figure4.13 A color map of the potential difference between edges of zigzag nanoribbons as a function of hydrogen concentration at the leftmost (B) and rightmost (N) edge atomic sites.

on the edge angles. This result indicates that tensile strain also can control the polarity of h-BN ribbons in addition to the edge structure and edge termination.

4.4 Conclusion

In this chapter, we studied the geometric and electronic structures of h-BN nanoribbons with edge angles ranging from armchair to zigzag using density functional theory. Our calculations show that the edge stability and electronic structure of h-BN nanoribbons strongly depend on the edge termination. In the case of hydrogenated edges, the edge formation energy retains a constant value for all nanoribbons. This indicates that hydrogenated h-BN nanoribbons and nanoflakes inherently possess edge roughnesses under static conditions. On the other hand, for ribbons with clean edges, the edge formation energy monotonically increases with the proportion of zigzag edge. Furthermore, the edge stability strongly correlates with the electronic structure of h-BN nanoribbons. Nanoribbons with small edge formation energy are semiconductors with a finite energy gap, while ribbons with large formation energy are metals with a large DOS at E_F. By analyzing the wave functions near E_F, we found that the dangling bond states appeared around E_F for nanoribbons with clean edges, except for that with armchair edges. Based on these findings, the increase in the DOS near E_F

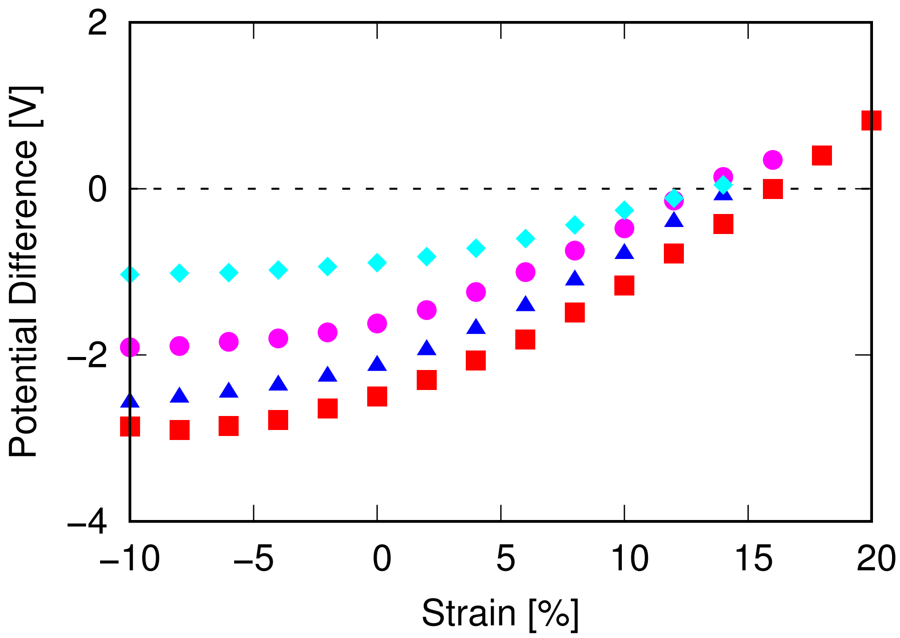

Figure4.14 Potential difference between edges of hydrogenated h-BN nanoribbons as a function of strain. Red squares, blue triangles, magenta circles, and cyan diamonds denote edge angles of 30, 23, 16, and 8°.

arising from the dangling bond states is the origin of the increase in formation energy for clean edges. The present results indicate that the shape of the h-BN nanoflakes is tunable by controlling the edge termination by atoms and molecules. Furthermore, the energetics provides guiding principles to design heterogeneous layered materials consisting of h-BN and graphene that possess unusual electronic structures [4.38,4.39].

We also studied the polarity of h-BN nanoribbons with edge angles from armchair to zigzag by calculating the electrostatic potential using density functional theory. Our calculations showed that the potential difference between the leftmost and rightmost edges of nanoribbons with hydrogenated nanoribbons is opposite to that with clean edges. This indicated that the edge hydrogenation can invert the polarity of h-BN ribbons. The polarity was sensitive to the edge angle and edge termination, while it is insensitive to the ribbon width. In the case of hydrogenated nanoribbons, the polarity increased with increasing the zigzag portion at the edges. On the other hand, polarity in the ribbons with clean edges seems to be independent of the edge angle. By analyzing the electrostatic potentials of zigzag edges at different hydrogen concentrations we found that the potential at the N edge was higher than that at the B edge for the most hydrogen concentrations, except under hydrogen rich conditions. Under the high H concentration for both edges, the polarity was opposite to that for the low H concentration. Thus, the h-BN nanoribbon exhibited non-polar properties at certain H concentration, although the zigzag h-BN nanoribbons essentially have polarity at their edges. In addition to the edge hydrogenation, the uniaxial tensile strain on hydrogenated ribbons can also invert their polarity at a critical tensile strain of 12 to 16 %, depending on the edge angles.

References

[1] D. Golberg, Y. Bando, Y. Huang, T. Terao, M. Mitome, C.Tang, and C. Zhi, *ACS Nano* **4**, 2979 (2010).

[2] L. Song, L. Ci, H. Lu, P.B. Sorokin, C. Jin, J. Ni, A.G. Kvashnin, D.G. Kvashnin, J. Lou, B.I. Yakobson, and P.M. Ajayan, *Nano Lett.* **10**, 3209 (2010).

[3] C. Zhi, Y. Bando, C. Tang, H. Kuwahara, and D. Golberg, *Adv. Mater.* **21**, 2889 (2009).

[4] J.H. Warner, M.H. Rümmeli, A. Bachmatiuk, and B. Büchner, *ACS Nano* **4**, 1299 (2010).

[5] A. Catellani, M. Posternak, A. Baldereschi, and A.J. Freeman, *Phys. Rev. B* **36**, 6105 (1987).

[6] X. Blase, A. Rubio, S.G. Louie, and M.L. Cohen, *Phys. Rev. B* **51**, 6868 (1995).

[7] C.R. Dean, *Nature Nanotechnol.* **5**, 722 (2010).

[8] W. Gannett, *Appl. Phys. Lett.* **98**, 242105 (2011).

[9] P.J. Zomer, *Appl. Phys. Lett.* **99**, 232104 (2011).

[10] K.H. Lee, H.-J. Shin, J. Lee, I.-Y. Lee, G.-H. Kim, and J.-Y. Choi, *Nano Lett.* **12**, 714 (2012).

[11] J. Zhou, Q. Wang, Q. Sun, and P. Jena, *Phys. Rev. B* **81**, 085442 (2010).

[12] J. Kotakoski, C.H. Jin, O. Lehtinen, K. Suenaga, and A.V. Krasheninnikov, *Phys. Rev. B* **82**, 113404 (2010).

[13] P.P. Shinde and V. Kumar, *Phys. Rev. B* **84**, 125401 (2011).

[14] J. Beheshtian, A. Sadeghi, Neek-M. Amal, K.H. Michel, and F.M. Peeters, *Phys. Rev. B* **86**, 195433 (2012).

[15] A.B. Preobrajenski, M.A. Nesterov, M.L. Ng, A.S. Vinogradov, and N. Mårtensson, *Chem. Phys. Lett.* **446**, 119 (2007).

[16] W. Auwärter, M. Muntwiler, J. Osterwalder, and T. Greber, *Surf. Sci.* **545**, L735 (2003).

[17] W.-Q. Han, L. Wu, Y. Zhu, K. Watanabe, and T. Taniguchi, *Appl. Phys. Lett.* **93**, 223103 (2008).

[18] N.G. Chopra, R.J. Luyken, K. Cherrey, V.H. Crespi, M.L. Cohen, S.G. Louie, and A. Zettl, *Science* **269**, 966 (1995).

[19] D. Golberg, Y. Bando, M. Eremets, K. Takemura, K. Kurashima, and H. Yusa, *Appl. Phys. Lett.* **69**, 2045 (1996).

[20] W. Han, Y. Bando, K. Kurashima, and T. Sato, *Appl. Phys. Lett.* **73**, 3085 (1998).

[21] E. Bengu and L.D. Marks, *Phys. Rev. Lett.* **86**, 2385 (2001).

[22] A. Rubio, J.L. Corkill, and M.L. Cohen, *Phys. Rev. B* **49**, 5081 (1994).

[23] X. Blase, A. Rubio, S.G. Louie, and M.L. Cohen, *Europhys. Lett.* **28**, 335 (1994).

[24] N. Alem, R. Erni, C. Kisielowski, M.D. Rossell, W. Gannett, and A. Zettl, *Phys. Rev. B* **80**, 155425 (2009).

[25] A. Loiseau, F. Willaime, N. Demoncy, G. Hug, and H. Pascard, *Phys. Rev. Lett.* **76**, 4737 (1996).

[26] R. Mukherjee and S. Bhowmick, *J. Chem. Theory Comput.* **7**, 720 (2011).

[27] E. Kan, F. Wu, H. Xiang, J. Yang, and M.-H. Whangbo, *J. Phys. Chem. C* **115**, 17252 (2011).

[28] A. Lopez-Bezanilla, J. Huang, H. Terrones, and B.G. Sumpter, *Nano Lett.* **11**, 3267 (2011).

[29] Y. Liu, S. Bhowmick, and B.I. Yakobson, *Nano Lett.* **11**, 3113 (2011).

[30] Z. Zhang and W. Guo, *Phys. Rev. B* **77**, 075403 (2008).

[31] F. Zheng, G. Zhou, Z. Liu, J. Wu, W. Duan, B.-L. Gu, and S.B. Zhang, *Phys. Rev. B* **78**, 205415 (2008).

[32] S. Okada, *Phys. Rev. B* **77**, 041408 (2008).

[33] M. Posternak, A. Baldereschi, A.J. Freeman, E. Wimmer, and M. Weinert, *Phys. Rev. Lett.* **50**, 761 (1983).

[34] M. Posternak, A. Baldereschi, A.J. Freeman, and E. Wimmer, *Phys. Rev. Lett.* **52**, 863 (1984).

[35] Y. Miyamoto, A. Rubio, X. Blase, M.L. Cohen, and S.G. Louie, *Phys. Rev. Lett.* **74**, 2993 (1995).

[36] Q. Liu, Z. Li, and J. Yang, *Chin. J. Chem. Phys.* **24**, 22 (2011).

[37] N.-T. Cuong, M. Otani, and S. Okada, *J. Phys. Condens. Matter* **26**, 135001 (2014).

[38] S. Okada, and A. Oshiyama, *Phys. Rev. Lett.* **87**, 146803 (2001).

[39] M. Maruyama, and S. Okada, *J. Phys. Chem. C* **120**, 1923 (2016).

Chapter 5

Summary

Two-dimensional materials have great deal of attention not only in nanoscience but also in nanothechnology because of its unique geometric and electronic properties. The electronic properties of these materials are strongly affected by their edges. However, it is still unclear the correlation between edge geometry and electronic structure. In this thesis, we study the energetics and electronic properties of edges of two-dimensional materials using density functional theory.

In Chap. 3, we study the energetics and electronic structure of graphene nanoribbons with hydrogenated and clean edges with respect to the detailed edge shapes. Our calculations showed that the stability of graphene edges strongly depends on the length of the zigzag edge portion. Near-zigzag edges are less stable than near-armchair edges because of the large number of states at the Fermi level (E_F) induced at near-zigzag edges. The edge formation energy retains a constant value up to the edge angle of 16°, after which it monotonically increases with increasing zigzag portion or edge angle. We also found that the edge stability strongly correlates with the electronic structures near the E_F of graphene nanoribbons. Nanoribbons with a small zigzag portion possess edge states near the E_F.

We also showed that the edge atomic sites of the nanoribbons with zigzag shape anomalously screen the external electric field; the electrostatic potential oscillates rapidly, leading to over-screening in the vicinity of edge C atomic sites. It is also found that the penetration depth of anomalous screening depends on the edge structure of nanoribbons.

Under a lateral electric field, we also showed that the nearly free electron (NFE) state emerges in the vacuum region outside the leftmost edge of the ribbons and shifts downward with increasing electric field. We also found that electrons are injected into the NFE state of graphene nanoribbons by the critical electric field, which is inversely proportional to the ribbon width. NFE states strongly depend on the mutual arrangements of graphene nanoribbons with respect to the electric field. In contrast, the electronic energy bands associated with the π electrons are insensitive to the relative direction of the ribbon with respect to the external electric field. We also observe that the electric field concentration around the edges leads to the orientation dependence of the NFE states on the field.

In Chap. 4, we study the energetics and electronic structure of hexagonal boron nitride (h-BN) nanoribbons with hydrogenated and clean edges with respect to the detailed edge shapes. Our calculations showed that the stability of h-BN edges strongly depends on the edge termination. In the case of hydrogenated edges, the formation energy is constant for all edge angles ranging from armchair to zigzag, indicating that h-BN may exhibit rich variation in their edge atomic arrangements under static conditions. The hydrogenated h-BN nanoribbons are insulators with an energy gap of 4 eV irrespective of edge shape, in which the lowest branch of the conduction band exhibits NFE states nature distributed in the vacuum region outside the ribbons. In contrast, the formation energy of h-BN nanoribbons with clean edges monotonically increases as the edge angle is changed from armchair to zigzag. Our analysis reveals that the increase of density of states at the E_F arising from dangling bond states leads to this monotonic increase of edge formation energy in h-BN nanoribbons with clean edges.

We also study the polarity of h-BN nano-flakes in terms of their edge geometries, edge hydrogen concentration, and uniaxial strain by evaluating their electrostatic potential. Our calculations showed that the polarity of the nanoribbons is sensitive to their edge shape, edge hydrogen coverage, and uniaxial tensile strain. Polarity inversion of the ribbons can be induced by controlling the hydrogen concentration at edges and the uniaxial tensile strain. The polarity inversion indicates that h-BN nanoribbons can exhibit non-polar properties at a particular edge hydrogen concentration and tensile strain, even though the nanoribbons essentially have polarity at the edge. We also found that the edge angle affects the polarity of nanoribbons with hydrogenated edges.

List of Publications

[1] A. Yamanaka and S. Okada, “Electronic properties of carbon nanotubes under an electric field”, *Appl. Phys. Express* **5**, 095101 (2012).

[2] A. Yamanaka and S. Okada, “Anomalous electric-field screening at the edge atomic sites of finite-length zigzag carbon nanotubes”, *Appl. Phys. Express* **6**, 045101 (2013).

[3] A. Yamanaka and S. Okada, “Electronic properties of capped carbon nanotubes under an electric field: inhomogeneous electric-field screening induced by bond alternation”, *Jpn. J. Appl. Phys.* **52**, 06GD04 (2013).

[4] A. Yamanaka and S. Okada, “Electrostatic potential of hydrogenated finite-length carbon nanotubes under an electric field”, *Phys. Status Solidi C* **10**, 1624 (2013).

[5] A. Yamanaka and S. Okada, “Structural dependence of electronic properties of graphene nanoribbons on an electric field”, *Jpn. J. Appl. Phys.* **53**, 06JD05 (2014).

[6] A. Yamanaka and S. Okada, “Electron injection into nearly free electron states of graphene nanoribbons under a lateral electric field”, *Appl. Phys. Express* **7**, 125103 (2014).

[7] A. Yamanaka and S. Okada, “Energetics and electronic structure of graphene nanoribbons under a lateral electric field”, *Carbon* **96**, 351 (2016).

[8] A. Yamanaka and S. Okada, “Influence of electric field on electronic states of graphene nanoribbons under a FET structure”, *Jpn. J. Appl. Phys.* **55**, 035101 (2016).

[9] A. Yamanaka and S. Okada, “Energetics and electronic structure of h-BN nanoflakes”, *Sci. Rep.* **6**, 30653 (2016).

[10] R. Taira, A. Yamanaka, and S. Okada, “Electronic structure modulation of graphene edges by chemical functionalization”, *Appl. Phys. Express* **9**, 115102 (2016).